A PRECISE DETERMINATION OF THE PION BETA DECAY RATE: DESIGN AND CALIBRATION

Kétévi Adiklè Assamagan
Lomé Togo,
Afrique Occidentale

B.S., Université Du Bénin, 1985
M.S., Ball State University, 1989

A Dissertation Presented to the Graduate
Faculty of the University of Virginia
in Candidacy for the Degree of
Doctor of Philosophy

Department of Physics

University of Virginia
May 1995

Abstract

A precise determination of the pion beta decay $(\pi^+ \to \pi^0 e^+ \nu_e)$ rate constitutes a stringent test for the Cabibbo universality through the Conserved Vector Current (CVC) hypothesis and for the unitarity of the Cabibbo-Kobayashi-Maskawa (CKM) mixing matrix. The unitarity of the CKM matrix can be used to constrain certain extensions to the minimal Standard Model (SM), for instance the existence of a fourth generation of quarks. The discrepancy between superallowed Fermi decay and neutron beta decay data, and the level of accuracy of the previous experiments on pion beta decay call for a new precision measurement of $\pi^+ \to \pi^0 e^+ \nu_e$ rate. This precision experiment is currently in progress at the Paul Scherrer Institute in Switzerland. The design of the experimental apparatus and its calibration are the subject of this work. Positive pions of momentum of 116 MeV/c were stopped in a scintillator fiber hodoscope. The beam distributions and contaminations have been investigated and measured. Monte Carlo simulations aided in the design of the apparatus, especially the shower calorimeter, and the response of its modules to monoenergetic positrons and photons have been measured. A cosmic ray tomography apparatus is being used to determine the light collection non-uniformity of each of the CsI modules. Finally, the response of the apparatus to $\pi^+ \to e^+ \nu_e$ events has been measured, since these events will be used for normalization purposes in determining the pion beta decay rate.

Once upon a time The Great Spider, Ananse Kokrofu was not pleased with the state of wisdom in the world. Ananse observed that people were not looking after it properly, consequently a great deal of wisdom was getting lost. The Great Spider argued that although people did not respect wisdom as they should, future generations will be very glad to use every bit they could. So Ananse decided to gather all the wisdom in the world and keep it in a safe place.

In due time, Ananse did indeed collect all the wisdom in the world into a jar and began to climb a tall palm tree where he had planned to store it. However, halfway to the top, Ananse ran into difficulties because he had tied the jar in front of himself and this affected severely his climbing. His son who was watching from the ground exclaimed: 'Father, if you really had all the wisdom in the world with you up there, you would have tied the jar on your back.' The difficulties were too much even for Ananse, and he was also tired from long labor. He untied the jar in a fit of anger an dropped it. The jar broke and wisdom was scattered far and wide. Men and women came and gathered their own jars of whatever they could find. This explains why few people have much wisdom, some have a little, but many have none at all [Dav-69].

The Akan People
Modern Ghana

To
Ananse Kokrofu
Dispenser of wisdom

Contents

Acknowledgements

The author would like to present his gratitude to his research advisor, Professor Dinko Počanić. The writer also expresses gratitude to Professor Ralph Minehart, Professor P. Q. Hung and Professor Elias Towe for their constructive critiques and suggestions toward the completion of this work.

Special thanks to Professor Klaus Ziock for the fabrication of the target and his contribution to the experiments described in this paper, and to Dr Bryan Wright for all his help in the understanding and the assimilation of the softwares used in preparing the present work.

Thanks also to Dr Cole Lee Smith who kindly reviewed parts of this writing. Dr Emil Frlež has introduced the author to some topics related to data analysis, simulation codes and the physics of this project. Their interactions from UVA to PSI via LAMPF have proven valuable.

With Steve Bruch who was writing a thesis at the same time, the author had had fruitful discussions regarding particularly the efficient typesetting of a paper such as this one.

The writer hereby acknowledges the people who participated in the pion beta runs presented in this paper.

Sincères remerciements à Dr Claudia Wigger pour toute son aide durant le séjour de l'auteur en Suisse. En somme, cette aide qui comprenait entre autres la recherche d'un appartement, l'explication des nuances d'une culture étrangère, l'assimilation et surtout la traduction d'une langue moins familière, a rendu l'auteur moins aliéné, et par conséquent, a permis à ce dernier de tenir aussi longtemps qu'il a pu.

Thanks also to Mrs Gerda Pirsch and Mrs Marion Limber for their support since the author's arrival at Charlottesville. Their words of encouragement and

the moments shared together especially during Thanksgiving, Christmas and New Year's Day — when a foreign student could find himself alone and lonely — certainly helped the author's morale throughout his stay at UVA.

The author conveys sincere gratitude to his friend, partner and wife Sarah Shanti Boone dit Lo̱nlo̱nNye for her spiritual, emotional and intellectual support during the tough and the good periods: Ata Nyo̱ḡon nè do ap̄é ganḏé no̱o.

To the spiritual allies, the ancestors who walk with the Gods and watch over him, and to the Gods and Goddesses of the Ewe and Mina people, the writer presents his special offering. Thanks in particular to the Goddess Ata Nyo̱ḡon whose protection and guidance have been felt in a remarkable way.

Finalement, l'auteur aimerait présenter ses sincères remerciements à ses parents, frères, soeurs et amis pour leur soutien, patience et tolérance. L'auteur partage les douleurs infligées à l'homme ordinaire de son pays durant ces dernières années et salue tous ceux qui ont lutté et survécu ces turbulences. Le présent chef-d'œuvre est dédié à la mémoire de ceux qui sont tombés durant la lutte pour le changement. Leur courage, effort et sacrifice n'auraient été pour rien car il y eut des concessions et notre pays, que les forces du mal le veuillent ou pas, a pris la direction des jours meilleurs. Par ailleurs, l'auteur a su puiser du courage exemplaire d'un peuple lassé d'être piétiné, tenu à l'écart et exploité sans pitié.

List of Figures

List of Tables

Chapter 1

Introduction

The objective of the first two chapters is the discussion of the scientific motivation for the pion beta decay experiment currently under way at the Paul Scherrer Institute in Switzerland. The explanation of some basic physics concepts will lay a firm foundation for the full understanding of the motivation for the experiment. These include the V$-$A structure of the weak interaction, the Conserved Vector Current hypothesis (CVC), the quark-lepton universality, the unitarity of the quark mixing matrix and the superallowed Fermi decays. Chapter 1 begins with the Dirac equation for the electron, and introduces the helicity and chirality operators as a prelude for the discussion on the V$-$A structure of the weak interactions. The CVC hypothesis is introduced by an analogy with electromagnetic interactions which conserve the electric charge. An alternative formulation of CVC is given using isospin and assuming that the electromagnetic isovector current and the weak vector current are different components of the same isospin current. Cabibbo universality is introduced next with some of its implications, especially the unitarity test of the Cabibbo-Maskawa-Kobayashi (CKM) quark mixing matrix. Finally, the superallowed beta decays are discussed as a particular type of nuclear beta decays involving only vector interactions. It is generally believed that if the CVC hypothesis is true, the vector coupling constants extracted from different superallowed Fermi decays would be the same after the necessary correction factors are accounted for. This universal vector coupling constant and the muon decay coupling constant give one element of the CKM matrix which, combined with the accepted values of some other elements of the matrix, allows a test of unitarity. The extent to which the unitarity test is satisfied places constraints on new physics beyond the Minimal Standard Model of elementary particles.

In chapter 2, the current state of nuclear beta decay and neutron beta decay data is presented. In particular, it is shown that a discrepancy between the nuclear decay data and the neutron decay data justifies a new precision measurement of the pion beta decay rate from which the vector coupling constant can also be extracted. In fact, the pion beta decay, proceeding solely via vector interactions, is similar to pure Fermi nuclear beta decays without the difficulties of nuclear corrections and screening effects. Therefore, the pion beta decay constitutes the most direct test of CVC. The previous experimental measurements of the pion beta decay rate are described in conjunction with the limitations in using their results to check some of the physical concepts presented above. Together, the first two chapters provide the motivation for this new precision experiment whose design and calibration are the subject of this thesis.

A description of the Ring accelerator at the Paul Scherrer Institute as it relates to the experiment is presented in chapter 3 along with the beam studies that have been conducted to date. Specifically, the beam particle rates, contaminations, profiles and spot size are discussed. After the explanation of the motivation and the description of the pion beam, a thorough description of the decay channels of the pion with the associated kinematical information is given in chapter 4. Chapter 5 begins with a general overview of the experiment followed by a description of the salient components of the apparatus together with the scientific justification of their design.

The design of the calorimeter is presented in chapter 6. There, the modularity of the shower calorimeter as a result of a geodesic triangulation is explained. In addition, a discussion on the choice of the calorimeter thickness and material is presented. In chapter 7, the experimental approach is described. The choice of the decay technique and the method of measurement are explained. The calculations of the systematic uncertainties (associated with the experimental technique) and the level of these uncertainties are also discussed. These calculations were carried out using three independent shower simulation codes, and their results showed remarkable agreement after optimization of the codes. In addition, the choice of the calorimeter granularity and the design of the event triggers are discussed. Finally, the procedure for testing the calorimeter crystals prior to assembly is presented.

In chapter 8, detector performances and calibration are discussed. First, the active target and its performance in beam are presented. Second, the surface treatments of the calorimeter modules as they affect the light output and light collection uniformity are also discussed. Next, the cosmic ray tomography system whose aim is to measure the light collection non-uniformity within the volume of each of the calorimeter modules is described and some of its results presented. Finally, the performance and calibration of the calorimeter are discussed. In the concluding chapter, the current state and the outlook of the experiment are described.

1.1 Massless Fermion

The Dirac equation for a massive fermion of momentum $\boldsymbol{p}$ is:

$$H\psi = (\boldsymbol{\alpha} \cdot \boldsymbol{p} + \beta m)\psi \tag{1.1}$$

However, the free particle must satisfy the energy-momentum requirement

$$H^2\psi = (\boldsymbol{p}^2 + m^2)\psi \tag{1.2}$$

which allows the determination of the coefficients β and $\alpha_i (i = 1, 2, 3)$:

$$\boldsymbol{\alpha} = \begin{pmatrix} -\boldsymbol{\sigma} & 0 \\ 0 & \boldsymbol{\sigma} \end{pmatrix} \tag{1.3}$$

and

$$\beta = \begin{pmatrix} 0 & I \\ I & 0 \end{pmatrix}, \tag{1.4}$$

where $\sigma_i (i = 1, 2, 3)$ are the 2×2 Pauli matrices and I is the 2×2 unit matrix. In covariant form, equation (1.1) can be written as:

$$(i\gamma^\mu \partial_\mu - m)\psi = 0, \tag{1.5}$$

where

$$\gamma^0 = \beta, \tag{1.6}$$

$$\boldsymbol{\gamma} = \beta\boldsymbol{\alpha}. \tag{1.7}$$

With

$$\psi = u(\boldsymbol{p})e^{-ip\cdot x}, \tag{1.8}$$

where

$$u(\boldsymbol{p}) = \begin{pmatrix} \chi(\boldsymbol{p}) \\ \phi(\boldsymbol{p}) \end{pmatrix}, \tag{1.9}$$

equation (1.1) leads, after some manipulation, to the following:

$$-\boldsymbol{\sigma}\cdot\boldsymbol{p}\chi + Im\phi = E\chi, \tag{1.10}$$

$$Im\chi + \boldsymbol{\sigma}\cdot\boldsymbol{p}\phi = E\phi. \tag{1.11}$$

In the case of a massless fermion, a neutrino for instance, the above relations are decoupled:

$$E\chi = -\boldsymbol{\sigma}\cdot\boldsymbol{p}\chi, \tag{1.12}$$

$$E\phi = \boldsymbol{\sigma}\cdot\boldsymbol{p}\phi. \tag{1.13}$$

Each of these equations is based on the relativistic energy-momentum relation $E^2 = \boldsymbol{p}^2$ and therefore has one positive and one negative solutions. For $E = |\boldsymbol{p}|$,

$$\boldsymbol{\sigma}\cdot\hat{p}\chi = -\chi, \tag{1.14}$$

and

$$\boldsymbol{\sigma}\cdot\hat{p}\phi = \phi; \tag{1.15}$$

where $\boldsymbol{\sigma}\cdot\hat{p}$ is the helicity operator. χ describes a left-handed neutrino (negative helicity) whereas ϕ describes a right-handed (positive helicity) antineutrino. The other solution with $E = -|\boldsymbol{p}|$ satisfies

$$\boldsymbol{\sigma}\cdot\hat{p}\chi = \chi, \tag{1.16}$$

and

$$\boldsymbol{\sigma}\cdot\hat{p}\phi = -\phi. \tag{1.17}$$

In this case, χ and ϕ describe a right-handed antineutrino and a left-handed neutrino, respectively.

Consider the case $E = |\boldsymbol{p}|$ and the operator

$$P_{R,L} = \frac{1}{2}\left(I \pm \gamma^5\right), \tag{1.18}$$

where

$$\gamma^5 = \begin{pmatrix} -I & 0 \\ 0 & I \end{pmatrix}. \tag{1.19}$$

The action of the operator P_L on the the spinor u gives:

$$\begin{aligned}
P_L u &= \frac{1}{2}(I - \gamma^5)\begin{pmatrix} \chi \\ \phi \end{pmatrix} && (1.20)\\
P_L u &= \frac{1}{2}\left\{\begin{pmatrix} I & 0 \\ 0 & I \end{pmatrix} - \begin{pmatrix} -I & 0 \\ 0 & I \end{pmatrix}\right\}\begin{pmatrix} \chi \\ \phi \end{pmatrix} && (1.21)\\
P_L u &= \frac{1}{2}\begin{pmatrix} 2I & 0 \\ 0 & 0 \end{pmatrix}\begin{pmatrix} \chi \\ \phi \end{pmatrix} && (1.22)\\
P_L u &= \begin{pmatrix} \chi \\ 0 \end{pmatrix} = u_L. && (1.23)
\end{aligned}$$

Similarly,

$$P_R u = \begin{pmatrix} 0 \\ \phi \end{pmatrix} = u_R. \tag{1.24}$$

So, the operator P_L projects out the left-handed spinor u_L whereas P_R projects out the right-handed spinor u_R.

1.2 Chiral Invariance and V−A

The operator γ^5 is referred to as the chirality operator which transforms as:

$$\begin{aligned}
\psi &\rightarrow \gamma^5\psi, \\
\bar{\psi} &\rightarrow -\bar{\psi}\gamma^5.
\end{aligned}$$

With the momentum $\boldsymbol{p}$ along the z-axis, the helicity operator becomes:

$$\boldsymbol{\sigma} \cdot \hat{p} = \sigma_3. \tag{1.25}$$

Since

$$\sigma_3 = \begin{pmatrix} I & 0 \\ 0 & -I \end{pmatrix} \tag{1.26}$$

we have:

$$\boldsymbol{\sigma} \cdot \hat{p} = -\gamma^5. \tag{1.27}$$

It follows that the solutions to the Dirac equation for a massless fermion are eigenstates of γ^5. This is not the case for a massive fermion. However, the wavefunction can be written as a linear combination of the right-handed and left-handed components:

$$\psi = \psi_R + \psi_L, \tag{1.28}$$

where

$$\psi_{R,L} = \frac{1}{2}(I \pm \gamma^5)\psi. \tag{1.29}$$

Consider a 4-fermion interaction $A + B \to C + D$ which is assumed to be invariant under the chiral transformation defined above. The interaction amplitude can be written as:

$$\mathcal{M} = \frac{G}{\sqrt{2}} \left(\bar{\psi}_D O \psi_B\right) \left(\bar{\psi}_C O \psi_A\right). \tag{1.30}$$

Chiral invariance leads to:

$$\bar{\psi}_D O \psi_B = -\bar{\psi}_D \gamma^5 O \gamma^5 \psi_B. \tag{1.31}$$

In order for the amplitude $\mathcal{M}$ to be invariant under a Lorentz transformation, the operator O can be shown to be a linear combination of the following:

Scalar(S)	1
Vector(V)	γ^μ
Axial-vector(A)	$\gamma^\mu\gamma^5$
Tensor(T)	$\sigma^{\mu\nu}$
Pseudoscalar(P)	γ^5

where

$$\sigma^{\mu\nu} = \frac{i}{2}\left(\gamma^\mu\gamma^\nu - \gamma^\nu\gamma^\mu\right). \tag{1.32}$$

It follows that:

$$\gamma^5 O = -O\gamma^5 \tag{1.33}$$

and

$$O\gamma^5 = -O \tag{1.34}$$

$$\gamma^5 O = O. \tag{1.35}$$

Of these five possible operators, only the vector and axial-vector operators V and A anticommute with γ^5. Therefore,

$$O = a\gamma^\mu + b\gamma^5\gamma^\mu. \tag{1.36}$$

From equation (1.34), one has $a = -b$ since $\gamma^5\gamma^5 = I$ and γ^5 anticommutes with γ^μ. The operator O becomes:

$$O = a\gamma^\mu(I - \gamma^5) \tag{1.37}$$

where a is a constant. The amplitude M takes the form:

$$\mathcal{M} = \frac{4G}{\sqrt{2}} J^\mu J^\dagger_\mu, \tag{1.38}$$

where the currents J^μ and $J^\dagger_\mu$ are given below:

$$J^\mu = \frac{1}{2}\bar{\psi}_D\gamma^\mu(I - \gamma^5)\psi_B, \tag{1.39}$$

$$J^\dagger_\mu = \frac{1}{2}\bar{\psi}_C\gamma_\mu(I - \gamma^5)\psi_A. \tag{1.40}$$

This is the modification of the current-current Fermi interaction — at a point — to accommodate the axial-vector contribution originally absent in Fermi's theory.

It should be pointed out that theoretically, one could arrive at a form of the weak charged current in which only S, T and P contribute. However, the experimental evidences are in favor of the (V,A) form.

The following conclusions follow from the V−A form $(\gamma^\mu - \gamma^\mu\gamma^5)$ of the weakly charged current [Che-79]:

- Only left-handed neutrinos and right-handed antineutrinos are coupled to charged leptons by the weak current.

- Parity violation: if P is the parity operator, then $P\psi_L$ leads to a neutrino with positive helicity which is not allowed.

- Charge conjugation violation: if C is the charge conjugation operator, then $C\psi_L$ (where ψ_L describes the neutrino) leads to an antineutrino still with negative helicity: this is not allowed.

- Time reversal (T) is conserved. Since T reverses both spin and momentum, the original state is unchanged.
- CP is conserved because such an operation transforms a left-handed neutrino into a right-handed antineutrino. However, from the studies of the weak decays of the neutral kaon, small CP violation has been established.

Naturally, one would hope that all weak processes are described the V−A interactions with a universal coupling constant.

1.3 Conserved Vector Current Hypothesis

1.3.1 Electromagnetic Current

The Lagrangian density $\mathcal{L}$ in electromagnetic interactions (EM) can be written as:

$$\mathcal{L} = -ieJ_\mu A^\mu, \tag{1.41}$$

where A^μ is the 4-vector potential. The interpretation of J_μ as current follows from the fact that J_μ satisfies the current conservation requirement. For illustration, consider an electron-proton scattering. In one photon-exchange approximation, the scattering amplitude is:

$$\mathcal{M} = -\frac{4\pi\alpha^2}{q^2} J_e^\mu J_\mu^p, \tag{1.42}$$

where the electron current takes the form:

$$J_e^\mu = \bar{u}(k')\gamma^\mu u(k) \tag{1.43}$$

and the proton current is written as:

$$J_\mu^p = \bar{u}(p')\Gamma_\mu(p', p)u(p); \tag{1.44}$$

α is the fine structure constant; k, k' are the initial and final 4-momenta of the electron; p, p' the corresponding 4-momenta of the proton and q is the momentum transferred:

$$q = k - k' = p' - p. \tag{1.45}$$

Γ_μ is constructed from the proton 4-momenta and the γ_μ matrices. Due to Lorentz invariance and parity conservation of EM interactions Γ_μ can only be vectors. Therefore, the hadronic current is:

$$\begin{aligned} J^p_\mu(p,p') &= \bar{u}(p')\left[\gamma_\mu K_1(q^2) + i\sigma_{\mu\nu}(p'-p)^\nu K_2(q^2) + i\sigma_{\mu\nu}(p'+p)^\nu K_3(q^2)\right. \\ &\quad \left. + (p'-p)_\mu K_4(q^2) + (p'+p)_\mu K_5(q^2)\right] u(p). \end{aligned} \tag{1.46}$$

The quantities K_j are functions of q^2 only because $(p'+p)^2$ can be expressed as a function of q^2 and the masses involved. Using the following identities

$$\bar{u}(p')\left[(p'+p)_\mu\right]u(p) = \bar{u}(p')\left[-i\sigma_{\mu\nu}(p'-p)^\nu + (M'+M)\gamma_\mu\right]u(p) \tag{1.47}$$

and

$$\bar{u}(p')\left[i\sigma_{\mu\nu}(p+p')^\nu\right]u(p) = \bar{u}(p')\left[-(p'-p)_\mu + (M'-M)\gamma_\mu\right]u(p) \tag{1.48}$$

the terms involving $(p'+p)$ can be incorporated into other factors and $J^p_\mu(p,p')$ reduces to the following:

$$J^p_\mu = \bar{u}(p')\left[\gamma_\mu F_1(q^2) + i\left(\frac{\kappa}{2M}F_2(q^2)\right)\sigma_{\mu\nu}q^\nu + F_3(q^2)q_\mu\right]u(p), \tag{1.49}$$

where κ is constant and M is the proton mass. The factor $\kappa/2M$ is inserted to make $F_2(q^2)$ coincide with the conventional definition of the EM form factor. The current conservation requirement leads to $F_3(q^2) = 0$ for elastic scattering ($M' = M$). The electric and magnetic form factors $G_E(q^2)$ and $G_M(q^2)$ can be shown to be linear combinations of $F_1(q^2)$ and $F_2(q^2)$. In the non-relativistic limit, $G_E(q^2)$ and $G_M(q^2)$ are interpreted as the Fourier transforms of the charge and the magnetic moment distributions inside the nucleus.

1.3.2 Conserved Vector Current(CVC)

The examination of the EM interactions (equation (1.42)) and weak interactions (equation (1.38)) suggests that G essentially replaces $\frac{(4\pi\alpha^2)}{q^2}$. Therefore G has the dimension of GeV^{-2} while α is dimensionless. By analogy to EM interactions which are mediated by photons, weak interactions are assumed to be mediated by vector bosons. In contrast to the photon, these vector bosons must be massive otherwise they would be directly produced in weak decays. Needless to say, the existence of these vector bosons and their masses have been confirmed experimentally. The decay amplitude is of the form:

$$\mathcal{M} = \frac{g}{\sqrt{2}} J^{\mu} \frac{1}{M_W^2 - q^2} \frac{g}{\sqrt{2}} J_{\mu}^{\dagger}, \tag{1.50}$$

where M_W and q are the mass and the momentum carried by the vector boson mediating the interaction; g is the dimensionless weak coupling constant and the factor $\frac{1}{\sqrt{2}}$ is inserted for the conventional definition of g. In the situations where $q^2 \ll M_W^2$ (β-decay and μ-decay for instance) the interaction is essentially at a point. By comparing equation (1.38) to (1.50) one has:

$$\frac{G}{\sqrt{2}} = \frac{g^2}{8M_W^2}. \tag{1.51}$$

For illustration, consider the neutron-β decay:

$$n \quad \rightarrow \quad p + e^- + \bar{\nu}_e.$$

The decay amplitude is:

$$\mathcal{M} = \frac{G}{\sqrt{2}} H_{\mu} L^{\mu}, \tag{1.52}$$

where H_{μ} and L^{μ} are the hadronic and the leptonic weak current:

$$H_{\mu} \quad = \quad \bar{u}_p \gamma_{\mu} (I - \gamma_5) u_n; \tag{1.53}$$

$$L^{\mu} \quad = \quad \bar{u}_e \gamma^{\mu} (I - \gamma^5) u_{\bar{\nu}_e}. \tag{1.54}$$

The hadronic current can be rewritten as:

$$H_{\mu} \quad = \quad \bar{u_p} \gamma_{\mu} u_n - \bar{u_p} \gamma_{\mu} \gamma_5 u_n \tag{1.55}$$

$$H_{\mu} \quad = \quad V_{\mu} - A_{\mu}, \tag{1.56}$$

where V_{μ} and A_{μ} are the weak hadronic vector and axial-vector currents respectively. Following the arguments used in the EM case, V_{μ} becomes:

$$V_{\mu} = \bar{u}_p \left[\gamma_{\mu} g_v + i \left(\frac{g_m}{2M} \right) \sigma_{\mu\nu} q^{\nu} + \frac{g_S}{2M} q_{\mu} \right] u_n. \tag{1.57}$$

The similarity between V_μ and the EM current (equation (1.49)) should be apparent. In EM, the charge is strictly conserved even for strong interacting particles. Furthermore, EM interactions are vector type of interactions with the coupling constant directly related to the charge:

$$\alpha = \frac{e^2}{4\pi}. \tag{1.58}$$

The weak vector current is assumed to be conserved with a universal coupling constant in an analogy to the EM vector current. This assumption is the CVC hypothesis. The form factor g_s in equation (1.57) vanishes as a result.

The CVC hypothesis can also be formulated using isospin formalism as follows: one defines a spinor

$$\Psi = \begin{pmatrix} u_p \\ u_n \end{pmatrix} \tag{1.59}$$

$$\bar{\Psi} = \left(\bar{u}_p, \bar{u}_n\right). \tag{1.60}$$

Using the Pauli matrices

$$\tau_1 = \begin{pmatrix} 0 & I \\ I & 0 \end{pmatrix} \tag{1.61}$$

$$\tau_2 = \begin{pmatrix} 0 & -i \\ i & 0 \end{pmatrix} \tag{1.62}$$

$$\tau_3 = \begin{pmatrix} I & 0 \\ 0 & -I \end{pmatrix}, \tag{1.63}$$

the EM current J_μ and the weak vector current V_μ are written as:

$$J_\mu = \frac{1}{2}\bar{\Psi}\gamma_\mu \left(I + \tau_3\right)\Psi; \tag{1.64}$$

$$V_\mu = \frac{1}{2}\bar{\Psi}\gamma_\mu \left(\tau_1 + i\tau_2\right)\Psi. \tag{1.65}$$

The EM current consists of the isoscalar part ($\frac{1}{2}\bar{\Psi}\gamma_\mu\Psi$) which satisfies the current conservation requirement:

$$\partial_\mu \left(\bar{\Psi}\gamma^\mu\Psi\right) = 0. \tag{1.66}$$

The isovector currents are as follows:

$$J_\mu(\text{isovector}) = \frac{1}{2}\bar{\Psi}\gamma_\mu\tau_3\Psi; \tag{1.67}$$

$$V_\mu(\text{isovector}) = \frac{1}{2}\bar{\Psi}\gamma_\mu \left(\tau_1 + i\tau_2\right)\Psi. \tag{1.68}$$

The CVC hypothesis assumes that these isovector currents are only different components of the same isospin current

$$I_\mu(\text{isospin}) = \frac{1}{2}\bar{\Psi}\gamma_\mu \tau \Psi. \tag{1.69}$$

J_μ(isovector) is not conserved by itself unless a pionic contribution is added to it; in the case of neutron decay for instance, only a fraction of its lifetime neutron exists as a bare neutron; for the rest of its lifetime, the neutron is a proton surrounded by a "pion cloud". Like J_μ(isovector), V_μ(isovector) needs to be supplemented with a pionic term to satisfy current conservation.

In conclusion, the assumption that the isovector currents J_μ(isovector) and V_μ(isovector) are different components of the same current amounts to attributing the same interaction strength to the pion-lepton vertices as to the baryon-lepton vertices. Furthermore, since strong interactions are charge independent (to a good approximation), one is led to the conservation of isospin — pionic plus baryonic — which is a generalization of conservation of charge.

1.4 Cabibbo Universality

Leptons participate in the weak interactions via the left-handed doublets:

$$\begin{pmatrix} e \\ \nu_e \end{pmatrix} \; ; \; \begin{pmatrix} \mu \\ \nu_\mu \end{pmatrix}.$$

Suppose $V_{e\nu_e}$ and $V_{\mu\nu_\mu}$ are the relative sizes of the (e,ν_e) and (μ,ν_μ) couplings. EM interactions do not distinguish e from μ. Similarly, in weak interactions, $V_{e\nu_e} = V_{\mu\nu_\mu}$ [Got-84]. By redefining the weak coupling constant, $V_{e\nu_e} = V_{\mu\nu_\mu} = 1$. This is the symmetry of the weak interaction under the exchange $(e,\nu_e) \longleftrightarrow (\mu,\nu_\mu)$. Because the neutrinos are massless, $V_{e\nu_\mu} = V_{\mu\nu_e} = 0$. The inclusion of the third doublet of left-handed leptons

$$\begin{pmatrix} \tau \\ \nu_\tau \end{pmatrix}$$

leads to:

$$U = \begin{pmatrix} V_{e\nu_e} & V_{e\nu_\mu} & V_{e\nu_\tau} \\ V_{\mu\nu_e} & V_{\mu\nu_\mu} & V_{\mu\nu_\tau} \\ V_{\tau\nu_e} & V_{\tau\nu_\mu} & V_{\tau\nu_\tau} \end{pmatrix} = \begin{pmatrix} 1 & 0 & 0 \\ 0 & 1 & 0 \\ 0 & 0 & 1 \end{pmatrix}. \tag{1.70}$$

In the quark sector, one has the left-handed fermion states

$$\begin{pmatrix} u \\ d \end{pmatrix}, \quad \begin{pmatrix} c \\ s \end{pmatrix} \text{and} \quad \begin{pmatrix} t \\ b \end{pmatrix}.$$

It is not quite correct to extend the lepton universality to the quarks. That will lead to transitions between $u \longleftrightarrow d$, $c \longleftrightarrow s$ and $t \longleftrightarrow b$ only. However, decays such as $K^+ \rightarrow \mu^+\nu_\mu$ occur. Since K^+ is made up of u and $\bar{s}$ quarks, there must be a weak current which couples u and $\bar{s}$, that is $V_{us} \neq 0$. In order to avoid the introduction of a new coupling constant for quarks — preserve universality — Cabibbo assumed that the weak interaction rotates quark states. Subsequently, Kobayashi and Maskawa generalized Cabibbo's work to three generations:

$$d' = V_{ud}d + V_{us}s + V_{ub}b, \tag{1.71}$$

$$s' = V_{cd}d + V_{cs}s + V_{cb}b, \tag{1.72}$$

$$b' = V_{td}d + V_{ts}s + V_{tb}b. \tag{1.73}$$

In other word, the quark states u, d', c, s', t, b' are eigenstates of the weak interaction while the states u, d, c, s, t, b are the mass eigenstates of the flavor-preserving strong interaction. The weakly charged current J^μ of the quarks is:

$$J^\mu = (\bar{u}, \bar{c}, \bar{u}) \frac{\gamma^\mu (1 - \gamma^5)}{2} U \begin{pmatrix} d \\ s \\ b \end{pmatrix}. \tag{1.74}$$

where U is a 3×3 matrix known as the Cabibbo-Kobayashi-Maskawa (CKM) mixing matrix:

$$U = \begin{pmatrix} V_{ud} & V_{us} & V_{ub} \\ V_{cd} & V_{cs} & V_{cb} \\ V_{td} & V_{ts} & V_{tb} \end{pmatrix}, \tag{1.75}$$

or

$$U = \begin{pmatrix} c_1 & s_1c_3 & s_1s_3 \\ -c_2s_1 & c_1c_2c_3 - s_2s_3e^{i\delta} & c_2c_1s_1 - s_2c_3e^{i\delta} \\ -s_1s_2 & c_1c_3s_2 - c_2s_3e^{i\delta} & c_1s_2s_3 - c_2c_3e^{i\delta} \end{pmatrix}; \tag{1.76}$$

where $c_j = \cos(\theta_j)$, $s_j = \sin(\theta_j)$; θ_j $(j = 1, 2, 3)$ are the Cabibbo angles and $e^{i\delta}$ is a phase factor. At four-quark (u, d, c, s) level U reduces to a real 2×2 matrix and the theory can be shown to be CP invariant. However, with the extension to t and

b quarks, the mixing matrix contains a phase factor and for that reason the theory violates CP [Hal-84].

The implication is that for nuclear beta decays involving only vector interactions, one must replace the coupling constant G of equation (1.51) by

$$G_V = GV_{ud}. \tag{1.77}$$

In the case of a pure leptonic decay (μ-decay for instance), there is no mixing:

$$G_\mu = G. \tag{1.78}$$

The top row the CKM matrix (equations 1.75 and 1.76) provides the unitarity test

$$|V_{ud}|^2 + |V_{us}|^2 + |V_{ub}|^2 = 1 \tag{1.79}$$

which must be satisfied if the Standard Model with three generations is correct.

1.5 Superallowed Fermi Decay

1.5.1 Nuclear Beta Decay

The transition probability per unit time in nuclear β-decay is given by the golden rule:

$$P(E)dE = \frac{2\pi}{\hbar}|M_{if}|^2\rho(E), \tag{1.80}$$

where $\rho(E)$ is the density of final states. The matrix element M_{if} includes a summation over all possible angular momentum states of the leptons, over all final spin states of the nucleus and an average over the spin orientations of the initial nucleus. For convenience, the nucleus is assumed to be infinitely heavy and therefore carries no energy but contributes the necessary recoil momentum for the leptons [Hor-75]. The density of final states is:

$$\rho(E) = \frac{dN_e dN_\nu}{dE_o}, \tag{1.81}$$

where dN_e and dN_ν are the number of states available to the β-particle and the neutrino in the momentum intervals p to $p + dp$ and q to $q + dq$ respectively and E_o

is the total energy carried by the leptons:

$$dN_e = 4\pi p^2 \frac{dp}{h^3}, \tag{1.82}$$

$$dN_\nu = 4\pi p^2 \frac{dp}{h^3}, \tag{1.83}$$

$$E_o = E_e + E_\nu. \tag{1.84}$$

From the energy-momentum relations of the leptons, one has:

$$qdq = (E_o - E_e)dE_o, \tag{1.85}$$

$$\frac{dq}{dE_o}q^2 = \frac{E_o - E_e}{c^3}\sqrt{(E_o - E_e)^2 - m_\nu c^4}\, dp \tag{1.86}$$

and

$$pc^2 dp = E_o dE_o. \tag{1.87}$$

Neglecting the neutrino mass, the transition probability becomes:

$$P(\epsilon) = \frac{m_e^5 c^4}{2\pi^3 \hbar^7}|M_i f|^2 \epsilon(\epsilon_o - \epsilon)^2 \sqrt{\epsilon^2 - 1}, \tag{1.88}$$

where

$$\epsilon = \frac{E_e}{m_e c^2} \tag{1.89}$$

and

$$\epsilon_o = \frac{E_o}{m_e c^2}. \tag{1.90}$$

The matrix element M_{if} is given by equation (1.52) with G_β instead of G. One rewrites the matrix element as:

$$M_{if} = \frac{G_\beta}{\sqrt{2}} M_h M_l, \tag{1.91}$$

where the lepton matrix element M_l is given by equation (1.50) and the hadron matrix element M_h generally comprises a vector and an axial vector contributions:

$$M_h = V M_\beta \tag{1.92}$$

where V is the vector necessary to construct M_h. With equation (1.91), the transition probability is:

$$P(\epsilon) = G_\beta^2 \frac{m_e^5 c^4}{2\pi^3 \hbar^7}|M_\beta|^2 \epsilon(\epsilon_o - \epsilon)^2 \sqrt{\epsilon^2 - 1}\, F(Z, \epsilon), \tag{1.93}$$

where the factor $F(Z,\epsilon)$, known as the Fermi Function, includes among other things, correction factors such as screening effects by atomic electrons and final state Coulomb interaction effects which are particularly important at low e/e^+ energies and for high-Z nuclei. By integration the transition probability over the β energy spectrum, the decay rate is:

$$\Gamma = G_\beta^2 \frac{m_e^5 c^4}{2\pi^3\hbar^7} |M_\beta|^2 f(Z,\epsilon_o), \tag{1.94}$$

with

$$f(Z,\epsilon_o) = \int_0^{\epsilon_o} F(Z,\epsilon)(\epsilon_o-\epsilon)^2 \sqrt{(\epsilon^2-1)}\,\epsilon d\epsilon. \tag{1.95}$$

The product ft of the Fermi integral function f and the decay half live $t_{1/2}$ is independent of kinematic effects and involves only the matrix element:

$$ft = f(Z,\epsilon_o)\left(\frac{\ln 2}{\Gamma}\right), \tag{1.96}$$

$$ft = \frac{K}{G_\beta^2 |M_\beta|^2}, \tag{1.97}$$

where K is a product of fundamental constants. In cgs units,

$$K = \frac{2\pi^3(\ln 2)\hbar^7 c^6}{(m_e c^2)^5} = 8.1201 \times 10^{-7}. \tag{1.98}$$

1.5.2 Superallowed Fermi Decay

Superallowed transitions are β-transitions between two members of an isospin multiplet — for instance a hadron A of spin zero decaying into another spinless hadron with the same parity. In this particular case, the axial vector contribution to the matrix element M_h vanishes because since there is no spin, it is impossible to construct an axial vector out of two hadron momenta alone. These types of transitions are pure vector interactions known as Fermi transitions and can be used to test the CVC hypothesis. The coupling constant G_β is the same as G_V given in equation (1.77). In addition, the matrix element M_β which is known as M_F for pure Fermi transitions, can be evaluated without reference to the details of the nuclear wavefunctions. Since both states belong to the same isomultiplet differing only in their values of τ_3 (see equation (1.59)), M_F is the matrix element of the isospin raising or lowering operator $\tau_\pm$:

$$\tau_\pm = \tau_1 \pm i\tau_2, \tag{1.99}$$

$$M_F = < \tau, \tau_3 \pm 1|\tau_\pm|\tau, \tau_3 >, \tag{1.100}$$

From angular momentum theory,

$$M_F = \sqrt{(\tau \mp \tau_3)(\tau \pm \tau_3 + 1)}. \tag{1.101}$$

For all superallowed transitions of the type $(0^+, \tau = 1) \rightarrow (0^+, \tau = 1)$

$$M_F = \sqrt{2} \tag{1.102}$$

and

$$ft = \frac{1}{2}\frac{K}{G_V^2}. \tag{1.103}$$

Chapter 2

Motivation

Pion beta decay ($\pi^+ \rightarrow \pi^0 e^+ \nu_e$) is one of the fundamental semileptonic weak interaction processes. It is a transition between two spin-zero members of an isospin triplet and is therefore analogous to the superallowed pure Fermi transitions in nuclear beta decay. At tree level, the rate of pure Fermi nuclear beta decay is directly related to the vector coupling constant G_V and the nuclear Fermi matrix element M_F. The Conserved Vector Current hypothesis (CVC) predicts that the product ft of the Fermi integral function f and the decay half live $t_{1/2}$ is a universal constant given by:

$$ft = \frac{K}{G_V^2 |M_F|^2}, \tag{2.1}$$

where K is given by equation (1.98). By comparing the vector coupling constant of the nucleon beta decay G_V to that of the muon decay, it is possible to determine V_{ud}, the mixing matrix element between the u and d quarks. Cabibbo universality relates G_V to the muon weak coupling constant G_μ via the CKM matrix element V_{ud} [Shr-78]

$$G_V^2 = G_\mu^2 \times V_{ud}^2 \times (1 - \Delta_\beta) \times (1 + \Delta_\mu). \tag{2.2}$$

G_μ is the muon decay coupling constant (see equation (1.78)); Δ_μ and Δ_β are the inner radiative corrections for μ and β decays respectively. The inner radiative corrections do not depend on the electron energy. They do depend however on the details of the strong interaction involved and the structure of the decay. In addition, they are model-dependent and tend to diverge theoretically. They are relevant when comparing different types of beta decay but act only to renormalize the coupling constant when comparing the rates of beta decays of the same type. In such cases, they are directly defined into the coupling constants themselves. Some $0^+ \to 0^+$ nuclear beta decay processes, characterized by the single parameter V_{ud} are as follows:

$$\begin{aligned} {}^{34}\mathrm{Cl} &\longrightarrow {}^{34}\mathrm{S}\, e^+\nu_e \\ {}^{26}\mathrm{Al} &\longrightarrow {}^{26}\mathrm{Mg}\, e^+\nu_e \\ {}^{14}\mathrm{O} &\longrightarrow {}^{14}\mathrm{N}\, e^+\nu_e. \end{aligned}$$

For instance, the third reaction represents the transition from the ground state of ^{14}O with $(\tau = 1, \tau_3 = 1)$ to the first excited state of ^{14}N with $(\tau = 1, \tau_3 = 0)$.

Two types of nucleus-dependent corrections must be applied to equation (2.1) in order to extract G_V from the measured decay rates: the phase space dependent radiative corrections δ_R to the statistical rate function f $(f_R = f(1+\delta_R))$ and the nuclear structure dependent corrections δ_C to the matrix element M_F $(|M_F|^2 = |M_{F_o}|^2(1-\delta_C))$. The uncorrected Fermi matrix element M_{F_o} is given by equation (1.101). Taking into account the corrections δ_R and δ_C and the matrix element of equation (1.102), the nucleus independent ft value becomes

$$\mathcal{F}t = ft \times (1+\delta_R) \times (1-\delta_C); \tag{2.3}$$

$$\mathcal{F}t = \frac{K}{2 \times {G_V}^2}. \tag{2.4}$$

where the uncorrected Fermi integral function f and the decay half live t are given by equations (1.95) and (1.96). The empirical values of G_V are determined from the $\mathcal{F}t$ values.

The outer radiative corrections δ_R are model-independent and uniquely specified. They include the inner bremsstrahlung and contain a dependence of the beta particle energy. In addition, they are discussed in terms of orders of α, the fine structure constant. They originate from, for instance, the emission of virtual photons by the final state charged particles. The zeroth and the first order outer radiative corrections are shown in figure 2.1. In the course of the past two decades, radiative corrections of $\mathrm{O}(\alpha)$ have been calculated as well as the leading terms of $\mathrm{O}(Z\alpha^2)$ [Sir-87a].

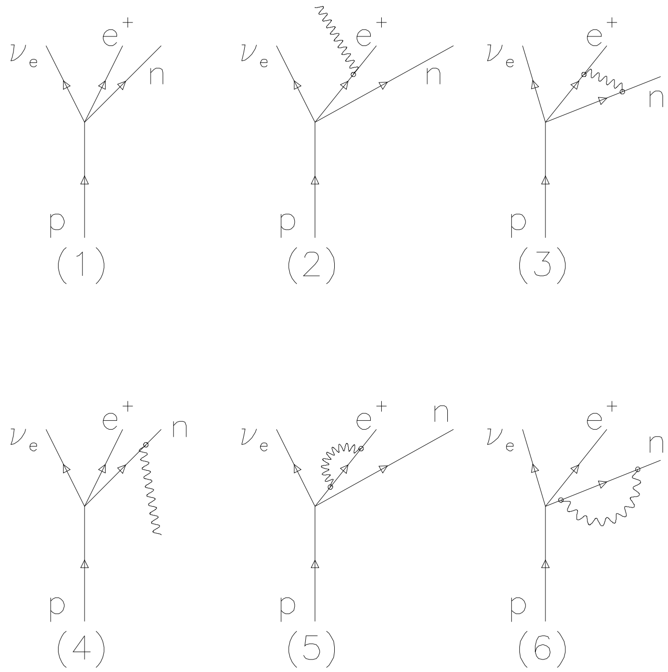

Figure 2.1: Feynman diagrams for the beta decay of a point nucleon: (1) no radiative correction; (2)–(6) first order radiative corrections.

The resulting radiative corrections (inner plus outer) amount to $3-4\%$ with theoretical uncertainty of 0.2% arising mainly from short-distance axial-vector-induced contributions [Mar-86].

The nucleus structure dependent corrections δ_C are conventionally factorized into two components: isospin impurity and radial overlap corrections. The fact that M_{F_o} is given by equation (1.101) rests on the assumption that the states involved are pure isospin states and eigenstates of a charge independent hamiltonian. Even after accounting for Coulomb interactions and spin-orbit coupling of the nucleus, the nuclear force is still slightly charge dependent [Bli-73]. As a result, the nuclear states involved in the decay are not pure isospin states. The radial overlap corrections are due to small differences in the single-particle radial wave functions of the neutron and the proton. Due to these differences, the radial overlap integral of the parent and the daughter nucleus deviates from unity. The evaluation of the isospin impurity correction is performed by adding an isospin nonconserving (INC) interaction term to the standard shell-model hamiltonian while the radial overlap correction is based on the radial wave functions obtained from a suitable parametrization of the mean field. There have been three systematic evaluations of δ_C by Tower, Hardy and Harvey (THH) [Tow-77], Wilkinson (W) [Wil-78] and Ormand and Brown (OB) [Orm-85] and [Orm-89]. The THH calculations of δ_C were carried out as follows: the radial wave functions were obtained from a Woods-Saxon plus Coulomb potential and the INC interaction term was determined by:

- adding Coulomb matrix elements to the proton-proton hamiltonian,
- increasing the $\tau = 1$ part of the proton-neutron interaction by 2%,
- determining the single-particle energies from closed-core plus proton and neutron nuclei [Orm-89].

On the other hand, the OB calculations of δ_C were based on an INC interaction that was determined empirically by requiring that the parameters of a Coulomb plus phenomenological isovector and isotensor potential reproduce the experimental isotopic mass splittings. The OB radial wave functions were obtained from a self-consistent Hartree-Fock calculation with a Skyrme-type interaction which also included a Coulomb exchange term. The most recent and theoretically refined is the OB calculation which yields a corrected $\mathcal{F}t$ of 0.2% or 3σ higher than that determined using THH δ_C's. As shown in table 2.1, both OB and THH values of δ_C yield essentially constant but inconsistent averaged $\mathcal{F}t$ values. The THH and OB nuclear corrections yield 0.9746 ± 0.001 and 0.9737 ± 0.001 respectively for V_{ud}; the errors quoted are dominated by the uncertainties in δ_R mentioned above. Furthermore, considering the accepted value for $V_{us} = 0.220 \pm 0.002$ and $V_{ub} < 0.0075$ (90%

			$\delta_C(\%)$		$\mathcal{F}t$	
Nucleus	ft	$\delta_R(\%)$	OB	THH	OB	THH
^{14}O	3038.1(23)	1.53(1)	0.19(13)	0.33(10)	3078.7(47)	3074.4(37)
^{26m}Al	3034.5(14)	1.47(2)	0.24(13)	0.34(11)	3071.7(44)	3068.6(37)
^{34}Cl	3052.0(29)	1.45(3)	0.48(14)	0.85(12)	3081.4(53)	3070.0(47)
^{38m}K	3045.1(26)	1.44(3)	0.49(17)	0.70(12)	3081.1(76)	3067.3(48)
^{42}Sc	3048.7(63)	1.46(4)	0.39(13)	0.48(12)	3081.1(76)	3078.4(76)
^{46}V	3043.7(22)	1.46(4)	0.21(13)	0.40(12)	3081.6(49)	3075.7(46)
^{50}Mn	3039.9(40)	1.46(5)	0.28(13)	0.43(13)	3075.6(59)	3071.0(59)
^{54}Co	3044.7(23)	1.45(5)	0.35(13)	0.60(12)	3077.1(49)	3070.3(48)
Average					3077.3(19)	3071.5(16)
χ^2/ν					0.63	0.64

Table 2.1: List of ft values, corrections and "nucleus independent" $\mathcal{F}t$ values obtained by THH and OB for various nuclei.

confidence level), one gets for $|V_1|^2 = |V_{ud}|^2 + |V_{us}|^2 + |V_{ub}|^2$ values of 0.9982 ± 0.0021 and 0.9965 ± 0.0021 for THH and OB calculations respectively. The OB calculations imply violation of CKM unitarity at the 90% confidence level.

Recently, Drukarev and Strikman discovered that the β electron final state interaction effects (Coulomb screening corrections) are more pronounced than previously thought. This effect moves the central value of V_{ud} away from unitarity.

Hardy et al. [Har-90] studied the spread of the THH and OB's δ_C, did a critical survey of available superallowed beta decay data and took unweighted averages. As a result, Hardy et al. removed the discrepancy of THH and OB calculations and reduced the overall uncertainties, bringing the unitarity test to

$$|V_{ud}|^2 + |V_{us}|^2 + |V_{ub}|^2 = 0.9962 \pm 0.0016, \tag{2.5}$$

a value which is 2.4σ lower than the Standard Model prediction.

From neutron beta decay, V_{ud} can be extracted knowing the neutron lifetime τ_n and G_A/G_V, the ratio of the weak axial vector to the vector coupling constants. A new precision measurement of the electron asymmetry in neutron decay [Ero-90] yields a new value for the ratio $G_V/G_A = -1.2570 \pm 0.0028$. This result, combined with the average value of the neutron lifetime, 888.8 ± 2.4s gives $V_{ud} = 0.9804 \pm 0.0022$

which leads to the unitarity test of

$$|V_{ud}|^2 + |V_{us}|^2 + |V_{ub}|^2 = 1.0096 \pm 0.0044. \tag{2.6}$$

This value is higher than the Standard Model prediction by 2.2σ.

The pion beta decay, proceeding solely via the weak vector current interaction, constitutes a superallowed transition from which V_{ud} can be determined. Given the discrepancy between the nuclear beta decay and the neutron beta decay results discussed above, the determination of the pion beta decay rate at the level of half a percent is of a clear importance and constitutes an independent test of universality in the meson sector.

Contrary to nuclear beta decay, pion beta decay is free of the nuclear overlap correction as well as the screening corrections. Sirlin [Sir-78] has calculated the $\pi\beta$ decay rate taking into account the effects of radiative corrections, δ_π^0 which involve only an axial-vector contribution [Mar-86].

$$\frac{1}{\pi_\beta} = \ln 2 \frac{30}{(\mathcal{F}t)} \left(\frac{\Delta}{m_e}\right)^5 \left(1 - \frac{\Delta}{2m_{\pi^+}}\right)^3 \mathcal{K}(\epsilon, \Delta) \left(1 + \delta_\pi^0\right), \tag{2.7}$$

where

$$\mathcal{K}(\epsilon, \Delta) = \sqrt{1-\epsilon}\left(1 - \frac{9\epsilon}{2} - 4\epsilon^2\right) + \frac{15\epsilon^2}{2} \ln\left(\frac{1+\sqrt{1-\epsilon}}{\sqrt{\epsilon}}\right)^2 - \frac{3}{7}\left(\frac{\Delta}{m_{\pi^+} + m_{\pi^0}}\right)^2 \tag{2.8}$$

and

$$\epsilon = \left(\frac{m_e}{\Delta}\right)^2 = \left(\frac{m_e}{m_{\pi^+} - m_{\pi^0}}\right)^2. \tag{2.9}$$

This result may be compared to the one obtained in chapter 4 without radiative corrections.

This theoretical advantage of the pion beta decay is offset by experimental difficulties. In fact, the main disavantage of the pion beta decay is its small branching ratio $\sim 10^{-8}$ which makes it a very difficult process to study with precision. The most precise measurements of the pion beta decay rate to date are as follow:

Using a stopped pion method, Depommier et al. [Dep-68] measured the branching ratio for the pion beta decay at CERN. They observed 332 ± 10 pion beta events for 1.48×10^{11} π^+ stopped in their apparatus. This led to a decay rate of $0.38^{+0.03}_{-0.04}\mathrm{s}^{-1}$.

Their result is in good agreement with theory but the experimental error is too large for a significant test of CVC.

The most recent and most precise measurement of the $\pi\beta$ decay rate is due to McFarlane et al. [McF-85] who performed an in-flight decay measurement at LAMPF. Their result $((0.394 \pm 0.015)\mathrm{s}^{-1})$, though in good agreement with theoretical predictions $((0.4027 \pm 0.0018)\mathrm{s}^{-1})$ is not precise enough ($\sim 4\%$ overall uncertainties) to test the full extent of the radiative corrections which stand at $\sim 3\%$.

A precision determination of the pion beta decay rate is being carried out in a two stage program at the Paul Scherrer Institute (PSI) in Switzerland. The first phase of the experiment is expected to yield a decay rate with an overall uncertainty of 0.5%. At this level of precision, a test of CVC and the radiative corrections will be possible. In addition, the superallowed Fermi decay data could be compare to the neutron beta decay. The second stage of the experiment will reduce the uncertainties still further to the level of $0.2-0.3\%$ which will test the CKM unitarity and constrain the following extensions to the minimal Standard Model:

- The existence of a fourth generation of fermions which could be inferred from an experimental violation of the CKM unitarity. At present, from the nuclear Fermi decay data, an upper bound of 0.07 (at 90% confidence level) is set on the mixing matrix element resulting from a fourth generation of quarks.

- The existence of other gauge bosons Z' in addition to the known γ and Z of electroweak theory. Marciano [Mar-87] and Sirlin [Sir-89] have computed quantum loop corrections to the quark mixing angles resulting from several types of Z'.

- Compositeness of fermions and gauge bosons which participate in weak interactions. The experimental limits on the validity of quark-lepton universality can be used to constrain the mass scale of compositeness.

Chapter 3

Pion Beam

This chapter introduces the production of the positive pions which are needed for the experiment. A general description of the accelerator which delivers the particle beam is presented. The development runs, intended to optimize of the beam channel for pure pion beam and minimal pion stopping volume are also discussed in conjuction with the results of these runs.

The accelerator facility at Paul Scherrer Institute (PSI) offers a large variety of intense particle beams and irradiation possibilities. The facility comprises three cyclotrons known as Injector 1, Injector 2 and the Ring. For the purposes of the pion beta decay experiment, Injector 2 and the Ring are relevant. Injector 2 delivers 72 MeV protons to the Ring which in turn accelerates them to 590 MeV. These protons are transported to two graphite production targets of length 7 mm (Target M) and 60 mm (Target E) in the direction of the proton beam. At Target E, five secondary beams are extracted, one of which is the $\pi E1$ beam used by various experiments including pion beta decay experiment mentioned in the previous chapter. Some properties of the Ring are summarized in table 3.1.

3.1 $\pi E1$ Beam Line

Particles from target E are extracted at an angle of 10° with respect to the proton beam direction for the $\pi E1$ beam line which transports pions and muons of momenta ranging from 10 to 500 MeV/c. The $\pi E1$ channel can be operated in two regimes: The first mode offers high fluxes with low momentum resolution. The range of

Injection Energy	72 MeV
Extraction Energy	590 MeV
Extraction Momentum	1206 MeV/c
Energy Spread (FWHM)	ca. 2%
Beam Emittance	ca. 2πmm $\times$ mrad
Beam Current	1 mA DC
Accelerator Frequency	50.63 MHz
Time Between Pulses	19.75 ns
Bunch Width	ca. 1 ns

Table 3.1: Properties of the PSI Ring Accelerator.

momenta is limited to 280 MeV/c. The second regime is a low acceptance mode with high momentum resolution up to 500 MeV/c. The characteristics of the $\pi E1$ beam line are listed in table 3.2; figure 3.1 is a sketch of the beam channel.

Mode of operation	1	2
Channel Length(m)	16	16
Maximum Momentum (MeV/c)	280	500
Solid Angle (msr)	32	13
Momentum Acceptance (FWHM)	7.8%	8.0%
Momentum Resolution (FWHM)	0.8%	0.26%
π^+ Stop Density (/g mA s)	2.5×10^7	1×10^7

Table 3.2: Some characteristics of the $\pi E1$ Channel.

3.2 Beam Contaminations and Phase Space

3.2.1 Optimization and Time of Flight Analysis

The first task for beam set-up is to set the magnet for the desired pion rate while minimizing the muon and positron contaminations. At a given pion momentum, the nominal magnet settings are used as the initial inputs of an optimization algorithm. With these initial settings, the optimization algorithm known as OPTIMA calculates the particle rate in a scintillator counter placed at a waist. Then, for each unit

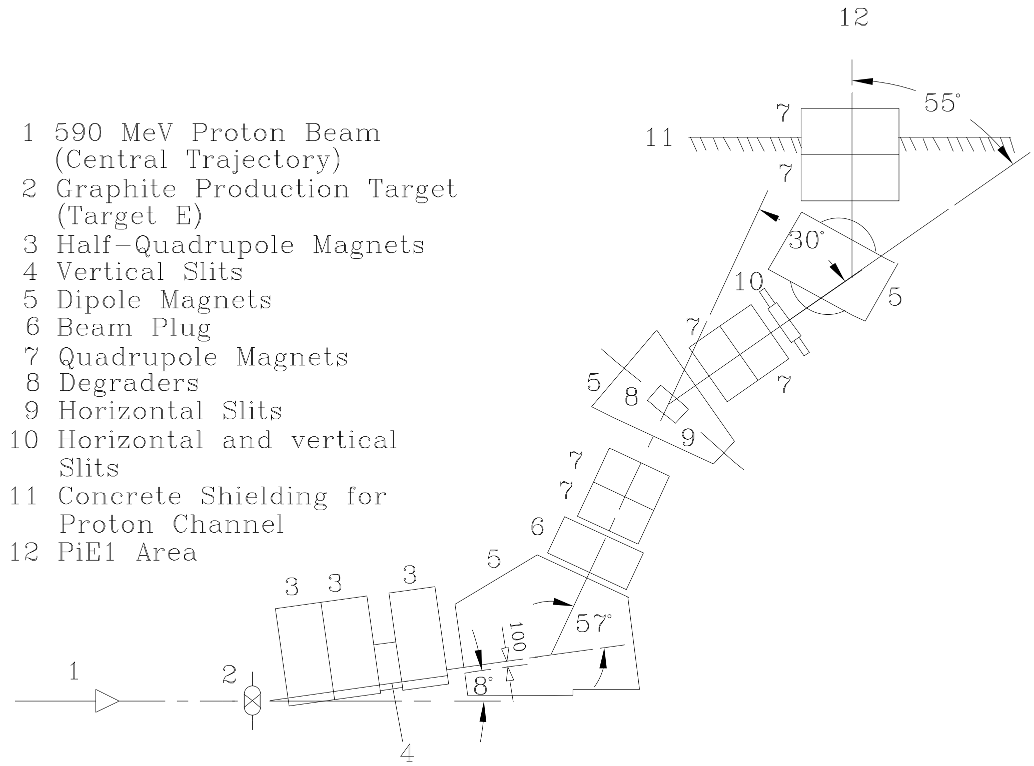

Figure 3.1: The $\pi E1$ Beam Line. This is the standard part of the channel. The continuation of the beam line displayed in figure 3.2 or figure 3.6, is adjustable according to the experiment.

in the beam channel except the momentum defining magnet, OPTIMA varies the corresponding setting within a given range with a given step size around the initial value for a maximum rate in the scintillator. The observed counting rate in the scintillator is normalized to the proton rate during the counting period to account for fluctuations in the primary proton current. When all the magnets are set at their optimum values, OPTIMA calculates again the rate in the scintillator and returns the ratio of the final rate to the initial rate as the gain. An iterative process is then performed until the gain is close to unity. The beam line set-up and the electronics diagram for optimization purposes during the test run of 1992 is shown in figure 3.2 and figure 3.3 respectively. The MWPC monitors the horizontal and vertical beam profiles at the waist. A time of flight (TOF) analysis is conducted before and after

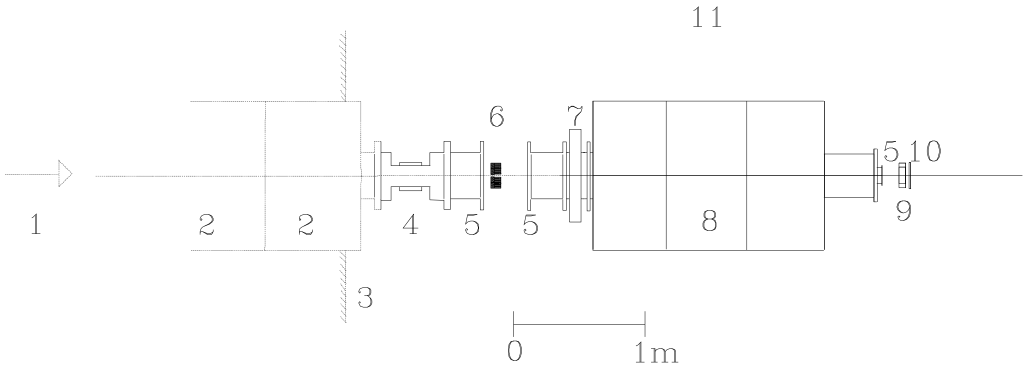

Figure 3.2: Beam line set-up for optimization during the test run of 1992: 1) secondary beam (central trajectory); 2) quadrupole magnets; 3) concrete shielding for proton channel; 4) vertical steering magnet; 5) mylar windows, 6) lead collimator(opening: 7 cm vertical, 2 cm horizontal, thickness 7.5 cm; 7) horizontal steering magnet; 8) quadrupole triplet; 9) multi-wire proportional chamber(MWPC); 10) scintillator $40 \times 40 \times 3\text{mm}^3$, 11) $\pi E1$ area.

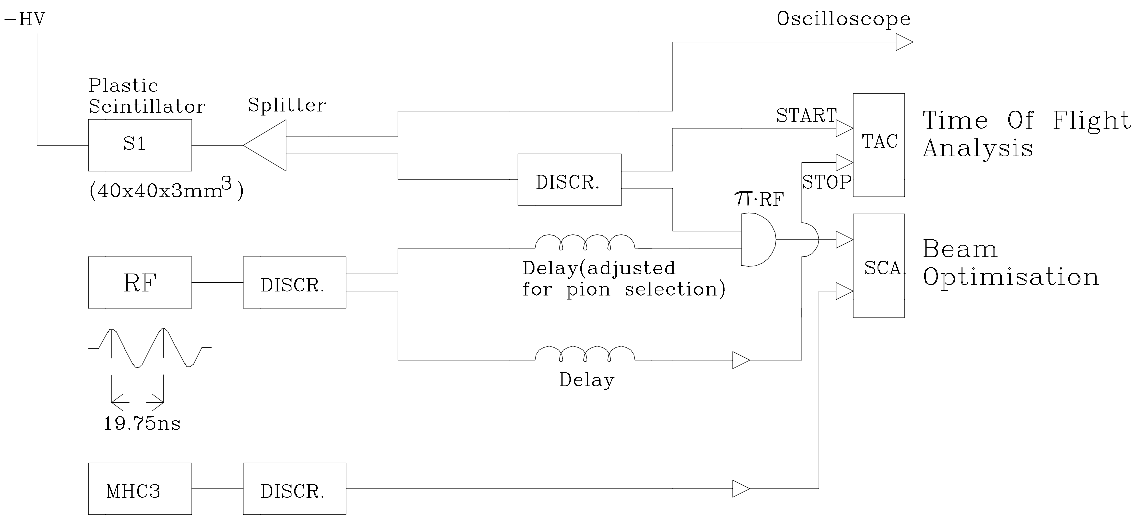

Figure 3.3: Electronics diagram for beam optimization and Time Of Flight analysis.

the optimization in order to determine the fractions of pions and the contaminating particles (muons and positrons) in the beam. The optimization scintillator provides the start signal for the Time to Analog Converter while the stop signal is the suitably

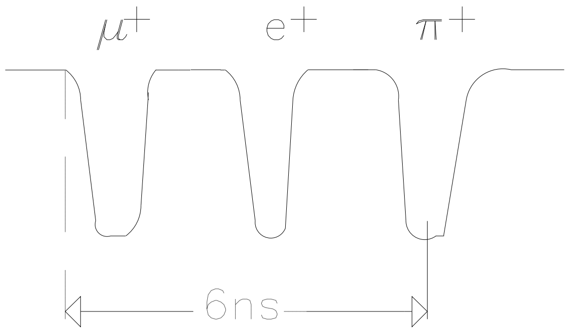

Figure 3.4: Time separation observed on the oscilloscope between π^+, μ^+ and e^+ at 116 MeV/c.

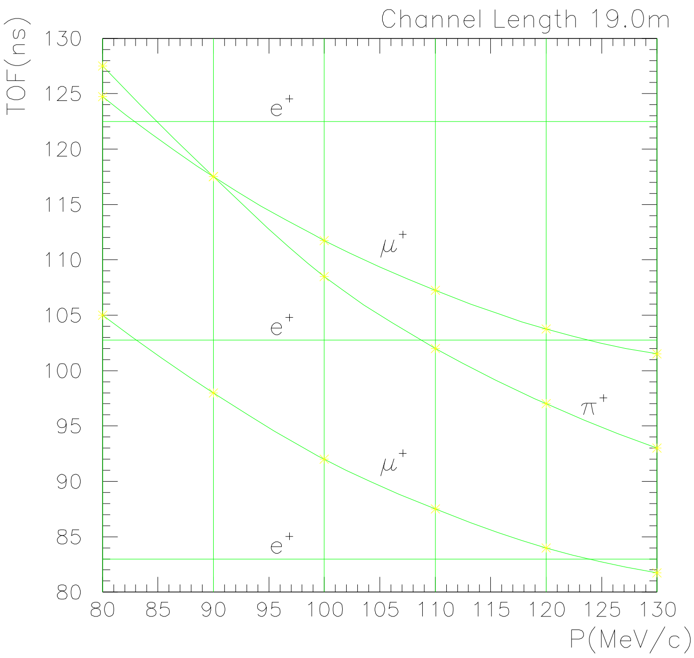

Figure 3.5: Time of flight in the secondary beam line of π^+, μ^+ and e^+ at various momenta. For the pion beta experiment, the central beam momentum is set at 116 MeV/c.

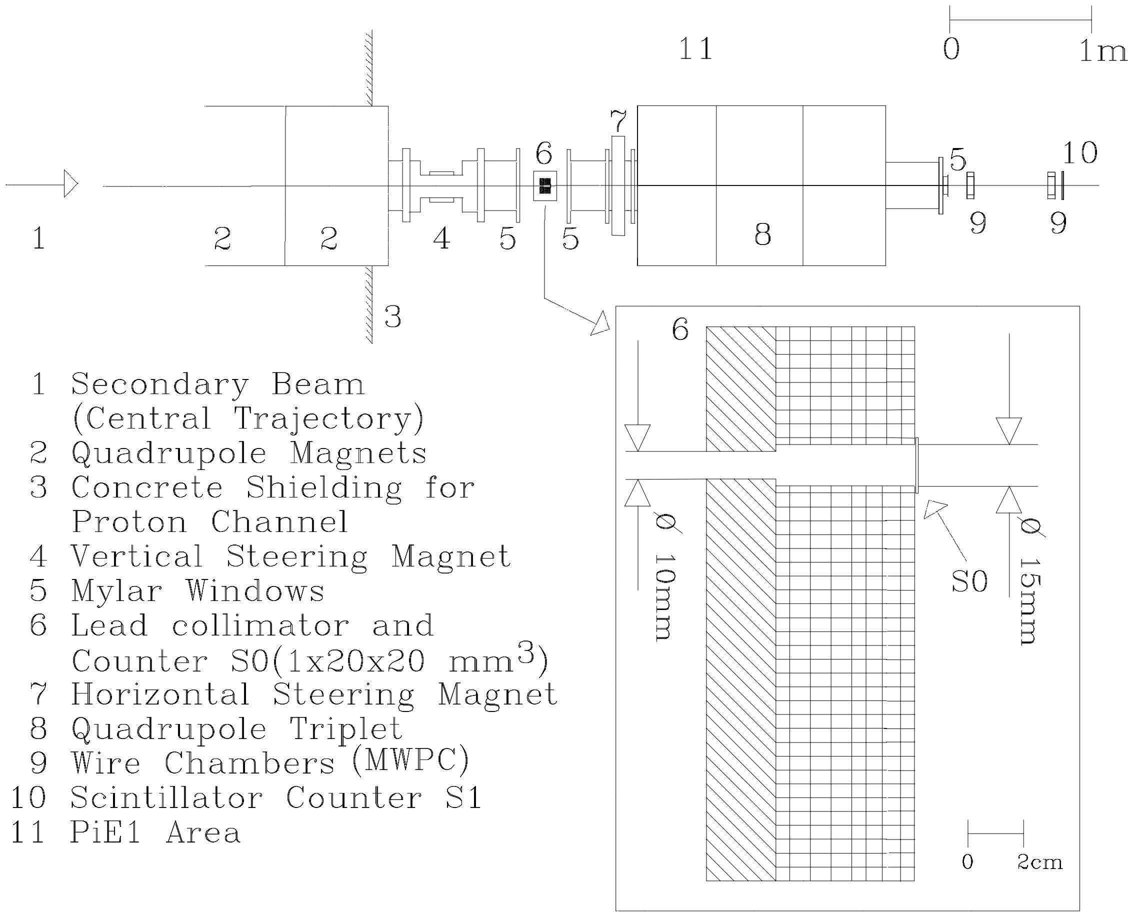

Figure 3.6: Beam line arrangement for phase space studies during the 1993 test run.

delayed RF signal, which marks a particular phase of the accelerator frequency (see table 3.1). The optimization branch of the electronics involves the selection of the particle type — π^+ in this case — for which the magnets are to be optimized using the coincidence, $\pi \cdot \mathrm{RF}$, in figure 3.3. Triggering an oscilloscope with the scintillator and looking at the RF, one observes at 116 MeV/c, a clean separation between particle types as shown in figure 3.4. This observation agrees well with the expected separation displayed in figure 3.5. Once the selection is made, the coincidence output is sent to a scaler whose counts are used by the optimization algorithm.

3.2.2 Contaminations and Beam Profiles

Following the optimization and TOF analysis, a system of two MWPC is set up along the beam to monitor the horizontal and vertical beam profiles and to determine the divergences. The beam line set-up during the test run in 1993 is shown in figure 3.6.

Type	Spot size(cm)	Divergence(mr)
Horizontal	0.77	45.50
Vertical	0.97	89.10

Table 3.3: $\pi E1$ beam characteristics (Full Width Half Maxima) as measured during the 1993 test run.

The position of the first wire chamber is the waist where the beam spot size is expected to be minimal. If the hits in the MWPC's shown in figure 3.6 are $(X1, Y1)$ and $(X2, Y2)$ respectively, the divergences are defined as follow:

$$X' = \frac{X2 - X1}{D} \tag{3.1}$$

and

$$Y' = \frac{Y2 - Y1}{D}, \tag{3.2}$$

where D is the distance between the two MWPC's. The horizontal and vertical characteristics of the beam during the test run of 1993 are shown in figure 3.7. The Full Width Half Maxima (FWHM) of the beam profiles and the divergences are presented in table 3.3.

The horizontal and vertical phase spaces (X, X') and (Y, Y') are shown in figure 3.8. A two-dimensional display of the of the energy deposited in the scintillator (see

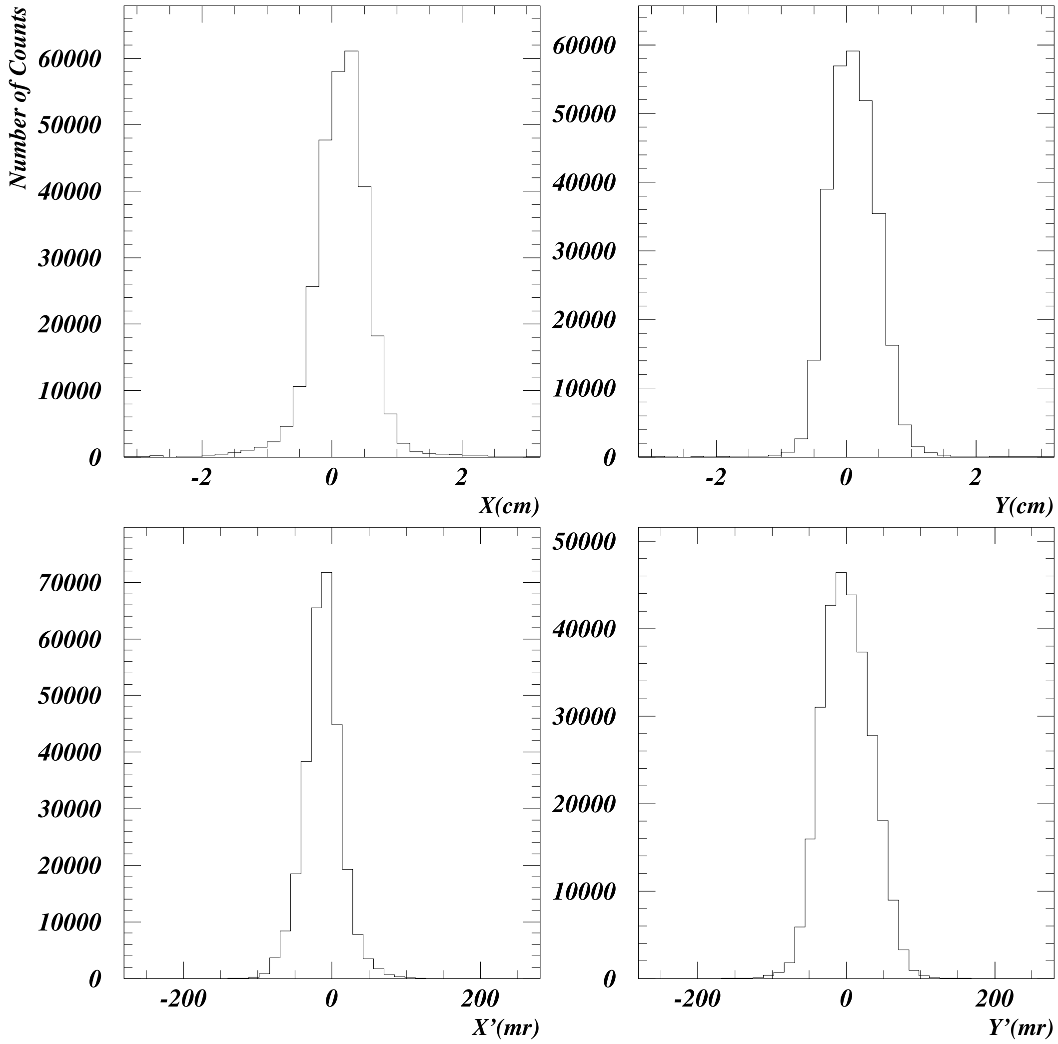

Figure 3.7: Beam profiles and divergences as measured during the 1993 test run.

figure 3.6) versus the timing of the RF signal reveals the composition of the beam as can be seen in figure 3.10, and allows a quantitative determination of the particle rates. The rates and contaminations based on these cuts are summarized in table 3.4.

	Rates(s^{-1})	Contaminations
Scintillator S1	9.70×10^5	
π^+	6.50×10^5	
μ^+	0.95×10^5	$\mu^+/\pi^+ = 14.61\%$
e^+	0.56×10^5	$e^+/\pi^+ = 8.62\%$

Table 3.4: Beam particle rates and contaminations. The average proton current during the run was 670μA. The π^+ beam-momentum was 116MeV/c, and the momentum spread was 2% (FWHM).

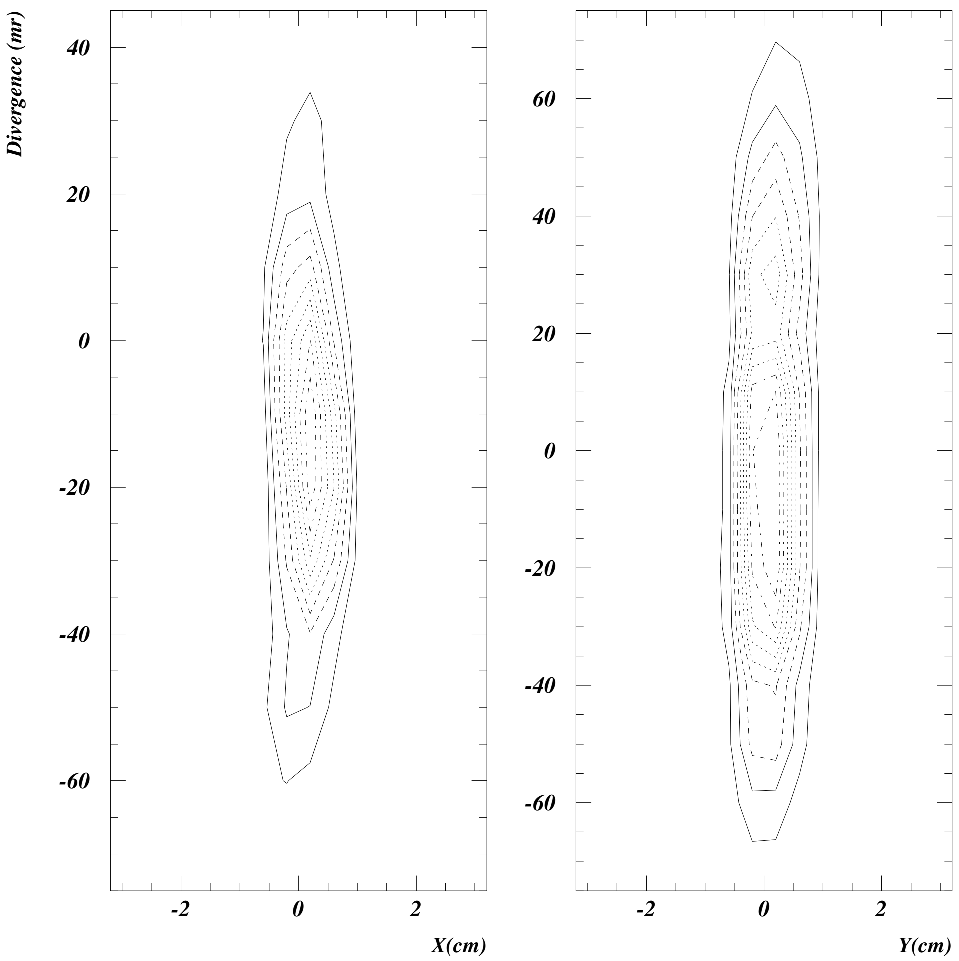

Figure 3.8: Horizontal and vertical phase spaces (X, X') and (Y, Y') at the waist.

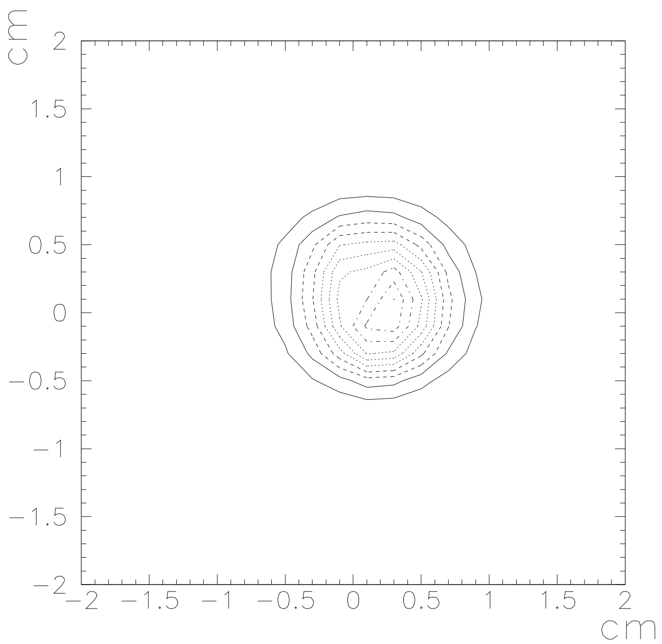

Figure 3.9: Beam spot at the waist. With a diameter less than one centimeter, the measured beam spot satisfies the requirement for the pion beta experiment.

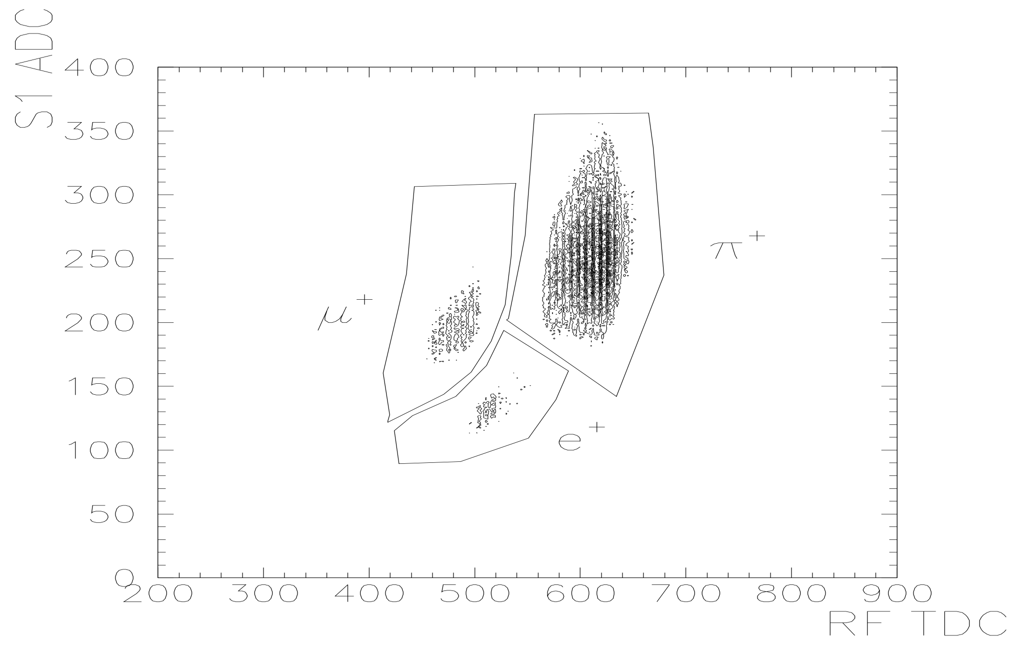

Figure 3.10: Scintillator ADC versus RF timing (TDC). The muon regions to the left, the positron regions below the muon band but slightly to the left and the pion regions to the right are clearly visible. By making cuts on the regions, the rates of the beam particles at the scintillator can be determined.

Chapter 4

Pion Decay Channels

In this chapter, the kinematics and the decay rates for the pion decay channels relevant to the experiment are presented. This is necessary for the understanding of the experimental apparatus and its design which are discussed in the subsequent chapters. The pion beta and the $\pi^+ \to e^+\nu_e$ decays, being the processes of interest, are discussed thoroughly. The other decay modes which act as background processes are introduced to varying degrees.

4.1 Pion Beta Decay

The processes known as pion beta decays or pibeta are the beta decays of the charged pions:

$$\begin{aligned} \pi^+ &\longrightarrow \pi^0 e^+ \nu_e, \\ \pi^- &\longrightarrow \pi^0 e^- \bar{\nu}_e. \end{aligned}$$

The final states involve mesons and leptons and are consequently known as semileptonic decays. In addition, pibeta is a transition between two spin zero members of an isotriplet: the pions are spin zero bosons with negative parity and isospin one. Therefore, one expects only the vector current to contribute to the hadronic matrix element. The axial vector contribution must vanish as explained in chapter one.

4.1.1 Kinematics

Consider the beta decay of π^+ and suppose q, q', p and k are the 4-momenta of the π^+, π^0, e^+ and ν_e respectively. The relations below follow from momentum conservation:

$$\begin{array}{rclcl} s_1 & = & (q'+p)^2 & = & (q-k)^2, \\ s_2 & = & (p+k)^2 & = & (q-q')^2, \\ s_3 & = & (q'+k)^2 & = & (q-p)^2, \end{array} \tag{4.1}$$

with

$$s_1 + s_2 + s_3 = s + m_{\pi^0}^2 + m_e^2 + m_{\nu_e}^2, \tag{4.2}$$

where

$$s = m_{\pi^+}^2. \tag{4.3}$$

The expressions for the energies and momenta of the final state particles are obtained by considering the 2-body processes below:

$$\begin{array}{rcl} \pi^+ & \longrightarrow & \pi^0 + (e^+ + \nu_e), \\ \pi^+ & \longrightarrow & e^+ + (\nu_e + \pi^0), \\ \pi^+ & \longrightarrow & \nu_e + (\pi^0 + e^+), \end{array}$$

with final state masses $(m_{\pi^0}, \sqrt{s_2})$, $(m_e, \sqrt{s_3})$ and $(m_\nu, \sqrt{s_1})$ respectively [Byc-73]. The explicit calculations *in the rest frame of the decaying* π^+ reveal:

$$E_{\pi^0} = \frac{s + m_{\pi^0}^2 - s_2}{2\sqrt{s}}, \tag{4.4}$$

$$E_e = \frac{s + m_e^2 - s_3}{2\sqrt{s}}, \tag{4.5}$$

and

$$E_{\nu_e} = \frac{s + m_{\nu_e}^2 - s_1}{2\sqrt{s}}. \tag{4.6}$$

The momenta follow from the energy-momentum relation

$$E^2 = m^2 + |\boldsymbol{p}|^2. \tag{4.7}$$

The kinematic constraints on the final state particle energies are derived as follow: from equation (4.1), s_1 reaches a minimum when

$$q' \cdot p = m_{\pi^0} m_e. \tag{4.8}$$

To arrive at the relation (4.8), one writes

$$q' \cdot p = E_{\pi^0} E_e - |\boldsymbol{q}'|\boldsymbol{p}| \cos(\theta), \tag{4.9}$$

where θ is the angle between the 3-momenta. Equation (4.9) goes through a minimum at $\cos(\theta) = 1$. This means that the 3-momenta of π^0 and e^+ are collinear. Suppose that the minimum is some value a to be specified. One gets:

$$a = E_{\pi^0} E_e - |\boldsymbol{q}'||\boldsymbol{p}| \tag{4.10}$$

which leads immediately to:

$$2a = m_{\pi^0} m_e \left(\frac{V_{\pi^0}}{V_e} + \frac{V_e}{V_{\pi^0}} \right), \tag{4.11}$$

where V_{π^0} and V_e are the magnitudes of the velocities of the neutral pion and the electron respectively. Setting

$$V_{\pi^0} = \alpha V_e, \tag{4.12}$$

the relation (4.11) becomes

$$2a = m_{\pi^0} m_e \left(\frac{1+\alpha^2}{\alpha} \right). \tag{4.13}$$

Taking the derivative of equation (4.13), the minimum is reached at $\alpha = 1$ where $a = m_{\pi^0} m_e$: (4.8) is proven and in addition, the neutral pion and the positron have the same velocity as can be seen from (4.12). From (4.1), s_1 reaches a maximum when the neutrino is born at rest. It is straightforward to establish the kinematic constraints on s_2 and s_3. Gathering all the information together:

$$\begin{array}{ccccc} (m_{\pi^0} + m_e)^2 & \leq & s_1 & \leq & (\sqrt{s} - m_{\nu_e})^2, \\ (m_e + m_{\nu_e})^2 & \leq & s_2 & \leq & (\sqrt{s} - m_{\pi^0})^2, \\ (m_{\pi^0} + m_{\nu_e})^2 & \leq & s_3 & \leq & (\sqrt{s} - m_e)^2. \end{array} \tag{4.14}$$

The above relations together with equations (4.4, 4.5 and 4.6) give the allowed energies of the neutral pion, the positron and the neutrino as:

$$\frac{s + m_{\pi^0}^2 - (\sqrt{s} - m_{\pi^0})^2}{2\sqrt{s}} \leq E_{\pi^0} \leq \frac{s + m_{\pi^0}^2 - (m_e + m_{\nu_e})^2}{2\sqrt{s}}, \tag{4.15}$$

$$\frac{s + m_e^2 - (\sqrt{s} - m_e)^2}{2\sqrt{s}} \leq E_e \leq \frac{s + m_e^2 - (m_{\pi^0} + m_{\nu_e})^2}{2\sqrt{s}}, \tag{4.16}$$

and

$$\frac{s+m_{\nu_e}^2-(\sqrt{s}-m_{\nu_e})^2}{2\sqrt{s}} \leq E_{\nu_e} \leq \frac{s+m_{\nu_e}^2-(m_{\pi^0}+m_e)^2}{2\sqrt{s}}. \qquad (4.17)$$

Neglecting the neutrino mass, the explicit calculations show:

$$\begin{array}{rcccr} 134.973 & \leq & E_{\pi^0}\,(\mathrm{MeV}) & \leq & 135.048, \\ 0.511 & \leq & E_e\,(\mathrm{MeV}) & \leq & 4.519, \\ 0.000 & \leq & E_{\nu_e}\,(\mathrm{MeV}) & \leq & 4.023. \end{array} \qquad (4.18)$$

The maximum kinetic energy of the π^0 is about 75 KeV. Because of this recoil energy, the momenta of two gamma rays which originate from the decay of π^0 are not necessarily collinear. Their opening angle can be computed as follows:

- In a frame where the π^0 is at rest, the two gammas have opposite momenta and same energy

$$E_\gamma = \frac{m_{\pi^0}}{2}. \qquad (4.19)$$

- In the rest frame of the decaying π^+:

$$\beta = \frac{|\boldsymbol{q}'|}{E_{\pi^0}}, \qquad (4.20)$$

$$\gamma = \frac{1}{\sqrt{1-\beta^2}}. \qquad (4.21)$$

- The Lorentz transform from the rest frame of π^0 to a frame where the momentum $\boldsymbol{q}'$ of the neutral pion lies along the z-axis gives the 4-momentum of one of the gamma rays (γ_1) as:

$$p'_{x1} = \frac{m_{\pi^0}}{2}\sin(\theta_c)\cos(\phi_c), \qquad (4.22)$$

$$p'_{y1} = \frac{m_{\pi^0}}{2}\sin(\theta_c)\sin(\phi_c), \qquad (4.23)$$

$$p'_{z1} = \frac{m_{\pi^0}}{2}\gamma(\beta+\cos(\theta_c)), \qquad (4.24)$$

$$E'_1 = \frac{m_{\pi^0}}{2}\gamma(1+\beta\cos(\theta_c)). \qquad (4.25)$$

  θ_c and ϕ_c are the polar angles of the gamma in the rest frame of π^0 where the momenta of the gammas are isotropic with θ_c and ϕ_c satisfying the conditions:

$$0^\circ \leq \theta_c \leq 180^\circ, \qquad (4.26)$$

$$0^\circ \leq \phi_c \leq 360^\circ. \qquad (4.27)$$

- To get the 4-momentum $(E_1, \boldsymbol{p_1})$ of the gamma in the rest frame of π^+, one performs the rotation (θ_0, ϕ_0) as follows, with θ_0 and ϕ_0 being the polar angles of the momentum $\boldsymbol{q'}$ of π^0 in the rest frame of π^+:

$$\begin{aligned} p_{x1} &= p'_{x1}\cos(\theta_0)\cos(\phi_0) - p'_{y1}\sin(\phi_0) + p'_{z1}\sin(\theta_0)\cos(\phi_0), && (4.28)\\ p_{y1} &= p'_{x1}\cos(\theta_0)\sin(\phi_0) + p'_{y1}\cos(\phi_0) + p'_{z1}\sin(\theta_0)\sin(\phi_0), && (4.29)\\ P_{z1} &= -p'_{x1}\sin(\theta_0) + p'_{z1}\cos(\theta_0), && (4.30)\\ E_1 &= E'_1. && (4.31) \end{aligned}$$

- The energy and momentum $(E_2, \boldsymbol{p_2})$ of the second gamma follow from space reflection:

$$\begin{aligned} \theta_c &\longrightarrow 180^\circ - \theta_c, \\ \phi_c &\longrightarrow 180^\circ + \phi_c. \end{aligned}$$

- Finally, the opening angle of the two gammas is computed as:

$$\cos(\boldsymbol{p_1}, \boldsymbol{p_2}) = \frac{\boldsymbol{p_1} \cdot \boldsymbol{p_2}}{|\boldsymbol{p_1}||\boldsymbol{p_2}|}. \tag{4.32}$$

The figure 4.1 shows the distribution of the opening angle of the two gamma rays, and the energy spectrum of one of the photons is displed in figure 4.2.

4.1.2 Pion Beta Decay Rate

The differential decay width is:

$$d\Gamma = \frac{|\mathcal{M}|^2}{2m_{\pi^+}(2\pi)^9} \frac{d^3q'}{2E_{\pi^0}} \frac{d^3p}{2E_e} \frac{d^3k}{2E_{\nu_e}} (2\pi)^4 \delta^4(q - q' - p - k), \tag{4.33}$$

where the matrix element is

$$\mathcal{M} = \frac{G}{\sqrt{2}} V_{ud} \bar{u}_\nu(k) \gamma^\mu \left(1 - \gamma^5\right) u_e(p) < \pi^0(q')|V_\mu|\pi^+(q) > . \tag{4.34}$$

The hadronic matrix element $< \pi^0(q')|V_\mu|\pi^+(q) >$ can only be a vector as explained in chapter one. With the similar method used to write down equation 1.42, the hadronic matrix element is:

$$< \pi^0(q')|V_\mu|\pi^+(q) >= (q + q')_\mu f_1(Q^2) + (q - q')_\mu f_2(Q^2), \tag{4.35}$$

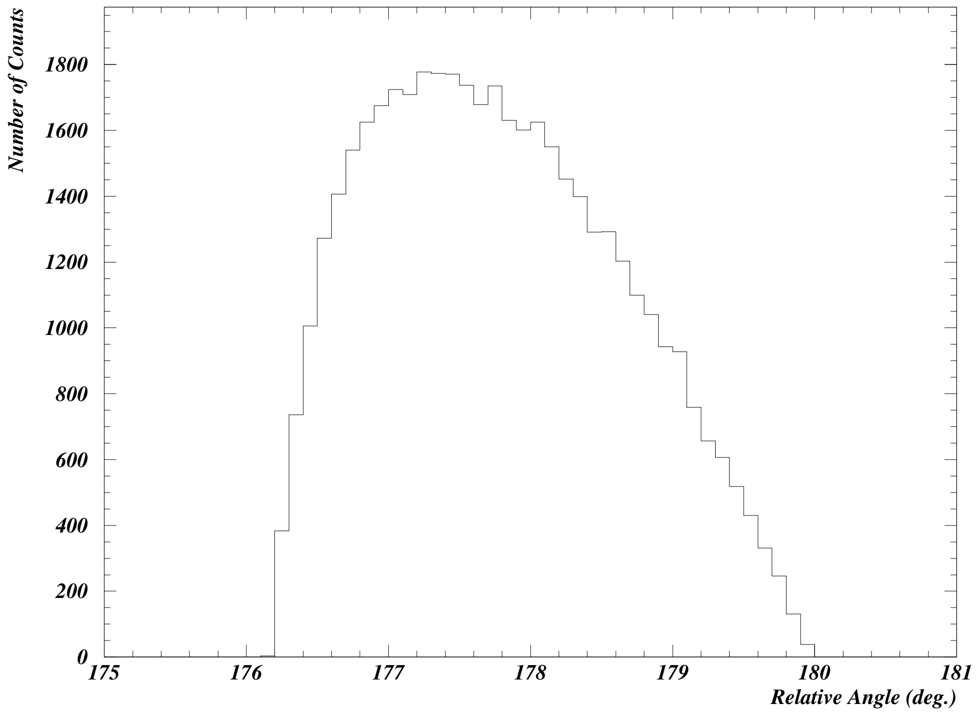

Figure 4.1: The opening angle between the two gamma rays from the π^0 decays. The directions of the gamma rays deviate from collinearity by at most 3.8° due to the recoil energy of the π^0.

with

$$Q = (q - q'). \tag{4.36}$$

Equation (4.35) follows from the fact that since there is no spin, $(q+q')_\nu$ and $(q-q')_\nu$ are the only vectors available to construct the matrix element. The CVC hypothesis requires that

$$Q^\mu < \pi^0(q')|V_\mu|\pi^+(q) >= 0 \tag{4.37}$$

which leads to

$$(m_{\pi^+}^2 - m_{\pi^0}^2)f_1 - Q^2 f_2 = 0. \tag{4.38}$$

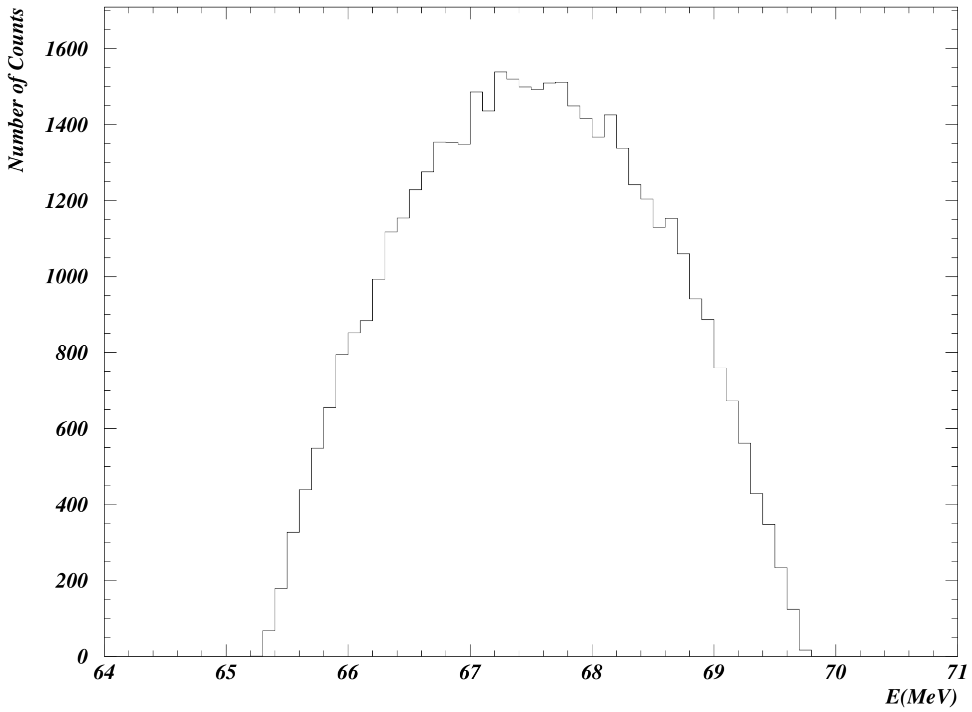

Figure 4.2: The energy spectrum of one of the gamma rays originating from the decay of the π^0. The spread of this energy reflects the spread in the recoil energy of the π^0.

In the exact isospin symmetry, $m_{\pi+} = m_{\pi^0}$ hence $f_2 \equiv 0$. The square matrix element is:

$$|\mathcal{M}|^2 = \frac{G^2 V_{ud}^2}{2} \sum_{\text{spin}} \left| \bar{u}_\nu \gamma^\mu \left(1 - \gamma^5\right) u_e \left\{a_\mu f_1 + Q_\mu f_2\right\}\right|^2 . \tag{4.39}$$

where

$$a = q + q'. \tag{4.40}$$

Using some trace theorems [Hal-84], it is a straightforward exercice to show that

$$\begin{aligned} |\mathcal{M}|^2 &= 4G^2 V_{ud}^2 \left\{ f_1^2 \left(2(a \cdot p)(a \cdot k) - a^2 (k \cdot p)\right) \right. \\ &\quad \left. + f_2^2 m_e^2 (k \cdot p) + 2 f_1 f_2 m_e^2 (a \cdot k)\right\} . \end{aligned} \tag{4.41}$$

In equation (4.41), the terms proportional to $m_e^2 f_2$ are negligible compare to the rest due to the electron mass. In addition, since the range of Q^2 is small $Q^2 \leq (m_{\pi^+} - m_{\pi^0})^2$, $f_1(Q^2)$ is replaced by its value at $Q^2 = 0$. However, $f_1(0)$ is fixed by the CVC hypothesis:

$$f_1(0) = \sqrt{2} \tag{4.42}$$

as was demonstrated in chapter one. With all these simplifications, the matrix element becomes:

$$|\mathcal{M}|^2 = 4G^2 V_{ud}^2 \left(2(a \cdot p)(a \cdot k) - a^2(k \cdot p)\right) f_1^2(0). \tag{4.43}$$

At this point, the decay width is written as:

$$\Gamma = C \int g(Q^2) \frac{d^3 q'}{2E_{\pi^0}}, \tag{4.44}$$

where

$$C = \frac{4}{(2\pi)^5} \frac{G^2 V_{ud}^2}{m_{\pi^+}} \tag{4.45}$$

and

$$g(Q^2) = \int\int \frac{d^3 p}{2E_e} \frac{d^3 k}{2E_{\nu_e}} \delta^4(Q - p - k) \left(2(a \cdot p)(a \cdot k) - a^2(k \cdot p)\right). \tag{4.46}$$

The above equation can be written as:

$$g(Q^2) = \left[\int\int \frac{d^3 p}{2E_e} \frac{d^3 k}{2E_{\nu_e}} \delta^4(Q - p - k) \left(p^\mu k^\nu + p^\nu k^\mu - (k \cdot p) g^{\mu\nu}\right)\right] a_\mu a_\nu. \tag{4.47}$$

One may write $g(Q^2)$ more elegantly as:

$$g(Q^2) = \left\{A(Q^2) Q^\mu Q^\nu - Q^2 B(Q^2) g^{\mu\nu}\right\} a_\mu a_\nu. \tag{4.48}$$

$A(Q^2)$ and $B(Q^2)$ need to be isolated and calculated. To that end, one contracts (4.48) with $Q_\mu Q_\nu$ and with $g_{\mu\nu}$. The results are two equations which are quickly solve to get:

$$A(Q^2) = \frac{2}{3Q^4} \int\int \frac{d^3 p}{2E_e} \frac{d^3 k}{2E_{\nu_e}} \delta^4(Q - p - k) \left[4(Q \cdot p)(Q \cdot k) - Q^2(p \cdot k)\right] \tag{4.49}$$

and

$$B(Q^2) = \frac{1}{3Q^4} \int\int \frac{d^3 p}{2E_e} \frac{d^3 k}{2E_{\nu_e}} \delta^4(Q - p - k) \left[2(Q \cdot p)(Q \cdot k) + Q^2(p \cdot k)\right] \tag{4.50}$$

After the isolation of $A(Q^2)$ and $B(Q^2)$, the integrations can be performed with the aid of the following properties of the δ-function:

$$\delta(ax) = \frac{1}{a}\delta(x), \tag{4.51}$$

and

$$\int \frac{d^3k}{2E_\nu} = \int d^4k\theta(E_\nu)\delta(k^2), \tag{4.52}$$

with

$$k^2 = 0. \tag{4.53}$$

$\theta(E)$ is the step function. The integral (4.49) reduces to:

$$\begin{aligned} A(Q^2) &= \frac{2}{3Q^4}\int \frac{d^3p}{2E_e}\theta(E_\nu)\delta((Q-p)^2)\times \\ &\quad \left[4(Q\cdot p)(Q\cdot Q-p) - Q^2(p\cdot Q-p)\right], \end{aligned} \tag{4.54}$$

where k has been replaced by $Q-p$. One gets:

$$(Q-p)^2 = Q^2 + m_e^2 - 2Q\cdot p, \tag{4.55}$$

$$Q\cdot p = E_Q E_e - |\boldsymbol{Q}||\boldsymbol{p}|\cos(\boldsymbol{Q},\boldsymbol{p}), \tag{4.56}$$

and

$$d^3p = -(2\pi)E_e|\boldsymbol{p}|dE_e d\cos(\boldsymbol{Q},\boldsymbol{p}). \tag{4.57}$$

Putting all this together,

$$\begin{aligned} A(Q^2) &= \frac{\pi}{3Q^4}\int \frac{dE_e}{|\boldsymbol{Q}|}d(Q\cdot p)\delta(\frac{Q^2+m_e^2}{2} - Q\cdot p)\times \\ &\quad \left[4(Q\cdot p(Q^2 - Q\cdot p) - Q^2(Q\cdot p - m_e^2)\right]. \end{aligned} \tag{4.58}$$

Integrating over the δ-function:

$$A(Q^2) = \frac{\pi}{3Q^4}\left(\frac{Q^2-m_e^2}{2}\right)\left(1+\frac{2m_e^2}{Q^2}\right)\frac{Q^2}{|\boldsymbol{Q}|}\int_{E_1}^{E_2} dE_e. \tag{4.59}$$

To get the limits E_1 and E_2, one realizes that after the δ-function integration, (4.56) becomes:

$$\frac{Q^2+m_e^2}{2} = E_Q E_e - |\boldsymbol{Q}||\boldsymbol{p}|\cos(\boldsymbol{Q},\boldsymbol{p}). \tag{4.60}$$

Since

$$|\cos(\boldsymbol{Q},\boldsymbol{p})| \leq 1, \tag{4.61}$$

equation (4.60) sets the range of integration over E_e which is determined as follows: solve (4.60) for $\cos(\boldsymbol{Q},\boldsymbol{p})$ and use the condition (4.61) to get:

$$E_e^2 Q^2 - E_e E_Q (m_e^2 + Q^2) + \frac{1}{4}(m_e^2 + Q^2)^2 + m_e^2 |\boldsymbol{Q}|^2 \leq 0. \tag{4.62}$$

One arrives at the discriminant

$$D = (Q^2 - m_e^2)|\boldsymbol{Q}|^2 \tag{4.63}$$

and finds the roots

$$E = \frac{E_Q(m_e^2 + Q^2) \pm |\boldsymbol{Q}|\sqrt{Q^2 - m_e^2}}{2Q^2} \tag{4.64}$$

from which the desired range of E_e is obtained:

$$\begin{array}{rl} \frac{E_Q(Q^2+m_e^2)-\sqrt{D}}{2Q^2} & \leq E_e, \\ \frac{E_Q(Q^2+m_e^2)-\sqrt{D}}{2Q^2} & \geq E_e. \end{array} \tag{4.65}$$

Finally, the integration (4.59) is carried out to get $A(Q^2)$:

$$A(Q^2) = \frac{\pi}{6}\frac{(Q^2 + m_e^2)^2}{Q^4}\left(1 + \frac{2m_e^2}{Q^2}\right). \tag{4.66}$$

With similar approach,

$$B(Q^2) = \frac{\pi}{6}\frac{(Q^2 + m_e^2)^2}{Q^4}\left(1 + \frac{m_e^2}{2Q^2}\right). \tag{4.67}$$

The decay width can now be written as:

$$\Gamma = C \int |\boldsymbol{q'}|^2 \frac{d|\boldsymbol{q'}|}{2E_{\pi^0}} \left(A(Q^2)Q^\mu Q^\nu - Q^2 B(Q^2) g^{\mu\nu}\right) a_\mu a_\nu. \tag{4.68}$$

From $q - q' = Q$,

$$E_{\pi^0} = \frac{m_{\pi^+}^2 + m_{\pi^0}^2 - Q^2}{2m_{\pi^+}} \tag{4.69}$$

and from the energy-momentum relation

$$|\boldsymbol{q'}| = \frac{\sqrt{m_{\pi^+} m_{\pi^0}}}{m_{\pi^+}} \sqrt{(\Delta^2 - Q^2)\left(1 + \frac{\Delta^2 - Q^2}{4m_{\pi^+} m_{\pi^0}}\right)}. \tag{4.70}$$

where Δ is the pion mass difference:

$$\Delta = m_{\pi^+} - m_{\pi^0}. \tag{4.71}$$

In addition,

$$\frac{|\boldsymbol{q}'|^2}{E_{\pi^0}} d|\boldsymbol{q}'| \;=\; |\boldsymbol{q}'| dE_{\pi^0} \;=\; -\frac{|\boldsymbol{q}'|}{2m_{\pi^+}} d(Q^2). \tag{4.72}$$

Furthermore,

$$\begin{aligned} a^2 &= 2(m_{\pi^+}^2 + m_{\pi^0}^2) - Q^2, && (4.73)\\ a \cdot Q &= \Delta(m_{\pi^+} + m_{\pi^0}), && (4.74) \end{aligned}$$

and

$$\left(A(Q^2)Q^\mu Q^\nu - Q^2 B(Q^2) g^{\mu\nu}\right) a_\mu a_\nu = A(Q^2)(a\cdot Q)^2 - B(Q^2)Q^2 a^2. \tag{4.75}$$

The decay width now appears as:

$$\begin{aligned} \Gamma &= 2\pi C \Delta^5 \frac{(m_{\pi^+} + m_{\pi^0})^2 \sqrt{m_{\pi^+} m_{\pi^0}}}{2m_{\pi^+}^2} \\ &\quad \int \sqrt{1 - \frac{Q^2}{\Delta^2}} \left(A(Q^2) - B(Q^2)\frac{Q^2}{\Delta^2}\right) \frac{d(Q^2)}{\Delta^2} && (4.76) \end{aligned}$$

where small terms of the order $\Delta^2/m_{\pi^+}^2$ have been neglected. It is useful to introduce a variable z and a parameter ϵ such that:

$$z = \frac{Q^2}{\Delta^2}, \tag{4.77}$$

and

$$\epsilon = \frac{m_e^2}{\Delta^2}. \tag{4.78}$$

Finally, the decay width is obtained as:

$$\Gamma = \frac{G^2 V_{ud}^2 \Delta^5}{30\pi^3} \frac{(m_{\pi^+} + m_{\pi^0})^2 \sqrt{m_{\pi^+} m_{\pi^0}}}{4m_{\pi^+}^3} \mathcal{K}(\epsilon), \tag{4.79}$$

where

$$\mathcal{K}(\epsilon) = \frac{2}{5}\int_\epsilon^1 \sqrt{1-z}\left(\frac{z-\epsilon}{z}\right)^2 \left(1 - z - \frac{\epsilon}{2} + 2\frac{\epsilon}{z}\right). \tag{4.80}$$

It is straightforward to show that with $m_{\pi^0} = m_{\pi^+} - \Delta$,

$$\frac{(m_{\pi^+} + m_{\pi^0})^2 \sqrt{m_{\pi^+} m_{\pi^0}}}{4m_{\pi^+}^3} \simeq 1 - \frac{3\Delta}{2m_{\pi^+}}. \tag{4.81}$$

The integration (4.79) can also be carried out:

$$\mathcal{K}(\epsilon) = \sqrt{1-\epsilon}\left(1 - \frac{9}{2}\epsilon + 4\epsilon^2\right) + \frac{15}{2}\ln\left(\frac{1+\sqrt{1-\epsilon}}{\sqrt{\epsilon}}\right). \tag{4.82}$$

Equation (4.79) together with the main decay mode of the π^+, that is $\pi^+ \longrightarrow \mu^+\nu$, gives the branching ratio of the pion beta process: $\sim 10^{-8}$. The other decay channels of π^+ are listed below with their probability of occurrence in parentheses:

$$\begin{array}{ccll} \pi^+ & \longrightarrow & \mu^+\nu & (1.0) \\ \pi^+ & \longrightarrow & e^+\nu & (\sim 1.2\times 10^{-4}) \\ \pi^+ & \longrightarrow & \mu^+\nu\gamma & (\sim 1.2\times 10^{-4}) \\ \pi^+ & \longrightarrow & e^+\nu\gamma & (\sim 1.6\times 10^{-7}). \end{array} \tag{4.83}$$

4.2 $\pi^+ \longrightarrow \mu^+\nu_\mu$ Decay

The energy of the muon in this 2-body decay is given by equation (4.4) with $s_2 = m_\nu^2$. Neglecting the neutrino mass, the muon kinetic energy in the rest frame of the pion is:

$$KE_\mu = 4.118\,\mathrm{MeV} \tag{4.84}$$

The matrix element of the decay is:

$$\mathcal{M} = \frac{G}{\sqrt{2}} V_{ud}\,\bar{u}_\nu(k)\gamma^\mu\left(1-\gamma^5\right)u_\mu(p) < 0|A_\mu|\pi^+(q) > . \tag{4.85}$$

In this case, the vector contribution to the hadronic matrix element must vanish because of parity [Geo-84]. The axial vector contribution is parametrized as:

$$< 0|A_\mu|\pi^+(q) >= f_\pi\left(p_\mu + k_\mu\right). \tag{4.86}$$

One notes in passing that if the pion were massless, the axial current would be conserved since:

$$q^\mu A_\mu = f_\pi m_{\pi^+}^2 \tag{4.87}$$

in which case the pions could be identified as the Goldstone bosons associated with the spontaneous breaking of chiral symmetry. Using Dirac equation and zero mass for the neutrino, equation (4.85) becomes:

$$\mathcal{M} = \frac{G}{\sqrt{2}} V_{ud} m_\mu \bar{u}_\nu(k) \left(1 - \gamma^5\right) u_\mu(p). \tag{4.88}$$

Summing over final spin states and using some trace theorems:

$$|\mathcal{M}|^2 = 4G^2 V_{ud}^2 f_\pi^2 m_\mu^2 p \cdot k. \tag{4.89}$$

The above expression together with the phase space factor gives, after integrating over fermion energies, the decay rate as:

$$\Gamma\left(\pi^+ \to \mu^+\nu_\mu\right) = \frac{G^2 V_{ud}^2 f_\pi^2}{8\pi} m_{\pi^+} m_\mu^2 \left(1 - \frac{m_\mu^2}{m_{\pi^+}^2}\right)^2. \tag{4.90}$$

In the case of a massless muon (relativistic limit for instance), this decay would be forbidden: in the relativistic limit, leptons are left-handed and antileptons are right-handed due to the V−A structure of the interaction and in analogy to the case of the neutrino discussed in chapter one. By considering the conservation of helicity and angular momentum, this decay is forbidden.

4.2.1 Muon Decay: $\mu \to e\nu_e\bar{\nu}_\mu$

The kinematic of this decay follows from that of the pion beta process discussed in above:

$$\begin{array}{rcccl} 0.511 & \leq & E_e\,(\mathrm{MeV}) & \leq & 52.830, \\ 0.000 & \leq & E_{\nu_e}\,(\mathrm{MeV}) & \leq & 52.828, \\ 0.000 & \leq & E_{\bar{\nu}_\mu}\,(\mathrm{MeV}) & \leq & 52.828. \end{array} \tag{4.91}$$

The decay rate can also be calculated using the same approach as in the case of pibeta with the following modifications:

- This is a pure leptonic decay which involves no mixing: The coupling constant is simply G instead of GV_{ud}.

- The matrix element is

$$\mathcal{M} = \frac{G}{\sqrt{2}} \bar{u}_{\nu_\mu} \gamma^\alpha \left(1 - \gamma^5\right) u_\mu \bar{u}_e \gamma_\alpha \left(1 - \gamma^5\right) u_\nu \tag{4.92}$$

- The positron energy is assumed to be much greater than its rest mass.

With the above adjustments, the energy spectrum of the positron is calculated to be:

$$\Gamma(\epsilon)d\epsilon = \frac{G^2 m_\mu^2}{192\pi^3}(3-2\epsilon)\,\epsilon^2 d\epsilon, \tag{4.93}$$

where

$$\epsilon = \frac{2E_e}{m_\mu}. \tag{4.94}$$

However, for the most general form of the four-fermion interaction, the positron spectrum has been shown to be [Sch-83]:

$$\Gamma(\epsilon)d\epsilon = \frac{G^2 m_\mu^2}{16\pi^3}\left\{1-\epsilon-\frac{2}{9}\rho(3-4\epsilon)\right\}\epsilon^2 d\epsilon. \tag{4.95}$$

The energy spectrum of the positron is displayed in figure (4.3). In the event of

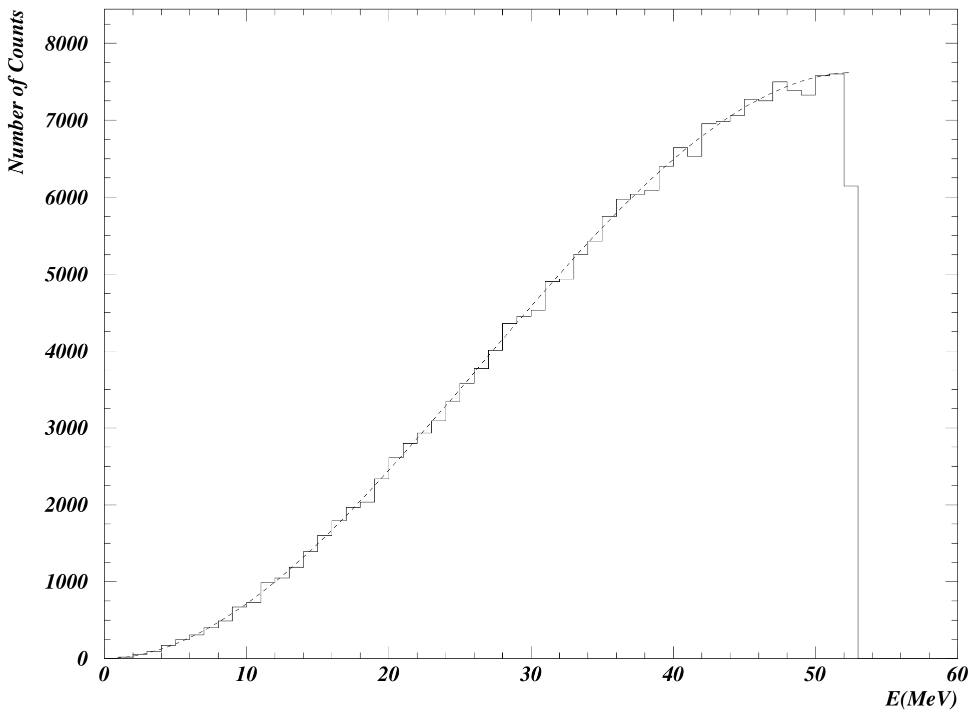

Figure 4.3: The energy spectrum of positrons from muon decays. This distribution is known as Michel spectrum and constitutes the major background in the study of pion beta decay in the stopped pion mode. The theoretical curve (dashed lines) is superimposed on the Monte Carlo generated distribution.

exact V-A structure of the weak charged current, the spectrum (4.95) reduces to (4.93) giving the Michel parameter $\rho = 0.75$.

The other decay modes of the muon are listed below:

$$\begin{array}{lcll} \mu^+ & \longrightarrow & e^+\bar{\nu}_\mu\nu_e\gamma & (\sim 0.014) \\ \mu^+ & \longrightarrow & e^+\bar{\nu}_\mu\nu_e e^+e^- & (\sim 3\times 10^{-5}). \end{array} \tag{4.96}$$

4.3 $\pi^+ \longrightarrow e^+\nu_e$ Decay

By making the appropriate change in equation (4.4), the kinetic energy of the positron is calculated as

$$KE_e = 69.273\,\mathrm{MeV}. \tag{4.97}$$

The decay rate follows from the $e\mu$ universality principle by substituting m_e for m_μ in equation (4.90).

Chapter 5

Overview of the Apparatus

Thus far, the foundations for a firm understanding of the motivation for the pion beta decay experiment have been laid down. In addition, a description of the Ring accelerator at the Paul Scherrer Institute in relation to the experiment has been presented. The beam studies that have been done to date have also been discussed, particularly the beam particle rates, contaminations, profiles and spot size. After the explanation of the motivation and the description of the production of the pions, a thorough explanation of the decay channels of the pion with the associated kinematical information were supplied since these affect the design of the apparatus which is introduced in this chapter. Here, a general overview of the experiment is given and the description of the salient components of the apparatus is presented.

The pion beta decay experiment is carried out in a stopped-pion mode: the $\pi E1$ channel of the Paul Scherrer Institute is set to transport 116 MeV/c particles with a momentum spread of about 2%. The beam is optimized for low positron and muon contaminations relative to the pion rate as discussed in chapter 3. After passing through a degrading material (active degrader), the pions come to rest within a plastic scintillator fiber hodoscope (the active target) where they decay with a mean life time of 26 ns. The active degrader is designed such that the beam pions stop within the central region of the active target. In addition, the active degrader enables the elimination of the beam muons and positrons by time of flight and pulse height information.

The decay channels of the pion are discussed in chapter 4. Since pion beta decay is the process of interest, the other decay modes constitute the background which must be suppressed. Among the decay products of the pion, one finds positrons, gamma rays, neutrinos and muons which, in turn, decay into the lighter particles with a mean life time of $2.2\,\mu$s. The decay muons with about 4.2 MeV, do not have enough energy to exit the fibers; they stop within the target where they decay mostly into Michel positrons some of which have sufficient energy to escape the target. The positrons from $\pi^+ \rightarrow e^+\nu_e$ with about 69 MeV are also capable of exiting the target. The energy lost by the positrons depends on where in the target they originate from and the amount of material traversed. A small fraction of the positrons (from $\pi^+ \rightarrow e^+\nu_e$ or Michel decays) annihilates with atomic electrons in the target material and the resulting gamma rays can exit the target.

The gamma rays on the other hand, pass through the plastic scintillators without any appreciable loss of energy. To detect them, a calorimeter is designed and fabricated from pure Cesium Iodide (CsI), one of the inorganic crystals with great stopping power due to their high density ($4.53\,\mathrm{g/cm^3}$ for CsI) and atomic number. These inorganic crystals also have the highest light output with better energy resolution which make them suitable for the detection of, not only gamma rays, but high energy electrons and positrons as well. Depending on their energy, the positrons which do reach the calorimeter initiate positron-photon showers via bremsstrahlung or suffer energy loss via ionization. The gamma rays also, depending on their energy, initiate showers via pair production or undergo Compton scattering or photo electric effect.

The experimental apparatus comprises the following main components:

- Beam counters, an active degrader and an active target to stop the pions, to discriminate against the muon and positron contaminations of the beam and to measure the lateral stopping distributions.

- Two multi-wire proportional chambers (MWPC) for charged particle tracking surrounding the active target inside the calorimeter. The MWPC's are capable of determining charged particle coordinates to better than 2 mm and ensuring high degree suppression of random coincidences of Michel events.

- A segmented plastic veto counter surrounding the MWPC's inside the calorimeter. Its purpose is an efficient identification of charged particle induced events.

- A high-resolution highly segmented fast shower calorimeter surrounding the active target in a near-spherical geometry with two openings for beam entry and readout of inner detectors. Its role is the detection of the two gamma rays from π^0 decays and the positron from $\pi^+ \to e^+\nu_e$.

- A thermal house surrounding the calorimeter. Cesium Iodide is slightly hygroscopic. For this reason, the CsI modules which have been delivered thus far are kept in a dried room with climatization. Also, the experimental apparatus will be thermally insulated for the control and the stabilization of the humidity and the temperature. A cooling apparatus is required due to the energy radiated by the bases of the PMT's. The control of the humidity follows from the hygroscopic property of CsI. Fluctuations in the temperature result in the drifts of the PMT gains and ultimately affect the energy resolution, and changes in the temperature and the humidity may affect the light collection efficiency. In addition, the temperature coefficient of the CsI light output is negative; as a result, the cooler the CsI the higher the light output.

- A lead house around the thermal house to avoid self vetoing (in the cosmic veto counters) of the shower leaking through the back of the calorimeter and to shield the calorimeter from beam related events.

- Veto counters around the entire apparatus to eliminate cosmic ray induced events.

The layout of the experimental apparatus is shown in figure 5.1.

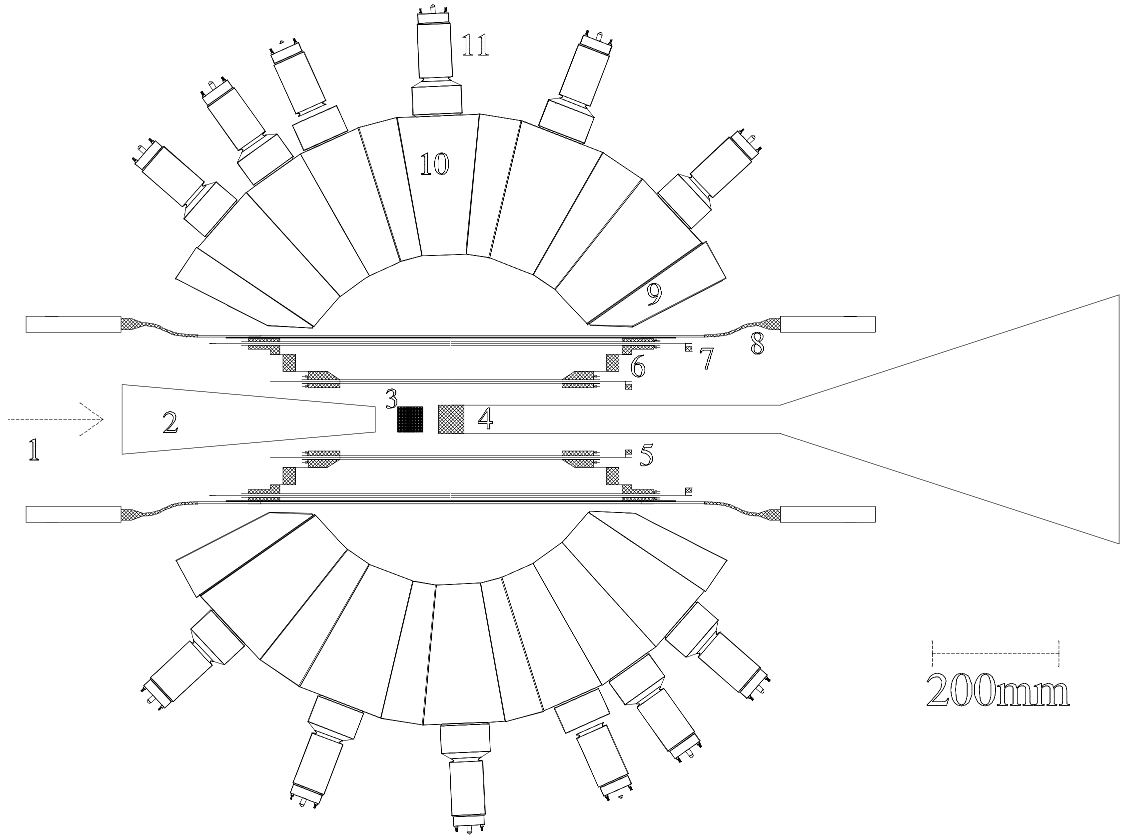

Figure 5.1: A cut view of the apparatus. The pion beam (1) goes through the vacuum pipe (2), traverses the active degrader (3) and stops within the active target (4). The experiment is equipped with two cylindrical MWPC's (5) and (7), a segmented plastic veto detector (8) and a shower calorimeter (10) with shower vetoes (9). Each of the calorimeter modules is viewed by a PMT (11) glued at the back face. The support for the MWPC's is provided by flanges and step-down rings (6). There is a thin (1mm thick) carbon fiber cylinder between the outer MWPC and the plastic veto detector for the support of the latter.

5.1 Active Target

The role of the active target is to monitor the lateral stopping distributions. The active target consists of 69 plastic scintillator fibers surrounded by 8 guard-ring elements of the same material. The entire active target is a cylinder of 4 cm diameter and 5 cm long as shown in figure 5.4. However, each of the 69 fibers has a square cross section of $2.76 \times 2.76\,\mathrm{mm}^2$ and is covered with an acrylic cladding of 0.12 mm thick for optical isolation. The fibers are then glued together with epoxy to make the active target. Each fiber is connected to a one-inch photomultiplier tube via a

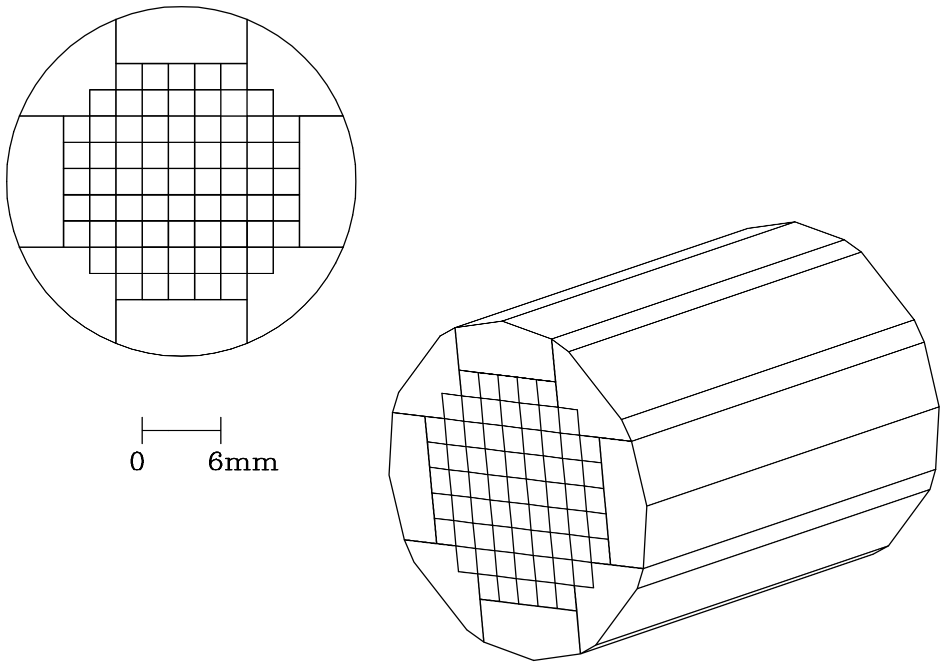

Figure 5.4: The active target used during the test run of 1994 to measure the horizontal and vertical beam profiles. It contains 69 plastic scintillator fibers with 8 guard-ring elements of the same material around them. Each fiber is isolated by an acrylic cladding and they are held together with epoxy.

fiber optic light guide.

The stopping distributions are needed for an accurate Monte Carlo simulation of the experiment and acceptance corrections for pion beta and $\pi^+ \rightarrow e^+\nu_e$ decays.

5.2 Tracking Detectors

The apparatus is equipped with two MWPC's whose importance is dictated by the need for double track resolution and the $\pi^+ \to e^+\nu_e$ trigger. The multiple shower

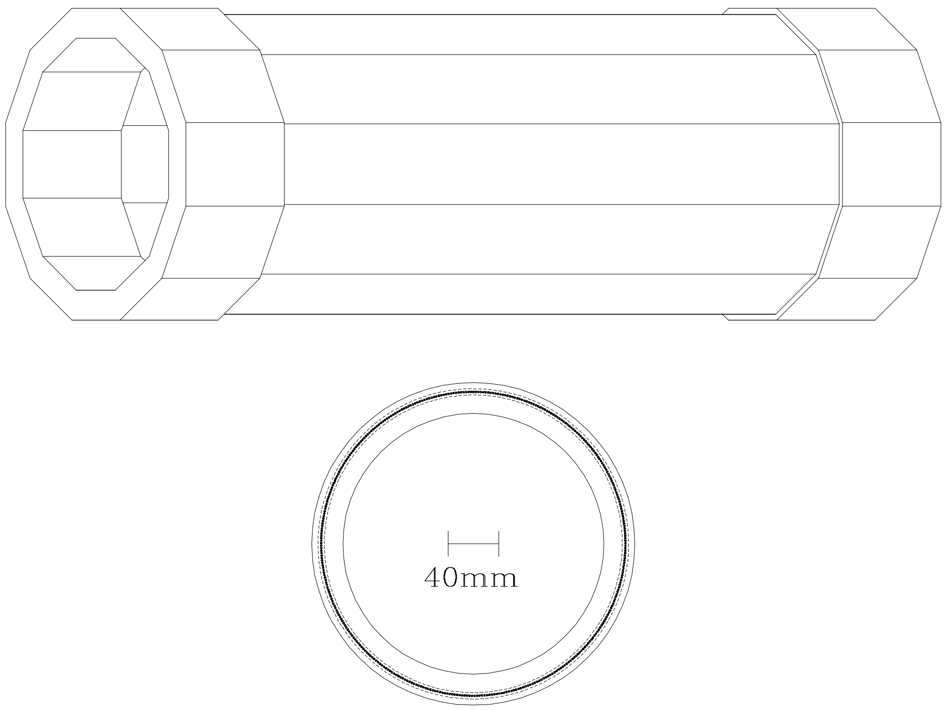

Figure 5.5: Cylindrical multi-wire proportional chamber for the pion beta experiment. Shown here is the outer chamber. The inner chamber is geometrically the same but smaller with fewer anode wires and cathode strips.

resolution of the calorimeter is limited to $\sim 4 \times 10^{-3}$ (0.004 of 4π in solid angle). However, for a high degree suppression of the accidental Michel events, a higher double event resolution is required. Additional suppression factors of the order of 6×10^{-3} from the MWPC's suffice to significantly reduce the Michel background under the $\pi^+ \to e^+\nu_e$ peak in high pion stopping rate: $\sim 5 \times 10^6\,\mathrm{s}^{-1}$. In addition to the double track resolution capability, the MWPC's have low mass — 3×10^{-3} radiation length of CsI[1] — which is necessary to reduce the probability of conversion of pion beta γ's prior to their arrival in the calorimeter and to detect low energy

[1]One radiation length of CsI is $X_o = 1.85\,\mathrm{cm}$

positrons. They are also expected to handle high rates with an efficiency of the order of $1 - 10^{-3}$.

	Inner chamber	Outer Chamber
Active length (mm)	350	540
Inner radius (mm)	45	103
Wire layer radius (mm)	60.15	120.1
Outer radius (mm)	76	127.5
Number of wires	192	385
Anode wire spacing(mm)	1.96	1.96
Strip width (mm)	3	2.4
Inner cathode radius(mm)	57.6	117.6
Outer cathode radius(mm)	62.5	122.6
Number of inner strips	128	192
Number of outer strips	128	192
Gap between strips(mm)	0.4	0.3
Half gas gap (mm)	2.55	2.5
Thickness (X_o)	1.4×10^{-3}	2.0×10^{-3}
Volume(cm^3)	660	2035

Table 5.1: Some parameters of the multi-wire proportional chambers of the pion beta experiment.

The MWPC 's have a cylindrical geometry (as shown in figure 5.5) with one anode wire plane in the longitudinal direction and two cathode strip planes in stereoscopic geometry. The MWPC's were fabricated in Dubna (Russia) and tested at the Paul Scherrer Institute. A cathode strip resolution of 0.2 mm full width half maximum has been measured. The main characteristics of the MWPC's are compiled in table 5.1.

5.3 Plastic Veto Counters

The outer MWPC is surrounded by a thin plastic veto detector (PV). The PV allows an efficient identification of charged particle induced events with good timing resolution. The PV has a cylindrical geometry with outer radius of 135 mm, a thickness of $\sim$ 3 mm and active length of 600 mm. It contains 20 modules with

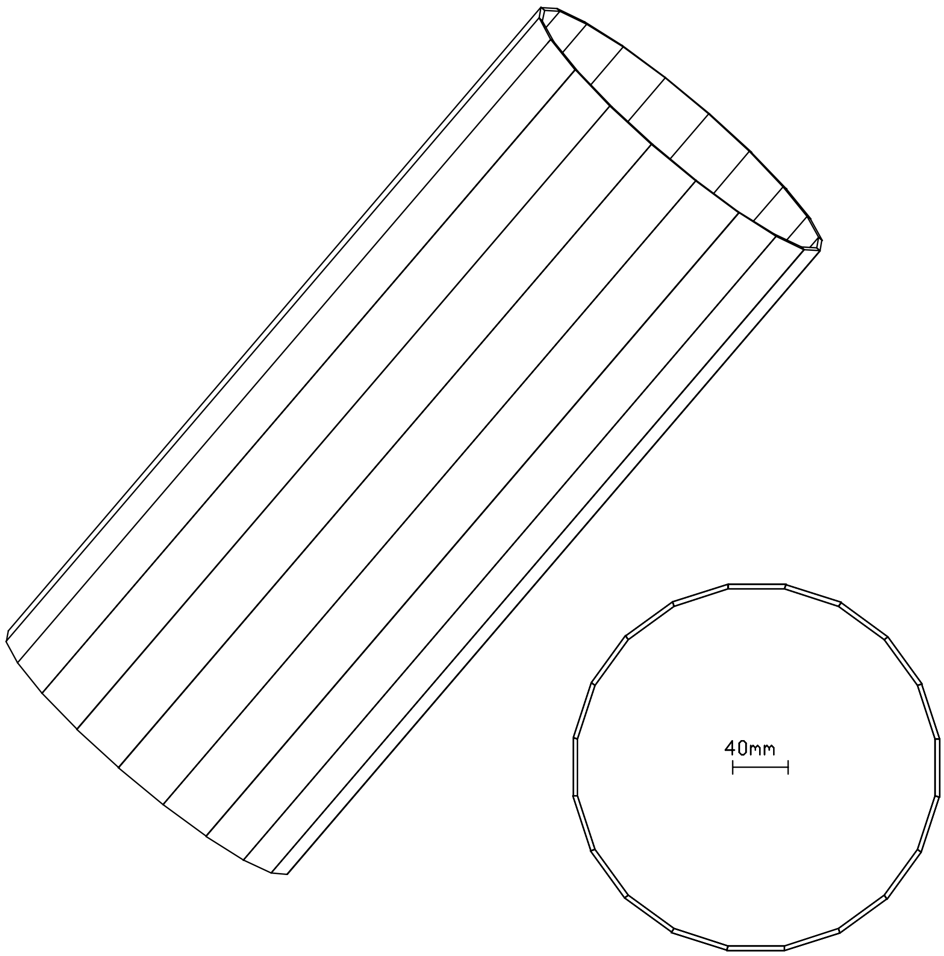

Figure 5.6: The Plastic Veto detector: it contains 20 modules each of which is read longitudinally at both ends. With a thickness of 3.175 mm, it ensures an efficient identification of charged particles.

interleaved edges as displayed in figure 5.6 and its segmentation is consistent with the geometry of the calorimeter and dictated by the stopping rate. Each of its modules is coupled via a light guide at both ends to a photomultiplier tube.

The PV is designed such that it provides a good separation of minimum ionizing particles, i.e. a separation of neutral and charged tracks as shown in figure 5.7. Therefore, for the pion beta processes, the PV allows the rejection of charged particle induced events in the calorimeter while it vetoes out the neutrals for the $\pi^+ \to e^+\nu_e$ processes.

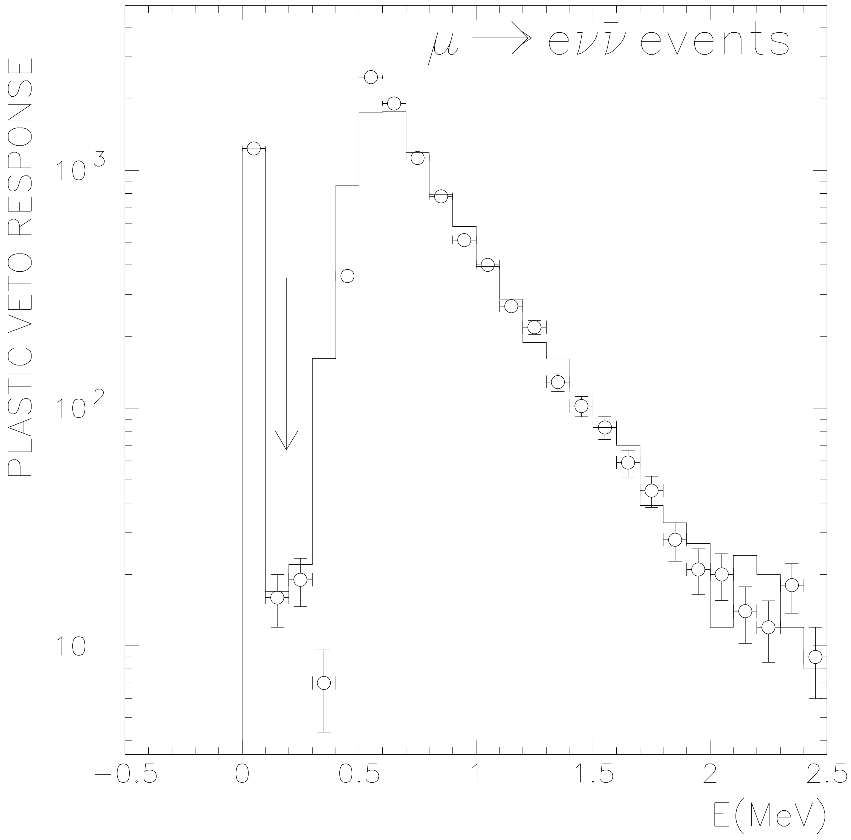

Figure 5.7: Simulation of the response of the Plastic Veto detector to Michel events thrown according to the stopping distribution and originating in the target. The arrow indicates the Minimum Ionizing Particle threshold. The energy deposited is superimposed on the histogram of the light output. Even after accounting for photoelectron statistics and light collection nonuniformity, there is a clear separation between charged and neutral particles as indicated by the arrow.

5.4 Shower Calorimeter

Surrounding the above described detectors is a high resolution shower calorimeter which contains 240 detector modules all of which are made of pure CsI. Its geometry is spherical with two openings for beam entry and readout of inner detectors as displayed in figure 5.8. The solid angle coverage of the calorimeter is about 77% of 4π,

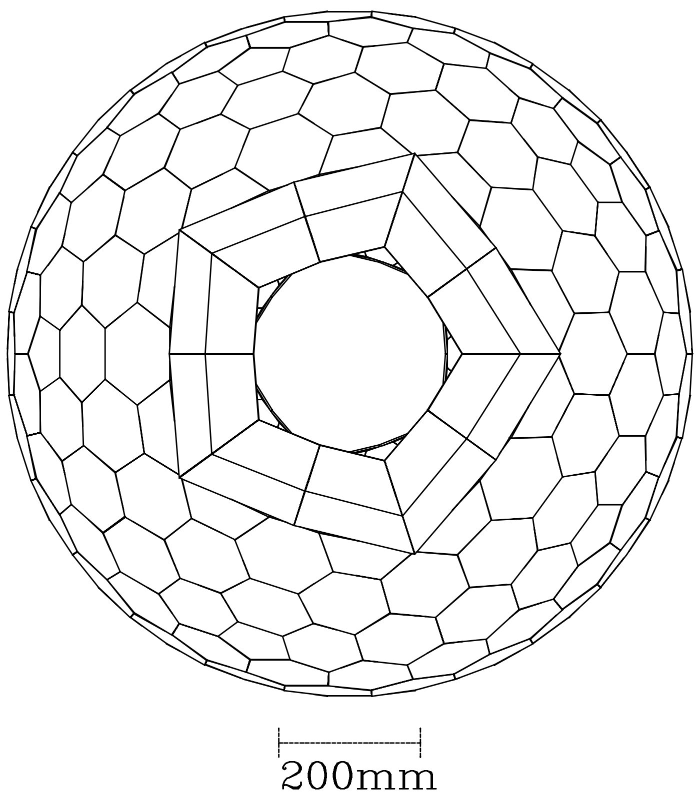

Figure 5.8: The pion beta shower calorimeter and its segmentation as a result of a class II geodesic subdivision of an icosahedron. It contains 240 modules each of which is read with a photomultiplier tube glued at its back face. The edge vetoes (20 in total) define the boundary of the openings. There is a gap of 200μm between modules, a gap filled by the wrapping material around each detector.

and its modularity is obtained from a class II geodesic triangulation of an icosahedron as explained in the next chapter. As a result of the geodesic breakdown, there are nine distinct modular shapes which make up the 240 detectors: one truncated

Inner radius	260 mm
Outer radius	480 mm
Active modules	220
Edge vetos	20
Number of pentagons (P)	10
Number of hexagon A	50
Number of hexagon B	50
Number of Hexagon C	50
Number of Hexagon D	40
Number of HD type 1	10
Number of HD type 2	10
Number of VT type 1	10
Number of VT type 2	10

Table 5.2: Some other properties of the shower calorimeter.

pentagonal pyramid (P), four different types of truncated hexagonal pyramids (A, B, C and D) and four different types of truncated trapezoidal pyramids (HD and VT). The average thickness of a detector module is 12 radiation lengths ($12\,X_o$) and the average solid angle it subtends is $0.004 \times 4\pi$. The dimensions of the nine different shapes have been determined in such a way as to leave a gap of 200μm between adjacent modules in the entire calorimeter. However, the gap is not an air gap. Rather, it accounts for the surface treatment and the wrapping of the modules. Each of the modules with pentagonal and hexagonal shapes is viewed by a 3-inch photomultiplier tube (PMT) with quartz window while the other modules are each readout with a 2-inch PMT also with quartz window, (the spectral response of CsI peaks in the UV region to which the quartz is transparent). The PMT are glued to the back faces of the modules with a 300μm layer of silicon elastomer of Sylgard 184. Some parameters of the calorimeter are cataloged in table 5.2. The information regarding the individual modular shapes are compiled in the following tables 5.3-5.11 and the shapes themselves are also shown in the figures 5.9-5.18. The dimensions of the modules were submitted (for their fabrication) to the companies specialized in the growth of CsI. Twenty-five of them were produced by Bicron corporation while the rest are being made in Kharkov (Ukraine).

Pentagon P						
Volume (cm^3)	962.560 ± 52.530					
	Front			Back		
Surface (mm^2)	2183.271			7469.084		
Vertices (mm):						
	30.303	0.000	260.000	56.048	0.000	480.000
	9.364	28.820	260.000	17.320	53.305	480.000
	−24.515	17.811	260.000	−45.344	32.944	480.000
	−24.515	−17.811	260.000	−45.344	−32.944	480.000
	9.364	−28.820	260.000	17.320	−53.305	480.000

Table 5.3: Properties of the pentagonal pyramid.

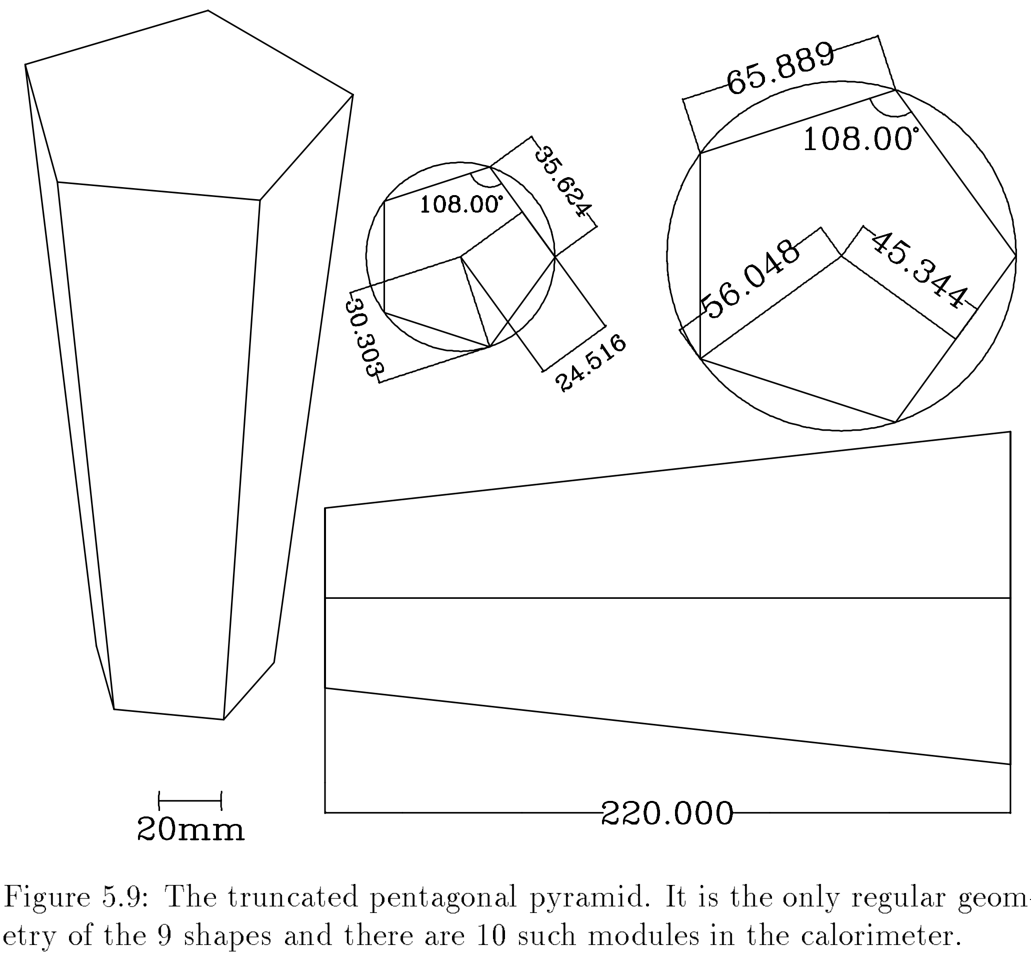

Figure 5.9: The truncated pentagonal pyramid. It is the only regular geometry of the 9 shapes and there are 10 such modules in the calorimeter.

Hexagon A						
Volume (cm^3)	1461.706 ± 46.802					
	Front			Back		
Surface (mm^2)	3144.369			10749.830		
Vertices (mm):						
	37.126	−0.004	260.000	68.642	−0.004	480.000
	17.850	27.058	260.000	32.997	50.038	480.000
	−17.850	27.058	260.000	−32.997	50.038	480.000
	−37.126	−0.004	260.000	−68.642	−0.004	480.000
	−19.348	−29.338	260.000	−35.768	−54.248	480.000
	19.348	−29.338	260.000	35.768	−54.248	480.000

Table 5.4: Properties of the hexagonal pyramid A.

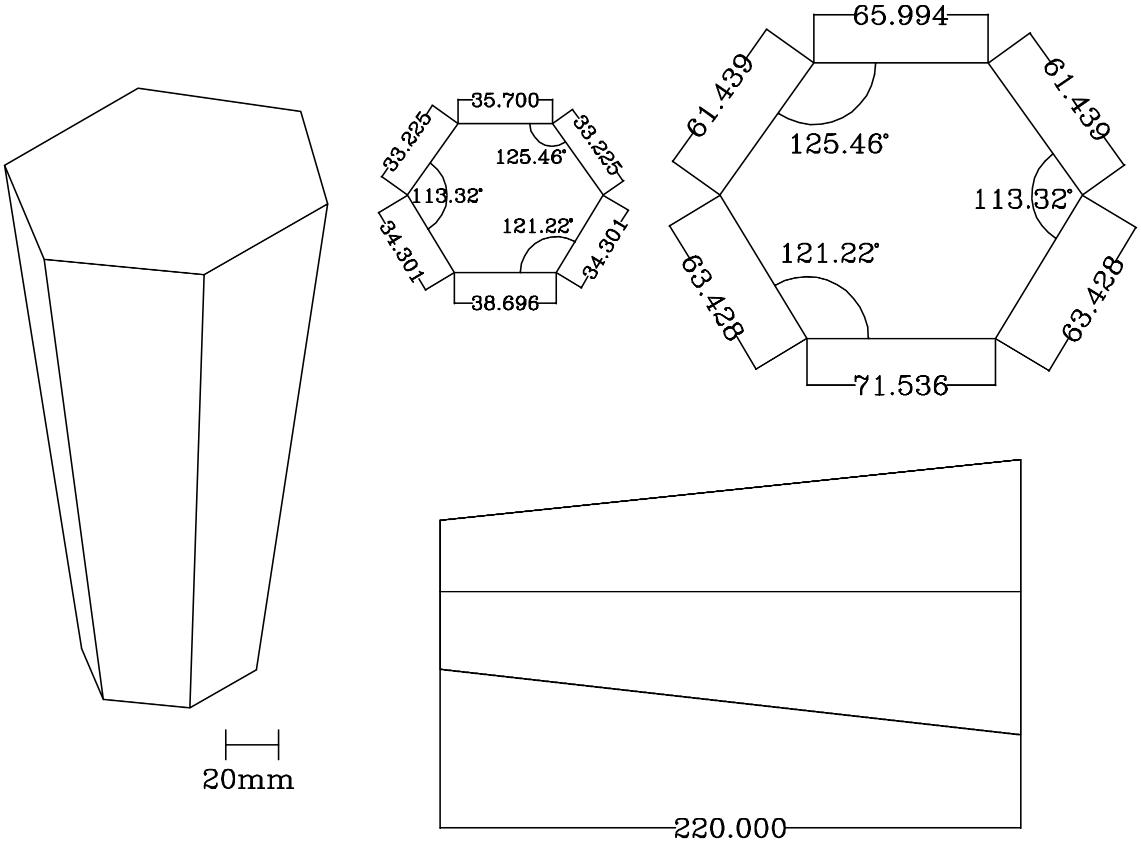

Figure 5.10: The truncated hexagonal pyramid A. There are 50 such modules in the calorimeter. Each pentagon is surrounded on all its five sides by hexagon A's.

Hexagon B						
Volume (cm^3)	1582.418 ± 53.021					
		Front			Back	
Surface (mm^2)		3407.554			11648.270	
Vertices (mm):						
	35.974	0.000	260.000	66.515	0.000	480.000
	15.737	31.726	260.000	29.100	58.657	480.000
	−21.162	31.343	260.000	−39.124	57.948	480.000
	−35.147	0.000	260.000	−64.981	0.000	480.000
	−21.162	−31.343	260.000	−39.124	−57.948	480.000
	15.737	−31.726	260.000	29.100	−58.657	480.000

Table 5.5: Properties of the hexagonal pyramid B.

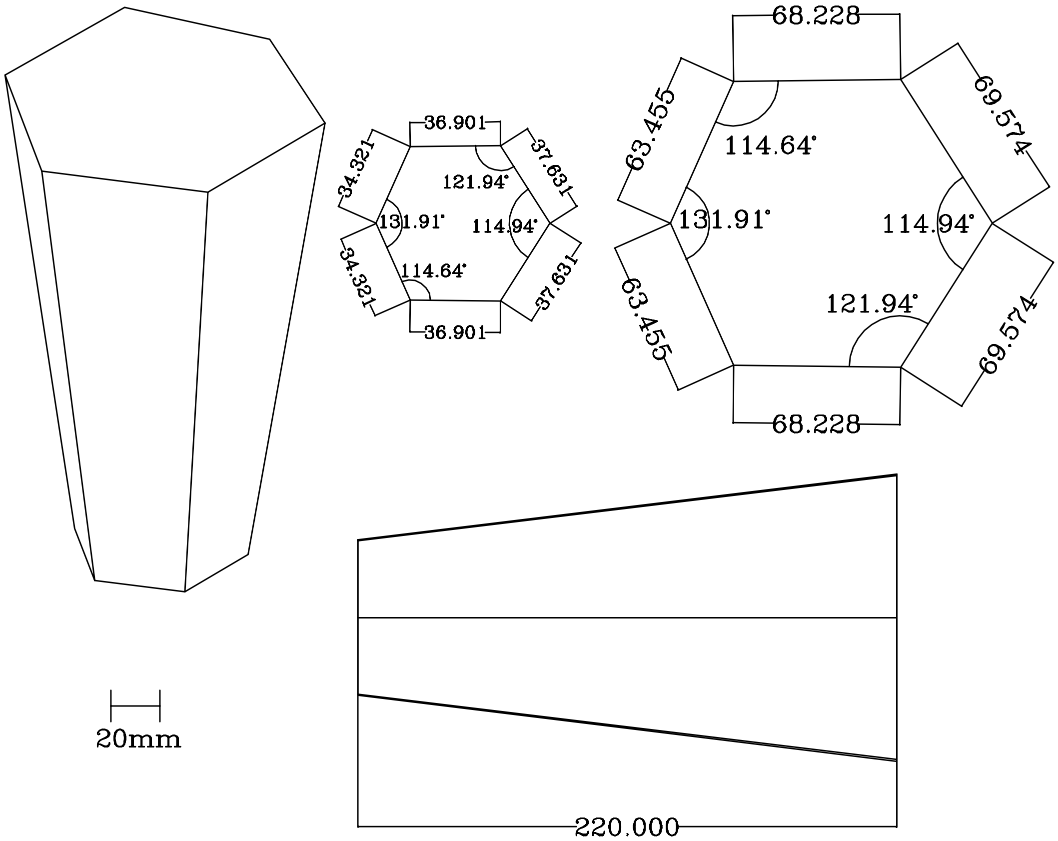

Figure 5.11: The truncated hexagonal pyramid B. There are also 50 hexagon B in the calorimeter.

Hexagon C						
Volume (cm^3)	1718.461 ± 59.262					
	Front			Back		
Surface (mm^2)	3722.305			12722.530		
Vertices (mm):						
	39.306	−0.002	260.000	72.665	−0.002	480.000
	19.365	31.084	260.000	35.797	57.471	480.000
	−19.365	31.084	260.000	−35.797	57.471	480.000
	−39.306	−0.002	260.000	−72.665	−0.002	480.000
	−19.956	−32.037	260.000	−36.891	−59.231	480.000
	19.956	−32.037	260.000	36.891	−59.231	480.000

Table 5.6: Properties of the hexagonal pyramid C.

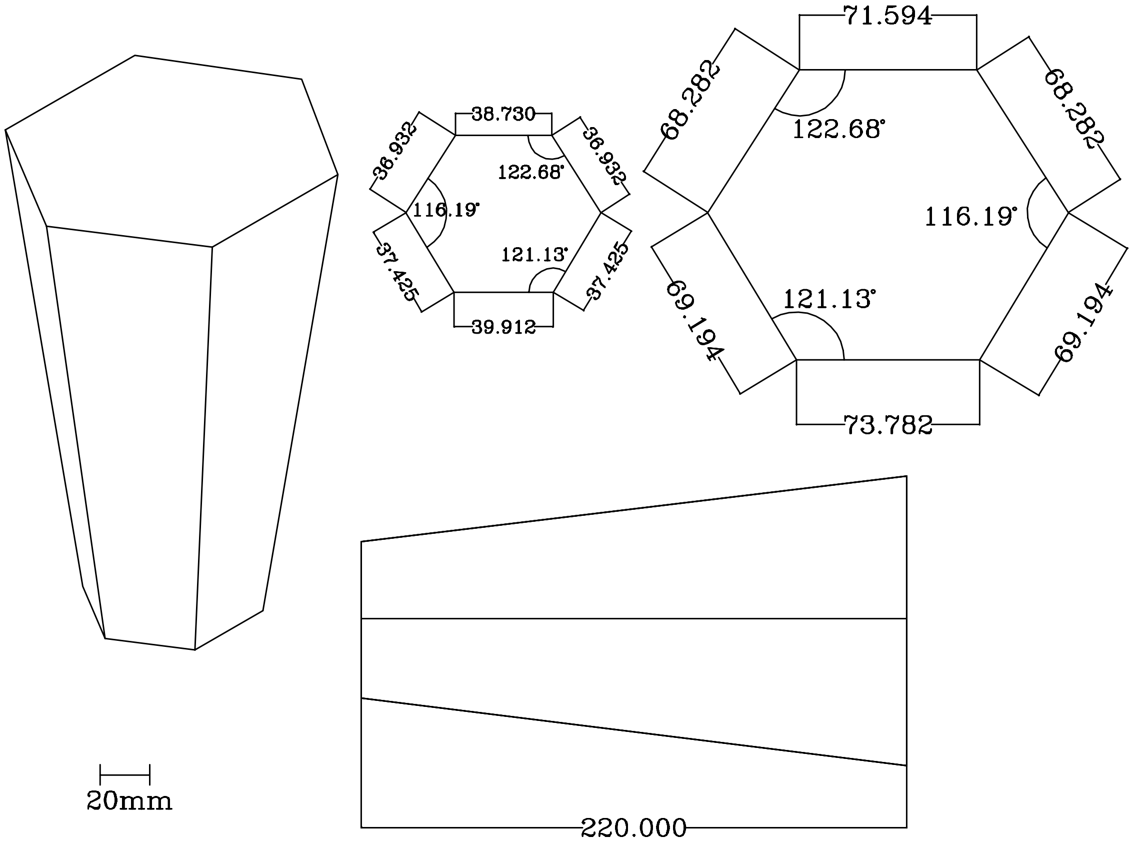

Figure 5.12: The truncated hexagonal pyramid C. The calorimeter contains 50 hexagon C.

Hexagon D						
Volume (cm^3)	1655.996 $\pm$ 60.441					
		Front			Back	
Surface (mm^2)		3531.648			12064.370	
Vertices (mm):						
	36.410	0.000	260.000	67.318	0.000	480.000
	18.503	30.714	260.000	34.210	56.787	480.000
	-19.135	31.753	260.000	-35.373	58.708	480.000
	-38.992	0.000	260.000	-71.957	0.000	480.000
	-19.135	-31.753	260.000	-35.373	-58.708	480.000
	18.503	-30.714	260.000	34.210	-56.787	480.000

Table 5.7: Properties of the hexagonal pyramid D.

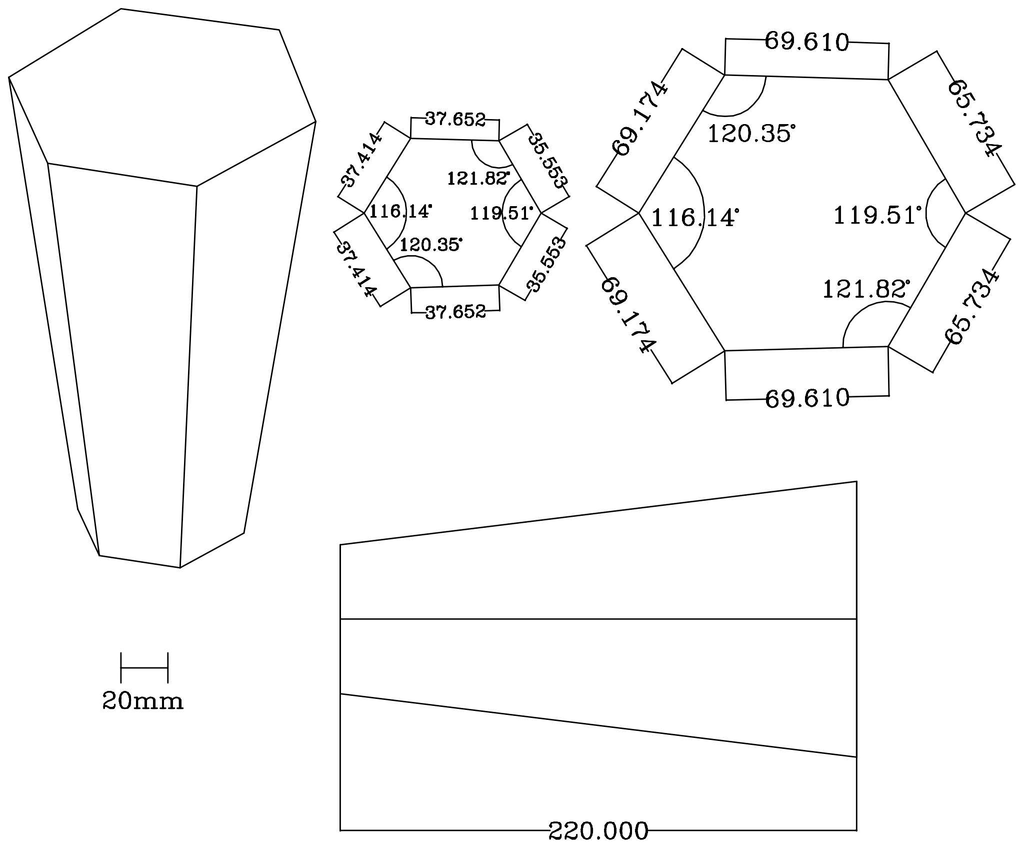

Figure 5.13: The truncated hexagonal pyramid D. There are 40 hexagon D in the calorimeter instead of 50 as the other types of hexagonal pyramids.

	Half Hexagon D 1 (HD1)					
Volume (cm^3)	797.164 $\pm$ 44.143					
		Front			Back	
Surface (mm^2)		1757.195			6018.222	
Vertices (mm):						
	36.352	0.100	260.000	67.259	0.100	480.000
	18.503	30.714	260.000	34.210	56.787	480.000
	-19.135	31.753	260.000	-35.373	58.708	480.000
	-38.860	0.100	260.000	-71.894	0.100	480.000

Table 5.8: Properties of the trapezoidal pyramid HD1.

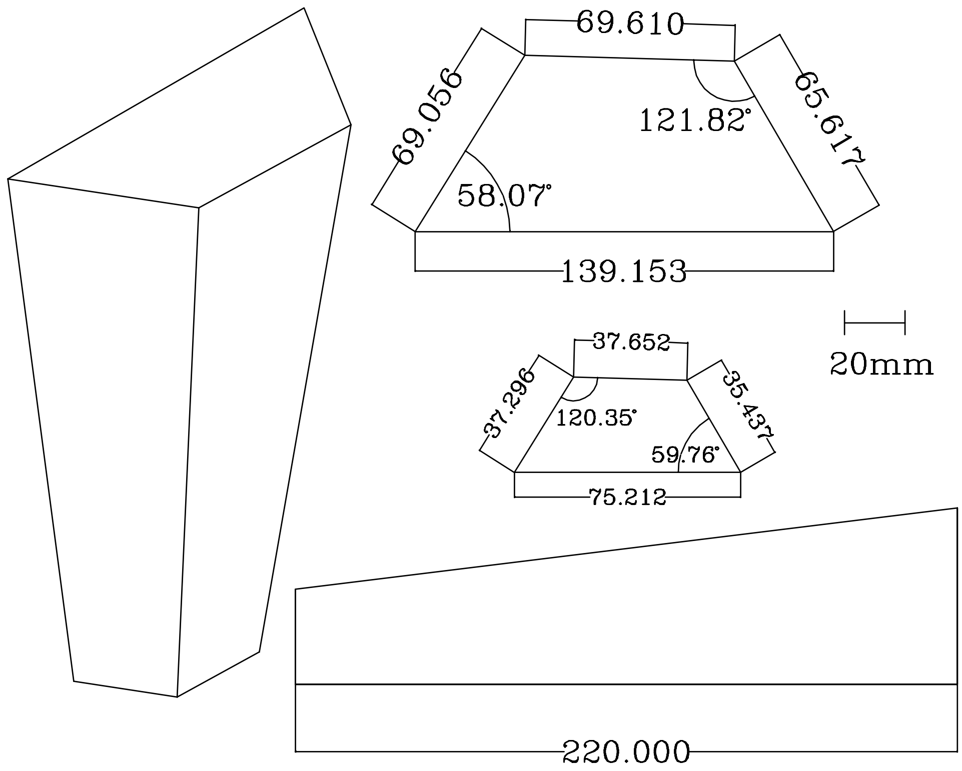

Figure 5.14: The truncated trapezoidal pyramid HD1. There are 10 of these modules in the calorimeter. In the original geodesic breakdown, this shape and its mirror symmetry HD2 generate the hexagonal pyramid D. As a result, they have been named HD for Half hexagon D. In the limit of zero gap between modules in the calorimeter, HD1 and HD2 would perfectly reproduce the hexagon D.

	Half Hexagon D 2 (HD2)					
Volume (cm^3)	797.164 ± 44.143					
	Front			Back		
Surface (mm^2)	1757.195			6018.222		
Vertices (mm):						
	38.860	0.100	260.000	71.894	0.100	480.000
	19.135	31.753	260.000	35.373	58.708	480.000
	−18.503	30.714	260.000	−34.210	56.787	480.000
	−36.352	0.100	260.000	−67.259	0.100	480.000

Table 5.9: Properties of the trapezoidal pyramid HD2.

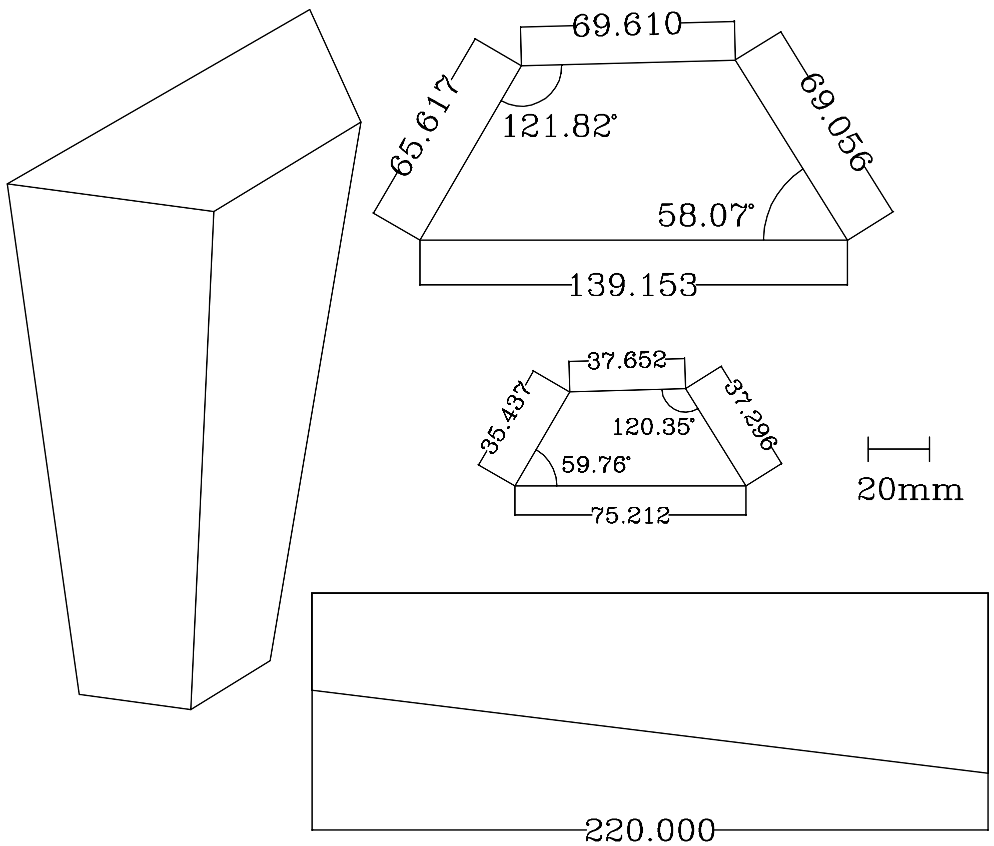

Figure 5.15: The truncated trapezoidal pyramid HD2. The calorimeter contains 10 of them and the are the mirror symmetry of the HD1's.

5.5 Support Structure

The mechanical support of the detector apparatus with the requirement of easy access to inner detectors (the target, the MWPC's and the plastic veto) and upstream detector readouts, has been designed and at the time of this writing, parts of the support structure are under construction. Except for the cosmic veto house, the entire detector apparatus including the electronics is supported on a platform and can be craned in and out of the experimental area ($\pi E1$ area). The veto house consists of a frame with layers of lead bricks and the cosmic veto detectors on the outside of the frame. The bricks prevent self-vetoing in the cosmic veto detectors due to leakage of showers through the back faces of the calorimeter modules. The veto house is equipped with a rail system on the platform and can be wheeled in to enclose the rest of the apparatus on all sides except upstream from the beam where there is a concrete wall for the shielding of the detectors from beam related events, and on the bottom where the platform is. The veto house can also be wheeled out up to five meters, thereby exposing the thermal house around the mechanical support of the calorimeter[2].

The thermal house and the support of the calorimeter are equipped with their own rail system and can be wheeled out (downstream of the beam) up to 85 cm for easy access to the upstream detectors such as the beam counters, the active degrader, etc. The support of the calorimeter consists of a spherical metallic housing with holes within which fit metallic cylinders enclosing the PMT's of the calorimeter modules. The spherical housing is in turn held by a mechanical system as shown in figure 5.16. The housing is made of steel plates that have been forced into semi-spherical geometry to create two hemispheres which are then welded. The support of the twenty plastic veto staves is provided by a thin (one millimeter) carbon fiber cylinder which protects the outer MWPC. The carbon fiber cylinder also provides for smooth and easy insertions and removals of the outer chamber which is equipped with flanges and step-down rings for the support of the inner MWPC (figure 5.1). The target has its own support system with rails and can be wheeled in and out

[2]The mechanical support was designed at the Paul Scherrer Institute by Dr Herman Obermeier and the figure 5.16 was also made there as a result of the design.

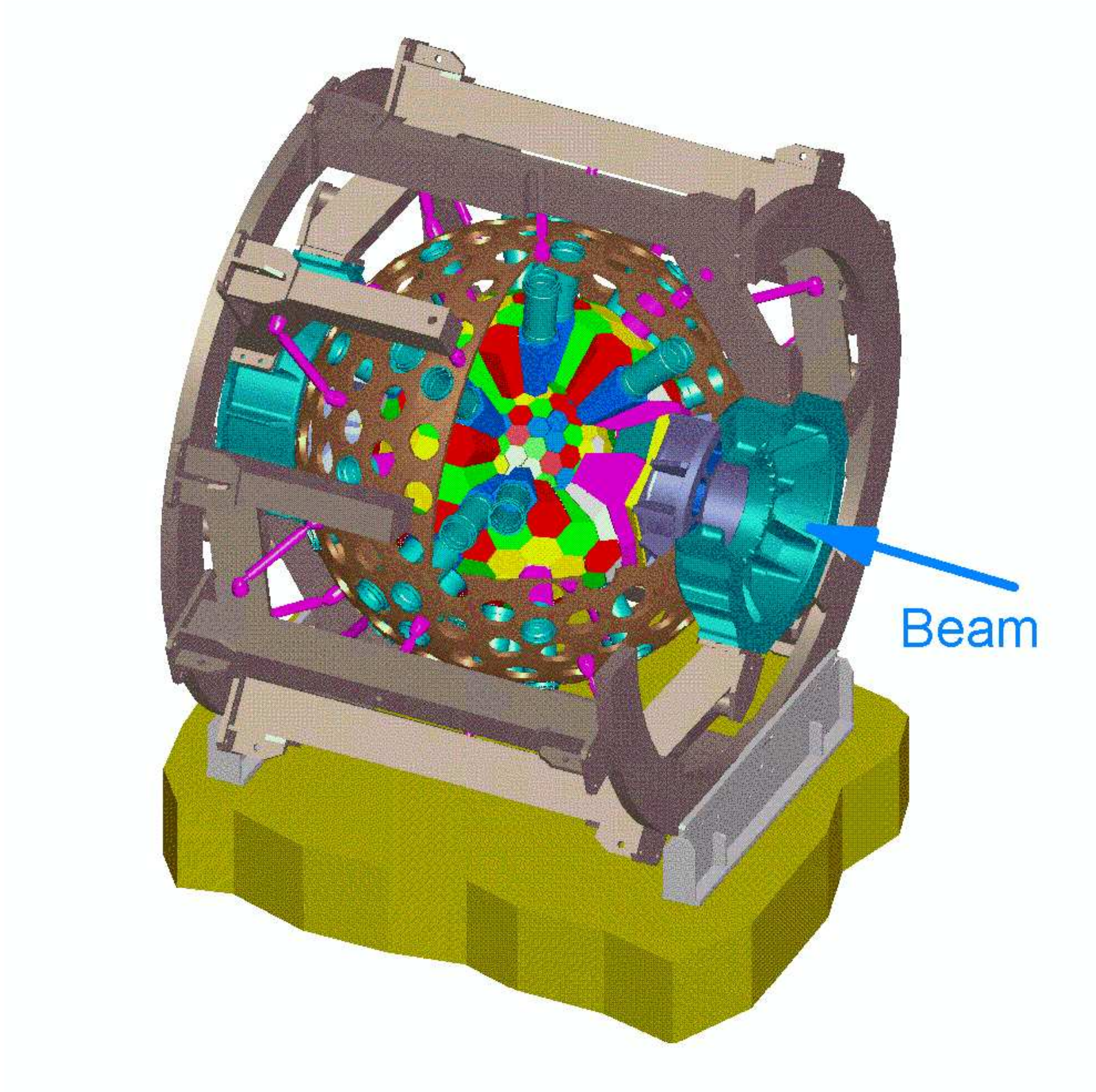

Figure 5.16: The support structure of the calorimeter showing the spherical steel housing, the inner calorimeter modules, the metallic cylinders enclosing the PMT's and the mechanical frame holding the housing.

separately. This facilitates the interchange of the passive and the active target during the data taking process.

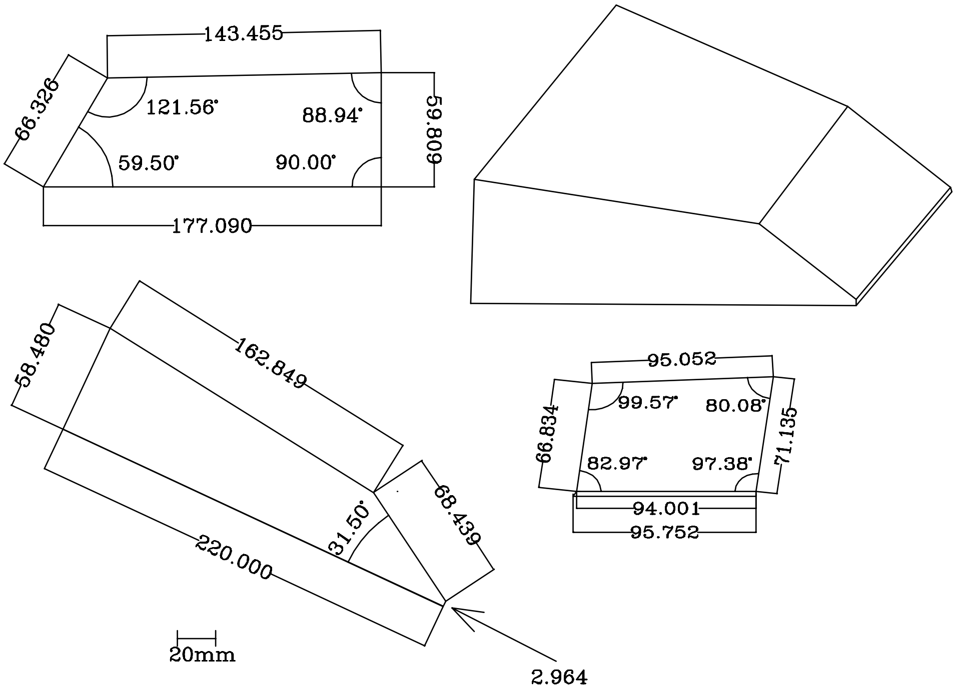

Figure 5.17: The truncated trapezoidal pyramid VT1. These are the edge shower veto detectors. There are 10 of these modules. In the process of the geodesic breakdown, this shape was produced as one HD plus one quarter of hexagon C.

Veto 1 (VT1)						
Volume (cm^3)	1152.812 ± 37.444					
Slanted surface	3368.987 mm^2					
	Front			Back		
Surface (mm^2)	281.220			9341.671		
Vertices (mm):						
	54.603	3.064	260.000	70.422	57.250	480.000
	−39.398	3.064	260.000	−72.820	59.909	480.000
	−39.398	0.100	260.000	−72.820	0.100	480.000
	56.354	0.100	260.000	104.189	0.100	480.000
	46.423	37.722	316.557	(∗)		
	−48.536	39.924	320.150	(∗)		

Table 5.10: Properties of the trapezoidal pyramid VT1. The coordinates of slanted faces in figures 5.17 and 5.18 are indicated by the (∗).

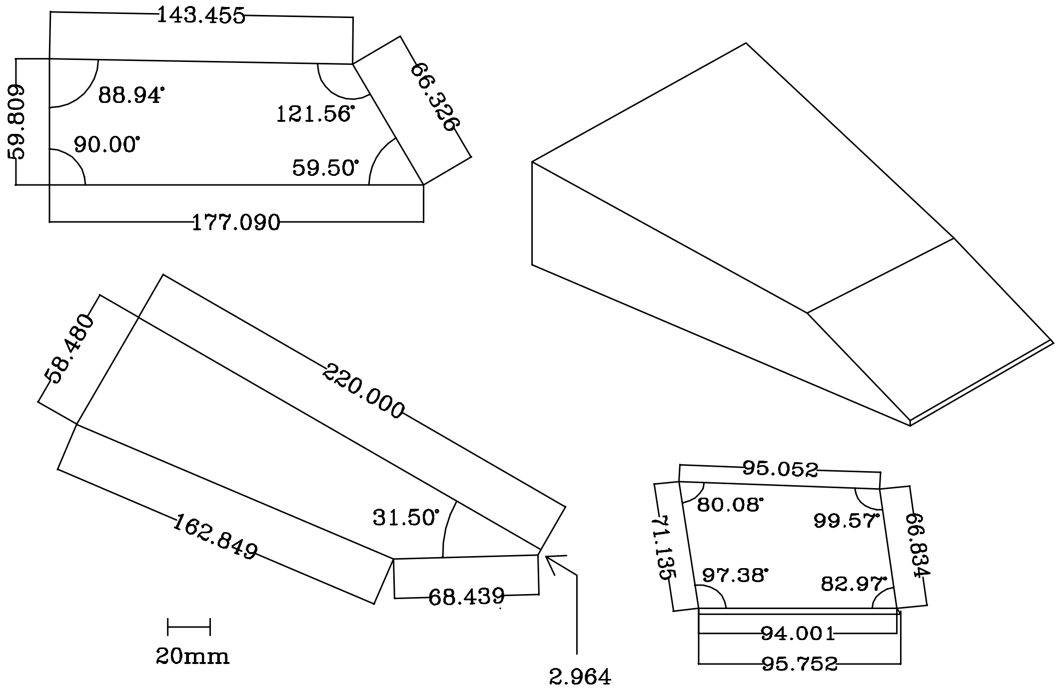

Figure 5.18: The truncated trapezoidal pyramid VT2. These are the other edge shower veto detectors. There are 10 of these modules making a total of 20 shower vetoes. VT2 is a mirror symmetry of VT1. To avoid an interference between the plastic veto detector and the shower vetos, the orginal geometries VT1 and VT2 were trimmed to produced the slanted faces shown figures 5.17 and 5.18.

	Veto 2 (VT2)					
Volume (cm^3)	1152.812 ± 37.444					
Slanted surface	3368.987 mm^2					
	Front			Back		
Surface (mm^2)	281.220			9341.671		
Vertices (mm):						
	39.398	3.064	260.000	72.820	59.909	480.000
	−54.603	3.064	260.000	−70.422	57.250	480.000
	−56.354	0.100	260.000	−104.189	0.100	480.000
	39.398	0.100	260.000	72.820	0.100	480.000
	48.536	39.924	320.150	(∗)		
	−46.423	37.722	316.557	(∗)		

Table 5.11: Properties of the trapezoidal pyramid VT2.

Chapter 6

Design of the Calorimeter

This chapter deals with the actual design of the pion beta calorimeter, a design that ultimately determined the shapes and the number of detector modules described in the previous chapter. The design proceeded with the general guideline of uniform coverage of solid angle by the detector modules, high energy resolution for the elimination of background events, high rate capability, optimization of light collection efficiency for the modules and maximum economy for different modular shapes. These features are obtained in a spherical geometry arrived at by a geodesic breakdown of an icosahedron.

6.1 Geodesic Subdivisions

One commences with an icosahedron, a polyhedron with twenty triangles and thirty-one great circles or geodesics. The great circles fall into three classes of six, fifteen and ten. The first class of six great circles can be seen by considering the twelve pairs of opposite vertices of the icosahedron. In addition, the icosahedron possesses fifteen pairs of opposite edges whose midpoints lead to the second class of fifteen great circles cutting perpendicularly through icosahedron edges. Finally, from the centers of the twenty triangles, ten pairs of opposite centers generate ten more great circles making the third class [Ken-76]. The great circles can be envisioned by assuming an axis going through a pair of opposite vertices, or mid points of opposite edges or centers of opposite faces, and imagining the icosahedron rotating around that axis.

An example of geodesic breakdown is as follows: starting with the family of six great circles, one outlines the faces of the icosahedron using only portions of the fifteen great circles. As a result, each icosahedron edge is subdivided into two pieces

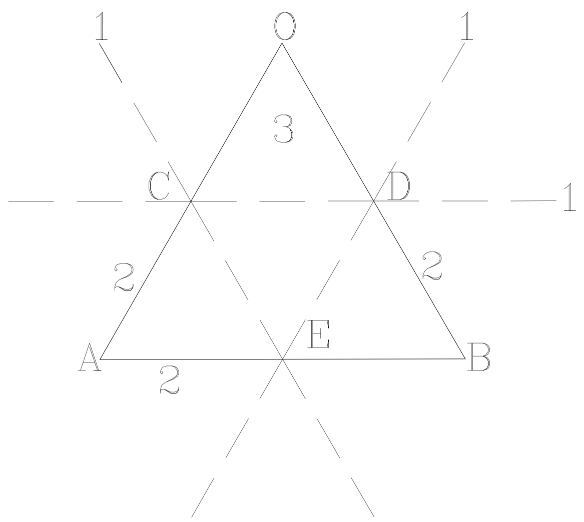

Figure 6.1: One face (labeled 3) of the icosahedron and its subdivisions are shown. The dashed lines (labeled 1) belong to the family of the 6 great circles while the continuous lines (labeled 2) are portions of the 15 great circles mapping out the faces of the icosahedron. Each edge is subdivided into 2 pieces according the two-frequency breakdown. In addition, the subdivisions (line DE for instance) tend to run parallel to the icosahedron edges (line OA) making this breakdown the class I type of subdivisions.

and the process is called a two-frequency breakdown. In addition, the subdivisions tend to run parallel to the icosahedron edges and this is known as class I breakdown as shown in figure 6.1.

As another example of geodesic breakdown, one begins with the fifteen great circles and simply removes the portions that outline the edges of the icosahedron. The result is also a two-frequency breakdown. However, contrary to the previous breakdown, this one has no complete great circles and the divisions run perpendicularly across icosahedron edges that have been removed: this is a class II breakdown.

The thirty-one great circles could be specified by a symmetry triangle. Rotated and reflected a number of times, the symmetry triangle will reproduce an icosahedron face as shown in figure 6.1 where 4 rotations and reflections of the symmetry triangle OCD will reproduce the icosahedron face OAB. Therefore, 4×20 such rotations and reflections will reproduces the entire icosahedron with the family of six great circles and portions of the fifteen. Any further subdivision made in the symmetry triangle will be propagated throughout the whole icosahedron. Therefore, the breakdown process starts with a triangular polyhedron face which is subdivided with a three-way grid according to the breakdown frequency. The vertices of the grid are then pushed outward until they are all at the same distance from the center of the polyhedron (in the case of a spherical geometry). Then a set of rotations and reflections will generate the whole sphere and some lines of the subdivisions will map out the great circles of the icosahedron.

6.2 Modularity of the Calorimeter

The pion beta calorimeter is produced with a class II type of breakdown and frequency 10. In the class II breakdown, the triangle that is drawn and subdivided is not a polyhedron face. Rather, the class II triangle straddles the common edge of two polyhedron faces and its base joins their centroid as displayed in figure 6.2. There are 60 such triangles clustered five to an icosahedron vertex. The class II triangles are what the class II breakdown actually subdivides. For an f-frequency breakdown, one makes an f/2 subdivisions of the class II triangle which, on reflection, produces an f divisions of the common edge, i.e. an f-frequency subdivision.

The coordinates of the vertices are obtained as follows: each vertex is assigned three numbers (n_x, n_y, n_z) whose sum is always the frequency of the breakdown as shown in figure 6.3. The coordinates in the local reference frame are given as [Ken-76]

$$x = n_x \sin(72^\circ), \tag{6.1}$$

$$y = n_y + n_x \cos(72^\circ), \tag{6.2}$$

$$z = f/2 + n_z/(2\cos(36^\circ)). \tag{6.3}$$

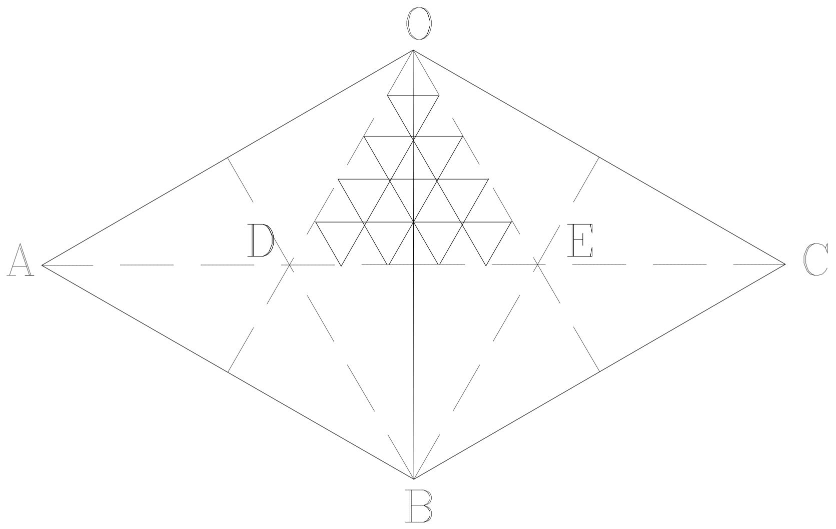

Figure 6.2: An example of a class II breakdown. The class II triangle is not an icosahedron face. The class II triangle ODE straddles the common edge OB of the two polyhedron faces OAB and OBC. For a 10-frequency breakdown, one makes a 5-frequency breakdown of the class II triangle which, on reflection DEB, produces the full 10-frequency breakdown.

The coordinates in the world reference frame are given by two rotations. The first one around the z-axis by an angle ϕ_z followed by a rotation around the new y-axis by θ_y. ϕ_z and θ_y are inherent to the geometry of the icosahedron. For one hemisphere, $\theta_y = \arctan(2)$ while $\phi_z = 36, 108, 180, 252$ and 324° with the special case $\theta_y = 0$ and $\phi_z = 0$. The reflection

$$\begin{aligned} \theta_y &\longrightarrow 180^\circ - \theta_y, \\ \phi_z &\longrightarrow 180^\circ + \phi_z \end{aligned}$$

gives the other hemisphere which is rotated with respect to the previous one by 36°. From the center of each pentagon, start portions of five great circles. At $\theta_y = \arctan(2)$ of the 360° circuit, each great circle runs into the center of another pentagon. At the center of a pentagon, five triangles of the icosahedon meet. $\theta_y = \arctan(2)$ is the angle between the line going through the center of a pentagon and the plane of one of the triangles which meet at that center. The angles ϕ_z follow from the fact that, at $\theta_y = \arctan(2)$, the centers of five pentagons are 72° apart.

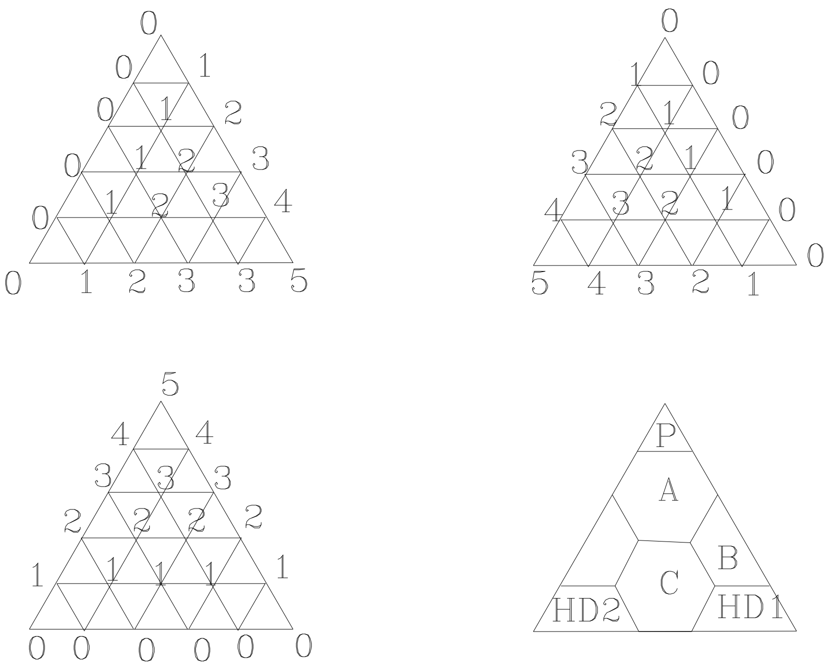

(a) First digit nx

(b) Second digit ny

(c) Third digit nz

(d) Pattern of Pion Beta modules in the class II triangle.

Figure 6.3: The convention for producing the coordinates of the vertices. The class II triangle is subdivided according to the breakdown frequency f, (f = 10 in the case of the pion beta calorimeter). Then the vertices are numbered in an orderly fashion to obtain the first digit n_x. A 60° clockwise rotation gives the second integer n_y. Another 60° rotation results in the third digit n_z. At each vertex $n_x + n_y + n_z = f$. In (d), by removing some lines of the grid, the pattern of the calorimeter modules emerges.

From figure 6.3, five consecutive rotations of 72° will produce a complete pentagon, five hexagon A, five hexagon B and 5 hexagon C. At this point, one has only 10 halves of the hexagon D. The full hexagon D are obtained from mirror symmetry at which point the total count of modules comprises 2 pentagons, 10 hexagon A, 10 hexagon B, 10 hexagon C and 10 hexagon D. When the whole sphere is completed, one has 12 pentagons, 60 hexagon A, 60 hexagon B, 60 hexagon C and 60 hexagon D.

The breakdown algorithm is presented in appendix A.

The next step in the design was to make openings for beam entry and readout of inner detectors and to create the shower vetoes. As a result, the pentagon at $(\theta_y = 0.0, \phi_z = 0.0)$ and its mirror symmetry together with all the modules associated with them were removed. This process leaves only 10 pentagons in the calorimeter, 50 hexagon A, 50 Hexagon B, 50 hexagon C and 40 full Hexagon D and 20 half hexagon D. The shower vetoes were designed as one quarter of a hexagon C plus one half of a hexagon D. There are 20 such veto elements bringing the total number of calorimeter modules to 240. At this stage of the design, there was no gap in the calorimeter to account for the wrapping of the crystals. However, a gap of $200\,\mu$m (between the modules) was required. In addition, the vertices at the front and back "faces" of the modules were all not in the same plane. These problems were dealt with by solving the simultaneous equations describing the intersection of three planes taking into account the gap and requiring that the z-components of the vertices be same, i.e. 260 mm at the front face and 480 mm at the back face of the modules. As a result, the truncated pyramids described in the previous chapter were arrived at and the information regarding their linear and angular dimensions were also obtained for their fabrication. The positions of the modules relative to one another are illustrated in figure 6.4. Also shown in the same figure is the nomenclature which indicates the type and the position of any given module in the calorimeter. The complete algorithm for producing the coordinates of the modular vertices is described in appendix B.

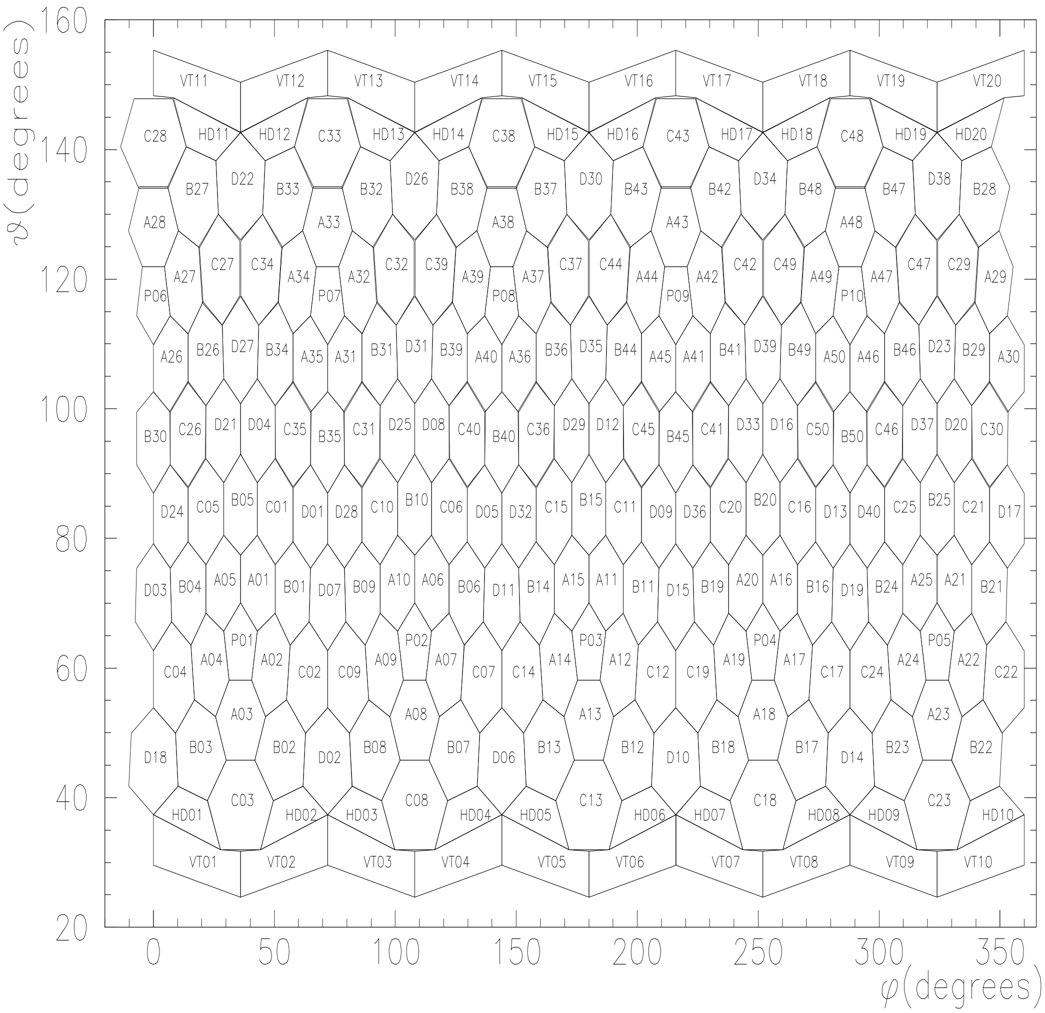

Figure 6.4: A 2-dimensional projection of the calorimeter showing the relative positions of the modules. The different shapes are clearly recognizable and the module names are also supplied. The pentagons for instance are named P01 through P10 while the hexagon A's are A01 through A50 and so on. In the nomenclature of the HD's and the vetoes, the odd numbers are the HD1, VT1 while the even number are the HD2 and VT2.

6.3 Thickness of the Calorimeter

The thickness of the calorimeter was determined after Monte Carlo simulations of its response to pion beta events. Different thicknesses of 10, 12, and 14 radiation lengths (X_o) were considered during the simulations which included the effects of photoelectron statistics and light collection nonuniformity. The detection efficiency as a function of the thickness varied between 0.70 (for $10\,X_o$) and 0.75 (for $14\,X_o$). However, the higher thickness gave a better energy resolution (see figure 6.5) which is necessary in isolating the pion beta process from the background. Therefore, $14\,X_o$ is a better choice for the thickness of the calorimeter whose volume, consequently

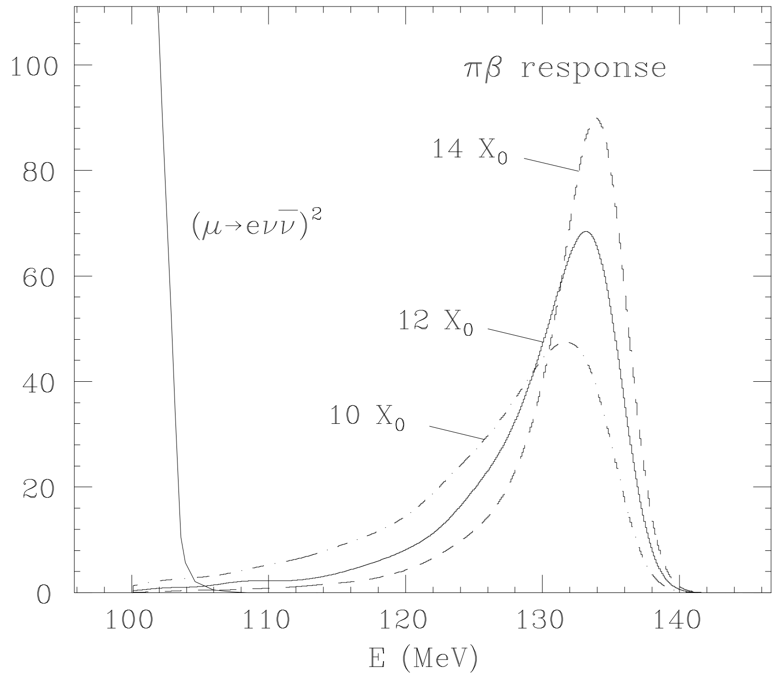

Figure 6.5: Response of the calorimeter to $\pi\beta$ decay events for three different detector thickness: 10, 12 and 14 radiation lengths. These calculations include the effects of light collection nonuniformity and photoelectron statistics. The calorimeter response to accidentally coincident Michel events is also shown. The actual thickness of $12\,X_o$ was selected as a compromise between the cost and the energy resolution of the calorimeter.

the cost, increases with the cube of the outer radius. The actual thickness of $12\,X_o$ was selected as a compromise: the energy resolution is worse but the cost of the calorimeter is less by \$300,000 than what it would be for $14\,X_o$.

6.4 Choice of the Calorimeter Material

In the fall of 1989, the pion beta collaboration undertook a development run during which a 175 MeV/c π^+ parasitic beam was stopped in an active plastic scintillator target in the $\pi E1$ area at the Paul Scherrer Institute. The active target was viewed by two sets of detectors: on one side, an array of seven large CsI modules and a NaI detector on the other side. There were thin plastic veto counters in front of the two sets of detectors which subtended matching solid angles at 180°. The run took place under severe time constraint due to the pending shutdown of the PSI Ring accelerator and the late delivery of the CsI modules from Bicron Corporation. These constraints limited the running time and consequently the counting statistics as can be seen in figure 6.6 which summarizes the results:

Figure 6.6 (a) shows the relative timing between a CsI block and the active target. The measured timing resolution was 1.3 ns FWHM. The CsI modules were readout with EMI 9821QB photomultiplier tubes with quartz window and a nominal rise time of 2.1 ns. In a previous test conducted at the University of Virginia with a ^{60}Co source, the same photomultiplier tubes coupled to good pure CsI crystals of similar size yielded a time resolution of 1.1 ns between two detectors. This meets the energy resolution requirement of the experiment.

Figure 6.6 (b) is the spectrum of the total energy of the NaI and CsI detectors within a delayed pion gate of 80 ns, 10 ns after a valid pion stop. This spectrum includes both charged and neutral showers as no cuts were applied on the plastic veto detectors. The portion of the spectrum below channel 310 was prescaled by a factor of about 100. The pion stopping rate was $2 \times 10^5\,\mathrm{s}^{-1}$. The spectrum is dominated by accidental Michel events in the NaI and CsI detectors. The conversion factor is about three channels per MeV.

Figure 6.6 (c) is the same as figure 6.6 (b) with the selection of only neutral

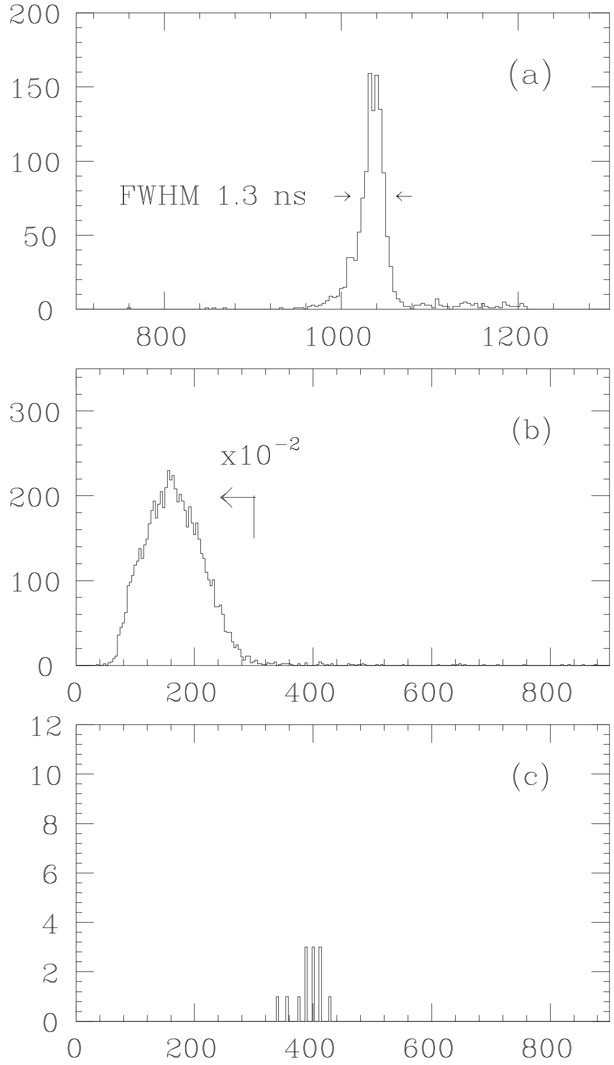

Figure 6.6: The results of the development run in the fall of 1989. A parasitic beam of 175 MeV/c π^+ was stopped in an active target viewed on the sides by an array of CsI and a NaI detectors. The top figure is the relative timing between a CsI block and the target. The central figure is the total energy (CsI plus NaI) detected within a gate, 80 ns long and opened 10 ns after the π^+ stop. The bottom figure is the central one cut on neutrals in the plastic veto detectors in front of the CsI and NaI crystals. A $\pi\beta$ peak emerges but the statistics is low due to time constraints during the data taking.

Radiation length (cm)	1.85
Density (g/cm^3)	4.53
Index of refraction	1.8
Nuclear interaction length (cm)	37.0
Fast component (nm)	305
Fast decay time (s)	7
Slow component (nm)	$\sim$ 450
Slow decay time (s)	30-40
Slightly hygroscopic	

Table 6.1: Some properties of pure CsI.

showers (the plastic veto counters do not fire in either arm). With these requirements, a well defined pion beta peak emerges at the correct energy and the number of counts is consistent with the correct branching ratio of $\sim 1 \times 10^{-8}$. However, the counting statistics is poor — it reflects only about four shifts of running time — because of the time constraints mentioned above. The following conclusions can be drawn from the above results of the development run:

- The attenuation length of pure CsI for its own radiation is quite long, of the order of 1 m. This enables the design of the calorimeter in a "tower" geometry with single-ended detector readout, which is more favorable in high rate measurements.

- The time resolution in large pure CsI crystals of good quality — with over 100 photoelectrons per MeV — is $\sigma \approx 400$ ps per phototube and ranges up to 600 ps for crystals with fifty or fewer photoelectrons per MeV.

- Large crystals subtending 0.4 sr operated very quietly in realistic conditions with beam.

Some other properties of pure CsI are cataloged in table 6.1. Compared to some other inorganic crystals, for instance BaF_2, pure CsI possesses the following advantages which dictate its choice as the calorimeter material: its has a shorter radiation length which means that the volume of a calorimeter like that of the pion beta decay experiment is less than the volume of the same calorimeter in BaF_2. Its has a lower density which suggests a lower weight for the calorimeter with pure CsI. Its higher refractive index indicates that it would be easier to achieve better light collection uniformity for tapered pure CsI crystals like the pion beta modules. Finally, pure CsI has a long nuclear interaction length and consequently, there would be fewer hadronic interactions in CsI, especially in the pion beta modules.

Some other properties of undoped CsI include radiation hardness and temperature dependence of the light output. Wei and Zhu observed a continuous decrease in the light yield of undoped CsI after 1 kRads [Wei-92]. According to their findings, pure CsI can sustain high counting rates up to 10 kRads. Woody et al. reported an increase in the light yield and the decay time of the fast component of pure CsI, and a shift to longer wavelengths at low temperatures Woo-90. A tomography system has been designed and is in operation at the Paul Scherrer Institute with the objective to examine the optical properties of each of the CsI modules prior to the assembly of the calorimeter.

Chapter 7

Experimental Method

The apparatus designed to do a precision measurement of the $\pi^+ \rightarrow \pi^0 e^+ \nu_e$ rate is described throughout chapter 5 and chapter 6. Here, the experimental approach is presented.

7.1 Stopped Pion Method

7.1.1 Decay in Flight

The most precise measurement of the pion beta decay rate to date [McF-85] was carried with an in-flight decay technique. The decay in flight method measures the pion beta decay rate fairly directly by detecting a certain number of pions in a known amount of pion proper time. Moreover, although high pion beam intensity is required, the average raw rates in the detectors are lower by about two orders of magnitude than in the stopped pion experiment. However, important drawbacks to the in-flight technique limit possible improvements of the set-ups of previous experiments and dictate the choice of the experimental method for this precision measurement. The drawbacks to the in-flight technique are discussed below.

Firstly, the in-flight method requires an absolute counting of beam pions as well as an absolute determination of the detector acceptance, efficiency, and pion proper time in the decay region. No scheme has been demonstrated to date to achieve an accuracy significantly better than a percent in counting beam pions at intensities of $\sim 10^8\,\mathrm{s}^{-1}$ and momenta greater than 400 MeV/c. A way around the problem of absolute normalization, is to do a relative normalization using a well measured decay channel of the pion. The only option is $\pi^+ \rightarrow e^+\nu_e$. However a precise knowledge of

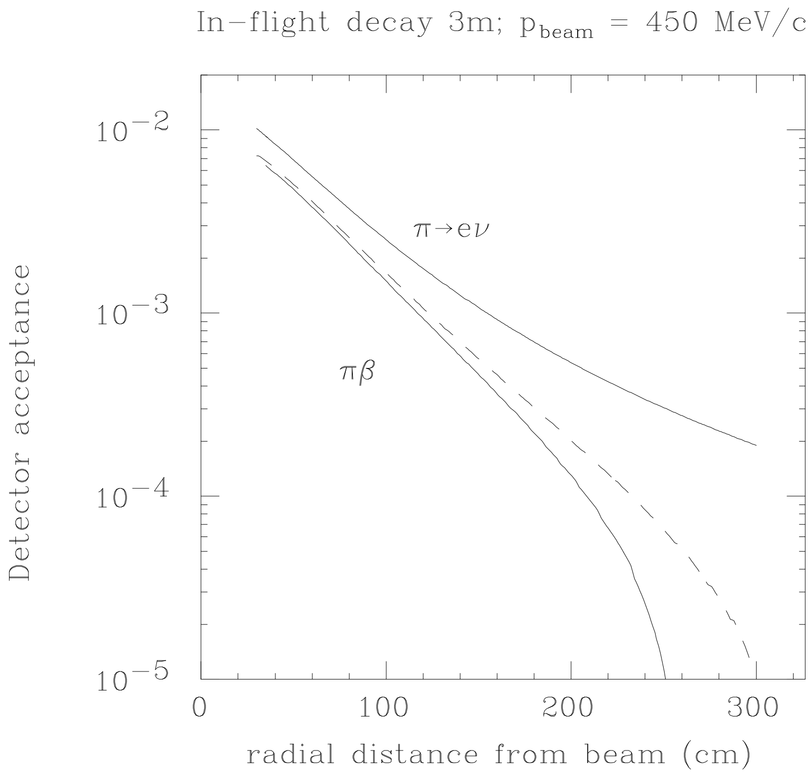

Figure 7.1: Radial dependence of the in-flight detector acceptances for $\pi\beta$ and $\pi^+ \rightarrow e^+\nu_e$ assuming 3 m decay path and a beam momentum of 450 MeV/c. The dashed line shows the change in $\pi\beta$ acceptance corresponding to extending the detector inward radially by 5 cm at the center.

the acceptances and conversion efficiencies for both decays is still required. As shown in figure 7.1, the acceptances for both decays differ by a factor of 2 for reasonable geometries so that the uncertainties do not cancel out in the ratio.

Secondly, the absolute determination of the effective acceptance of a π^0 detector at the desired level of accuracy is difficult due to edge effects. The edge effects arise from the opening to let the beam and the Michel positrons through. However, the edge region contributes most significantly to the total acceptance as shown in figure 7.1 for a set-up with three meters decay region. A radial uncertainty of 1 cm in γ fiducial area translates into a $\sim 3\%$ uncertainty in total acceptance.

Thirdly, the triggers: the pion decays occur over an extended decay region. As a result, there is no unique correlation between the shower and the coordinates of the conversion point. In a relative measurement, an energy-angle cut is necessary for the identification of $\pi^+ \rightarrow e^+\nu_e$ events. The energy-angle cut requires the placement of a tracking detector in front of the calorimeter. In a realistic experimental situation, the tracking accuracy and thus the energy-angle cut efficiency is limited by beam size, divergence and momentum distribution. Moreover, the energy resolution in the calorimeter is important in isolating the $\pi^+ \rightarrow \pi^0 e^+\nu_e$ and $\pi^+ \rightarrow e^+\nu_e$ decays from the background. In an in-flight technique involving more energetic showers, it is more difficult to resolve the $\pi - \mu$ separation of about 30 MeV.

Fourthly, rate limitations: due to the high kinematic boost of all events, their energy separation in the detector is difficult. Particularly troublesome are the radiative decays $\pi \rightarrow e\nu\gamma$ and $\mu \rightarrow e\nu\bar{\nu}\gamma$. The effective duty factor for in-flight measurement is $\sim 1/20$, given the PSI beam structure. This exacerbates the suppression of accidentally coincident background events like $(\mu \rightarrow e\nu\bar{\nu})^2$. In order to suppress them by a time-of-flight cut, a long beam line is needed, which reduces the total available beam pions. Enlarging the shower detector does not work beyond a certain point because the size of the opening determines the total acceptance for pion beta events, not the outer boundary (see figure 7.1).

Finally, size and cost of the detector: figure 7.1 gives a good indication of the size requirements for an in-flight decay detector. For a calorimeter in CsI like in the stopped experiment, the volume would be 1.5×10^6 cm^3 and the cost about \$4 M. This is more than four times the volume of a corresponding shower calorimeter in the stopped experiment (see section 5.4).

7.1.2 Decay at Rest

On the other hand, the disadvantage of the stopped pion technique is that one accepts into the detectors all the Michel positrons from muon decays in the target. In addition, one measures the branching ratio for pion beta decay. Then the decay rate is obtained from the measured branching ratio using the pion life time.

Clearly, the design of the apparatus, especially the size and the cost of the detectors, is affected by the decay method used. The design of the pion beta calorimeter stems from a decay at rest method which relies on the similarity between the $\pi^+ \rightarrow \pi^0 e^+ \nu_e$ and $\pi^+ \rightarrow e^+ \nu_e$ decays in terms of their systematic uncertainties. This enables a relative measurement of the pion beta decay rate without the absolute knowledge of acceptances and conversion efficiencies for both processes as required in the in-flight technique. Furthermore, the relative stopped pion technique finds its justification in the drawbacks to the in-flight technique, particularly the difficulty in controlling the systematic uncertainties with 0.1% accuracy in an absolute measurement of the pion beta decay which occurs with a probability of 10^{-8}.

7.2 Relative Measurement

About 10 ns following the pion stop, a time window known as the delayed pion gate (DPG), of 100 ns is opened. The pion gate is delayed in order to avoid prompt interaction processes such as elastic scatterings or pion charge exchanges. Within this time window, pion beta decay is registered as a detection in coincidence in the shower calorimeter, of the two gamma rays (with energies exceeding the Michel endpoint) which originate from the decay of the neutral pion. Following the delayed pion gate, another time window is opened; however, this time window is mostly sensitive to Michel events as shown in figure 7.2 and can be used to understand their rate and the energy distribution.

Normalization is performed with the $\pi^+ \rightarrow e^+ \nu_e$ events registered within the DPG as the detection in the calorimeter of the single arm showers with total energy exceeding that of the Michel positrons. The relative measurement of the pion beta decay is possible because of the similarity between the showers produced by photons from $\pi\beta$ and by positrons from $\pi^+ \rightarrow e^+ \nu_e$ as shown in figure 7.3. As a result, the detector acceptance and response to the $\pi^+ \rightarrow e^+ \nu_e$ events are very similar to those of the $\pi\beta$ events so that the differences in systematic uncertainties are small and manageable. To account for the difference in the branching ratios the $\pi^+ \rightarrow e^+ \nu_e$

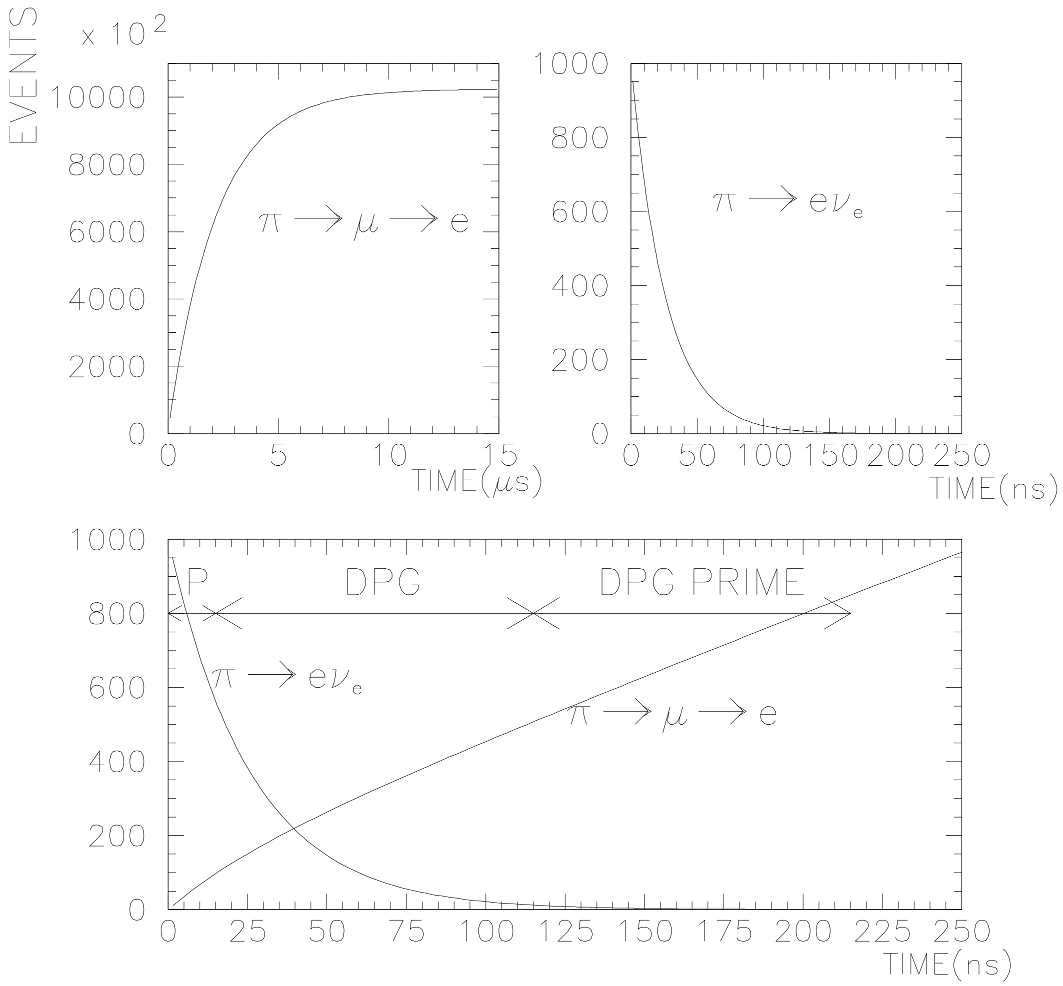

Figure 7.2: Time spectra of Michel and $\pi^+ \rightarrow e^+\nu_e$ events. The Delayed Pion Gate (DPG) is opened $\sim$ 15 ns after a valid π^+ stop in order to avoid Prompt (P) interaction processes. $\pi^+ \rightarrow \pi^0 e^+\nu_e$ and $\pi^+ \rightarrow e^+\nu_e$ events are registered during the DPG. Following the DPG, the DPG Prime (DPG') is mostly sensitive to Michel decays. The accurate branching ratios are not taken into account in these pictures. The temporal distribution of $\pi^+ \rightarrow \pi^0 e^+\nu_e$ event is similar to that of the $\pi^+ \rightarrow e^+\nu_e$ events, the only difference being in the branching ratios of both decays.

events need to be prescaled. Experimentally, the pion beta decay rate is given as

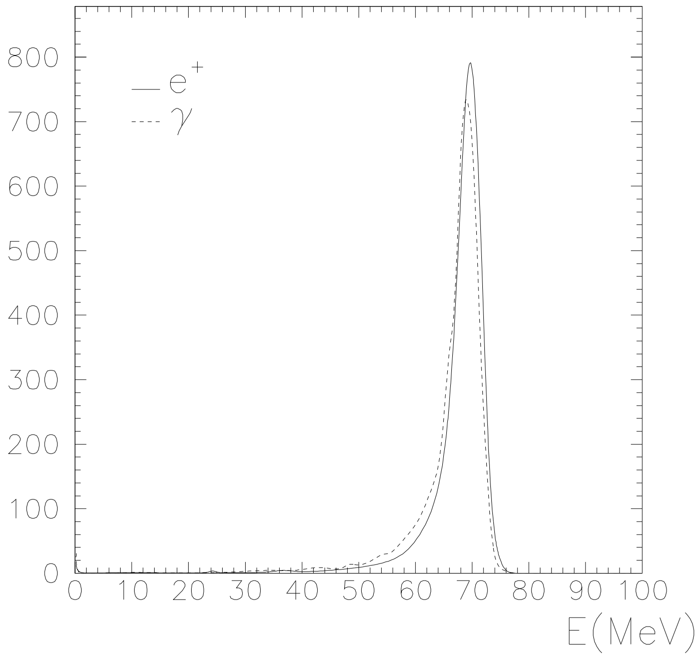

Figure 7.3: Simulated calorimeter responses to 70 MeV photons and positrons. The similarity of the responses can be used to do a relative measurement of the pion beta decay rate by normalizing to $\pi^+ \to e^+\nu_e$ events and accounting for the differences in the acceptances and the branching ratios.

the ratio:

$$\frac{1}{\tau_{\pi\beta}} = \frac{1}{\tau_\pi} \cdot BR_{\pi\beta} = \frac{1}{\tau_\pi} \cdot \frac{BR_{\pi^+\to e^+\nu_e} N_{\pi\beta}}{(N_{\pi^+\to e^+\nu_e} \cdot f_p) \cdot BR_{\pi^0\to\gamma\gamma}} \times \text{corrections}, \tag{7.1}$$

where τ_π is the pion lifetime, the N's represent the respective numbers of good $\pi\beta$ and $\pi^+ \to e^+\nu_e$ events and f_p is the prescale factor for the $\pi^+ \to e^+\nu_e$ trigger. The above corrections include ratios of the following quantities for the two triggers respectively:

- Shower detector acceptances. The differences in the acceptances for pion beta and $\pi^+ \to e^+\nu_e$ events are due to the fact the two gamma rays from a pion beta event are not collinear. As explained in chapter 4, the deviation from collinearity reflects the spread in the recoil energy of the original π^0.

- Live time corrections. They are determined experimentally and are inherent to the data acquisition process.

- Neutral shower self-vetoing due to backsplash. A fraction of the shower initiated in the calorimeter proceeds in the opposite direction of the original particle and leaks through the front faces of the calorimeter modules. A valid neutral shower could be vetoed by the plastic veto detectors which are the first material encountered by the shower back-splash.

- In-flight annihilations of positrons in the target, air and charged particle detectors. The positron annihilation produces two gamma rays and as a result, the original particle can not be identified as a charged particle.

- Leak-through of γ's from π^0 decay which did not deposit any energy in the calorimeter. A fraction of the gamma rays traversing the shower calorimeter escape detection because they do not convert and therefore do not initiate showers.

- Instrumental inefficiency of the MWPC's and fast veto counters.

- Acceptance corrections due to finite size of pion stopping distributions. The horizontal and vertical distributions are measured using the active target while the range distribution is obtained from a measurement of the pion range curve. Unlike the gamma rays from pion beta decays, the positrons from $\pi^+ \to e^+\nu_e$ decays loose some energy in the target and suffer net defections from their original directions via multiple scatterings. The energy losses and the deflections depend on the points of origin of the positrons, i.e., the stopping distributions. This results in further differences in the acceptances for pion beta and $\pi^+ \to e^+\nu_e$ decays.

7.3 Systematic Uncertainties

The main sources of systematic uncertainties have been stated in in the previous section. The size of the systematic uncertainties is determined by the accurate calculation of the following:

(1) the distribution of the deposited energy as well as the geometry of the shower spreading,

(2) the leakage of shower through the back of the calorimeter,

(3) the shower backsplash, and

(4) the in-flight annihilation of positrons.

The above mentioned effects have been calculated using three different simulation codes: ITS, EGS4 and GEANT. A simplified planar detector geometry was used for the simulation in order to avoid any bias or inaccuracy resulting from the definition of more involved geometry in these codes. The detector consisted of a target counter, a thin plastic veto counter (PV) and twelve radiation lengths of CsI. In this case also, monoenergetic photons and positrons of 70 MeV were thrown into and tracked throughout the detector. By appropriately choosing the origin of the primary photons and positrons, all the points (1)-(4) were addressed. After a careful optimization of the tracking medium parameters, a remarkable agreement was observed between the results of the three simulation codes. The profiles of the shower spreadings as calculated by GEANT, are shown in figure 7.8. The top panel of figure 7.4 shows the line-shape in CsI of 70 MeV photon-induced showers. In the region above the threshold of 50 MeV, the agreement between the calculations of the three different codes is excellent. The integrated detection efficiencies above 55 MeV agree to $\sim 0.1\%$, which is remarkable. Similar agreement is found for the energy leaked through the back of the calorimeter.

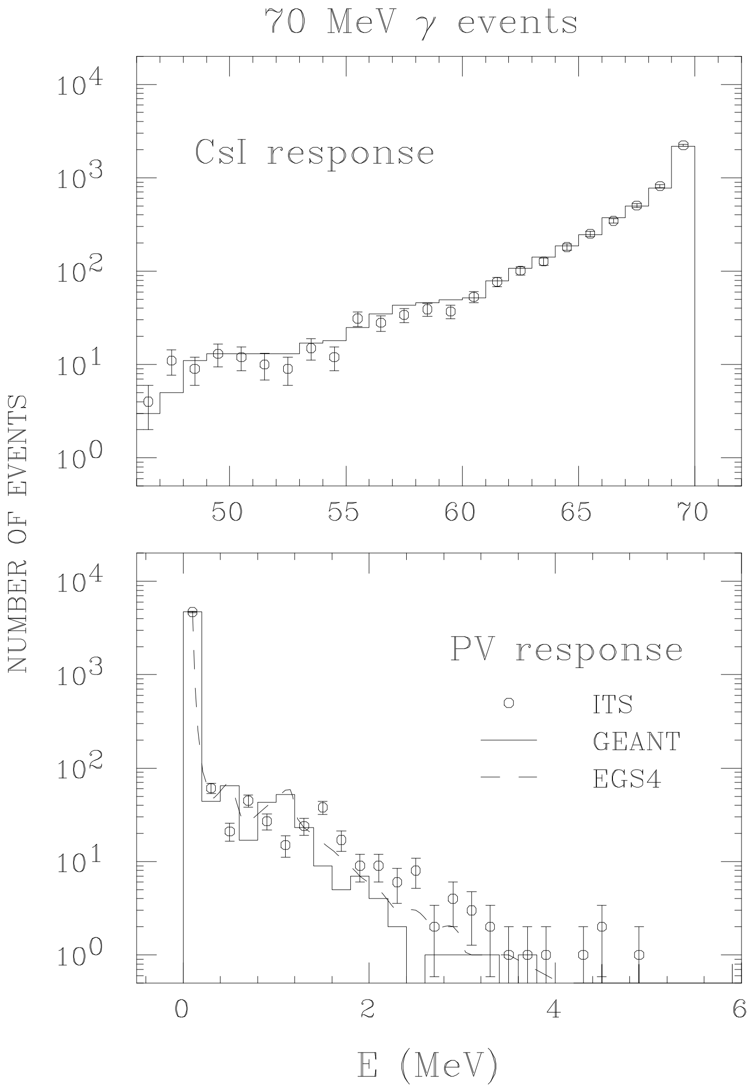

Figure 7.4: The line-shapes of 70 MeV photon-induced showers in CsI as calculated by GEANT, ITS and EGS4 (top panel). The calculations of the three codes show excellent agreement, especially in the region above the threshold of 50 MeV. The bottom panel shows the response of the plastic veto counter to showers initiated by photons which originate in the target. Here too, the results of the three different calculations agree remarkably well.

The response of the plastic veto counter to showers initiated by photons originating in the target is presented in the bottom panel of figure 7.4 for ITS, GEANT and EGS4. This response is a combination of the processes (3) and (4) and affects the overall detection efficiency for pion beta decays. The integrated yields above minimum ionizing particle (MIP) threshold differ by $\sim 0.5\%$ of the total number of shower histories. However, raising the threshold by 0.4 MeV improves the agreement to about 0.1% between ITS and GEANT results and $\sim 0.3\%$ between ITS and EGS4 calculations.

To isolate the process (3), the monoenergetic 70 MeV photons were thrown perpendicularly incident onto the CsI detector with their origin at the front face of the CsI detector. A fraction of the showers proceed in the direction opposite to that of the original photons and flows back across the front face of the CsI detector. This shower backsplash is shown in top panel of figure 7.5. ITS and Geant calculations of the energy flow back across the front face of the CsI detector agree to better that 0.1% in an integrated yield above 1 MeV. The EGS4 result is higher by almost one percent. The plastic veto counter is the first detector encountered by the shower backsplash; the response of this counter to the backsplash is shown in the bottom panel of the same figure 7.5 and is the more relevant quantity from the standpoint of corrections to the detection efficiency. A very small fraction of the backsplash consists of charged particles, i.e. less than 1% of the histories registered above the MIP threshold. The integrated yields above the MIP threshold differ by less than 0.1% of the total number of histories for GEANT and EGS4 calculations. However, the ITS result is slightly higher at large deposited energies.

In conclusion, the processes which affect the detection efficiency of pion beta decays occur at the level of few percent probability. A remarkable agreement has been observed in the calculations of detection efficiencies using GEANT, ITS and EGS4. Depending on the process considered, the three different calculations agreed at the level of few per mill of better. Since these calculations were carried out, GEANT has been the only code used for the simulations of the various processes affecting the design of the apparatus. This has been due to the fact that the GEANT simulation code includes the most comprehensive geometry package and interfaces with

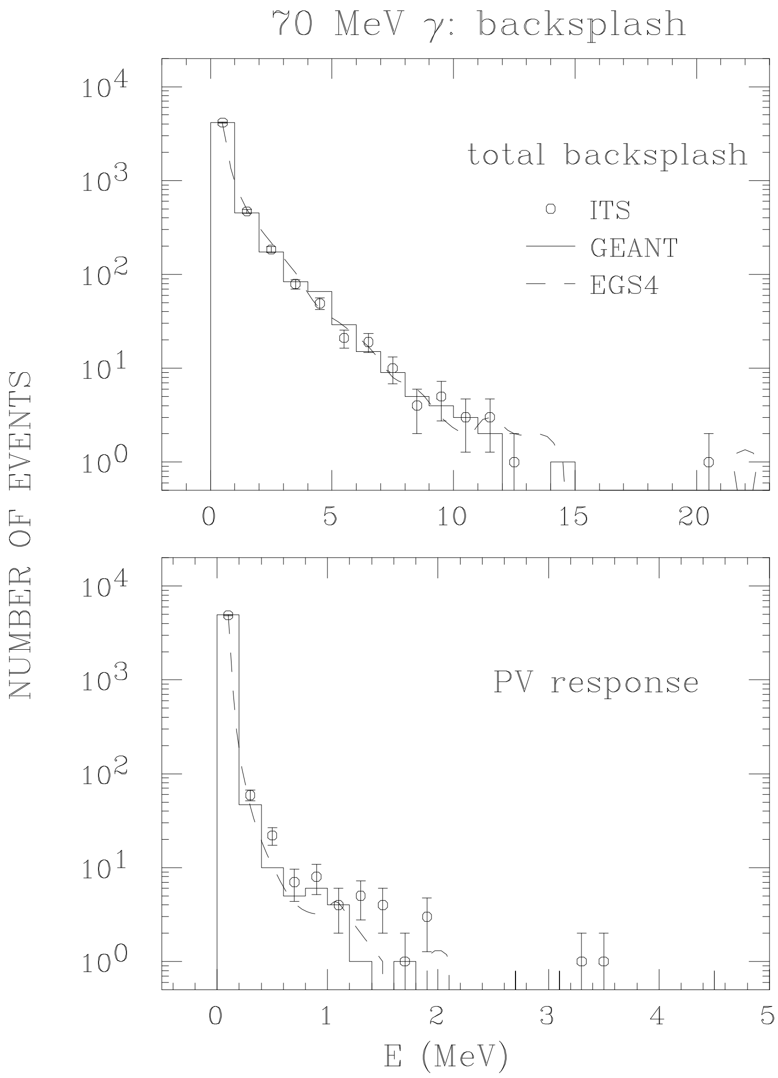

Figure 7.5: The top panel is the total shower backsplash as calculated by the three different codes. This is the total energy flow back across the front face of the CsI detector. The response of the thin plastic veto detector to this backsplash is displayed in bottom panel. A very small fraction of the backsplash consists of charged particles.

CERN library routines. These systematic uncertainties will have to be evaluated experimentally during the set-up and calibration parts and monitored throughout the data taking process.

7.4 Granularity of the Calorimeter

The granularity of the calorimeter was chosen after a detailed simulation and study of the spreadings of the showers produced by γ's and e^+'s. Prior to the simulation of the showers, the detector apparatus was defined in the Geant simulation package as explained below.

7.4.1 Calorimeter in Geant

In the Geant simulation code, the user is expected to provide the information regarding the geometry of the set-up and its position in the master reference frame where the tracking is performed. In the master reference frame, the user also supplies the kinematical information about the reaction under study. In addition, the user must make the necessary arrangement for the read out of the desired quantities. The information needed to run the simulation code is supplied via subroutines where the user is free to take any action.

In the case of the pion beta calorimeter, the nine different shapes were defined and positioned as displayed in figure 7.6. The pentagonal shape, being the only regular geometry, was simple to define. The other shapes, especially the hexagons have been defined as two trapezoids which were patched together to reproduce the original hexagons. The half hexagon D's were defined as trapezoids. The shower vetoes, due to their peculiar geometry, were also defined as two trapezoids connected together. The pentagons, although they can be single entities, were defined as two geometries patched together as shown in figure 7.6.

Once the shapes were defined, the next step in constructing the simulation code was the rotations and translations necessary for positioning each module in order to generate the calorimeter. This was a straightforward task since the rotation angles and translation vectors follow as the result of the geodesic breakdown described in

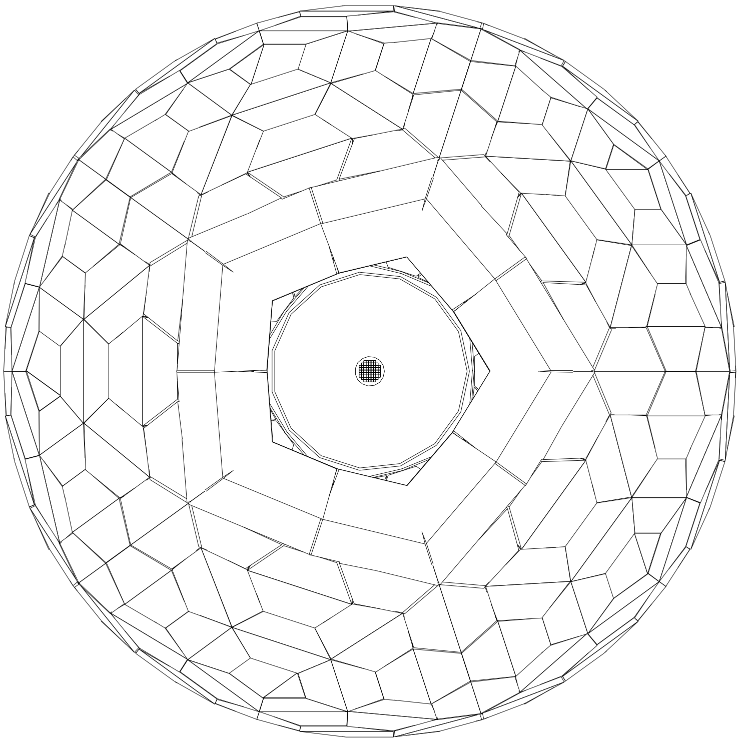

Figure 7.6: The pion beta apparatus as defined and positioned in Geant for the simulations of the reactions relevant to the experiment and the design and understanding of the triggers. Shown here from the center, are the active target, the plastic veto detector and the calorimeter. The pentagons, the hexagons and the vetoes were each defined as two entities which are patched together to get the correct geometries: this process was necessary due to the difficulty in defining irregular objects in Geant. This segmentation in Geant reveals one property of the geodesic breakdown: from a pentagon center to another pentagon center, one can see portions of geodesics as explained in section 6.1

section 6.2. The kinematics parameters for the pion beta process or other reactions of interest were set-up in the appropriate user subroutine and the energy deposited within each of the modules was recorded at the end of each track or whenever necessary during the tracking process via another user subroutine. The tracking medium parameters—their optimization is very important to interpret accurately the simulation results—were adjusted to reflect fine tracking step size and low tracking cut-offs for all shower particles. The light collection non-uniformity and the photoelectron statistics which have been measured during the pion beta test runs, were taken into account for more realistic simulations. A complete simulation code is described in appendix C and one simulated pion beta decay event is shown in figure 7.7.

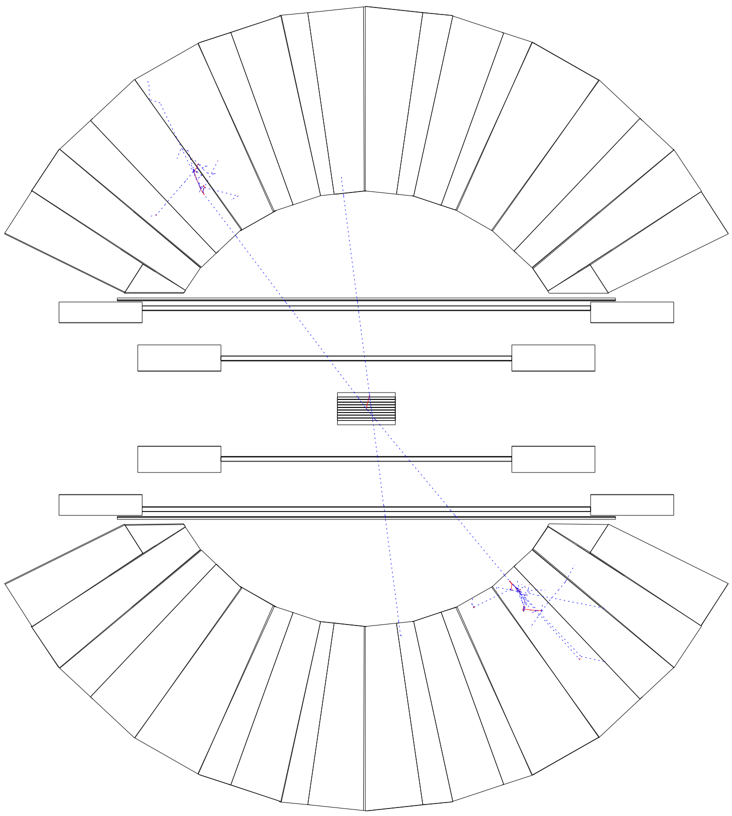

Figure 7.7: A cut view of the calorimeter and the simulation of one pion beta decay event in Geant. The two photons from π^0 decay are the blue dashed lines emerging from the target. The photons reach the calorimeter where they initiate electromagnetic showers all of which are contained within the modules. The e^+ (the red line in the target) from pion beta decay annihilates in the target with an atomic electron. The two gamma rays resulting from the annihilation process are also shown as blue lines coming from the target. The red lines are charged particles.

7.4.2 Granularity

The gamma rays and positrons of 70 MeV — this is approximately the energy of the γ's from pion beta and π^0 decays and e^+'s from $\pi^+ \rightarrow e^+\nu_e$ as explained in chapter 4 — were thrown into the apparatus according to the stopping distributions and tracked throughout the detector volumes, keeping track of the location of the energy deposition at each step. The energy deposited was then histogrammed into one degree conical bins concentric with the direction of the original particle's momentum. From figure 7.8, it is concluded that:

- The mean of the deposited energy as well as the full width half maximum approach saturation within a cone of half-angle $10 - 12°$.

- The shower profiles initiated by e^+'s are similar to that initiated by γ's particularly in the saturation region of the deposited energy: this is important in controlling the systematic errors which result from the normalization of pion beta events to $\pi^+ \rightarrow e^+\nu_e$ decays.

- As indicated by the arrow marked 1, if hit centrally, a detector module will receive 90% of the shower energy. At most three detector modules will receive significant portions of the shower. As shown by the arrow marked 7, clusters of 7 detectors constitute excellent trigger elements since almost all of the shower energy is contained within the conical fiducial volumes of seven modules. However, clusters of three are also satisfactory.

Therefore, the building blocks of the two main data triggers, $\pi\beta$ and $\pi^+ \rightarrow e^+\nu_e$, are overlapping clusters of seven crystals. To each cluster, there corresponds a symmetric one in the opposite hemisphere. The determination of the clusters and their efficiency in detecting the gamma rays and positrons (of 70 MeV) which indeed deposit over ~ 50 MeV in the calorimeter, have been thoroughly investigated. The threshold of ~ 50 MeV is selected so as to discriminate against the Michel e^+'s whose spectrum extends up to ~ 53 MeV as explained in chapter 4. 70 MeV γ's and e^+'s were thrown into the apparatus and the energy deposited into each cluster was

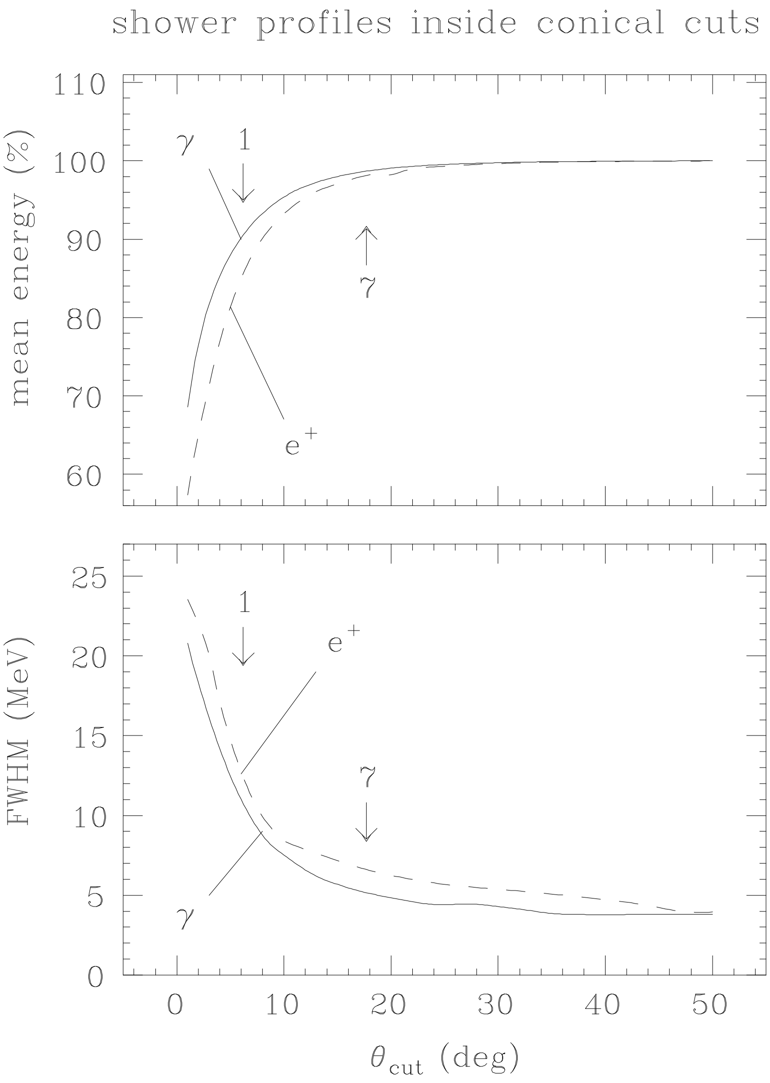

Figure 7.8: Profiles of the electromagnetic shower spreading in the calorimeter. Shown here are the histograms of the means and FWHM's of the energy deposited by the shower inside a conical fiducial subvolume of the calorimeter. The conical subvolumes are defined by the half-opening angles, θ_{cut}. Showers were initiated by 70 MeV photons (solid curves) and positrons (dashed curves) using the Geant simulation package.

recorded. A total of 100,000 shower histories were collected for each type of particles. The vetoes, due to their role as shower vetoes, are not included in the clustering scheme. In addition, a given module cannot belong to more than three clusters: this avoids the degradation of the PMT signals due to excessive splittings. The efficiency of the clustering scheme in detecting the particles whose shower energies exceed the threshold was defined as follows:

- The total energy deposited into the entire calorimeter is greater than the threshold but none of the clusters receive an energy greater than the threshold.

- The total number of events for which the above condition is true divided by the total number of events with energies above the threshold, determines the efficiency of the clusters.

- The energy distribution of the events which satisfy the above condition was displayed in a text histogram similar to that of figure 6.4 except that the names of the modules were replaced by the actual values of the energy deposited in each of the crystals on an event by event basis. By studying the pattern of the shower spreadings, it was possible to make modifications in the clusters. The new clustering scheme was tested in the same manner.

- After several iterations, the average number of elements per cluster was increased from 7 to 9 and the following results were arrived at: with the threshold at 50 MeV, the clustering scheme was 99.3% and 98.6% efficient for 70 MeV photons and positrons respectively. This suggests that, with the present cluster configuration, about seven out of one thousand pion beta decay events will not be detected although these events will deposit more than the threshold energy in the calorimeter.

- The clustering method was also tested against Michel decays. The expected efficiency for suppressing these events in a single arm trigger is 99.7% at 50 MeV. A small fraction (0.3%) of Michel events will deposit

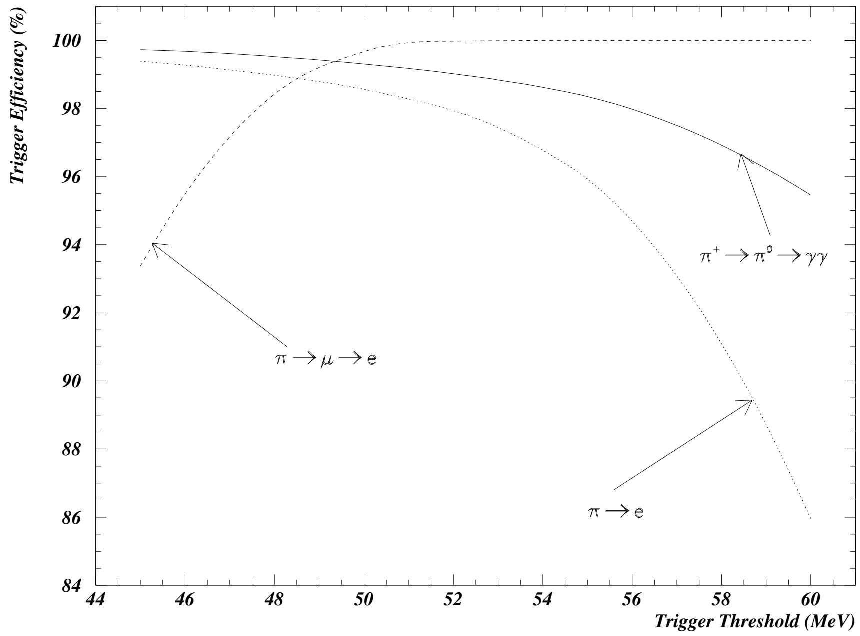

Figure 7.9: The efficiency of the clustering scheme as a function of the trigger threshold. An optimum value for the threshold is $\sim 50\,\mathrm{MeV}$.

more than 50 MeV in the calorimeter and fire at least one cluster. The performance of the clustering method as a function of trigger threshold is displayed in figure 7.9.

7.4.3 Triggers

There are sixty overlapping clusters each of which comprises nine calorimeter modules. One type of clusters is centered around a pentagon and five different types of clusters are centered around each of the hexagon B's. As explained in section 6.2, each pentagon has associated with it, five hexagon A's, five hexagon B's, five hexagon C's, four hexagon D's, one HD1, one HD2, one VT1 and one VT2. Therefore, at the position of a pentagon, six clusters can be identified: one around that pentagon itself and five around the five hexagon B's associated with that pentagon. The rest of the clusters follow from the geodesic subdivisions by propagating

Cluster	#	1	2	3	4	5	6	7	8	9
CL01	9	P01	A01	A02	A03	A04	A05	B05	B01	B04
CL02	9	B01	D01	D07	C02	A02	A01	C01	C35	D28
CL03	9	B02	C02	C09	D02	HD02	C03	A03	A02	P01
CL04	9	B03	A03	C03	HD01	D18	C04	A04	P01	B02
CL05	9	B04	C05	A05	A04	C04	C22	D03	D24	B05
CL06	9	B05	D04	C01	A01	A05	C05	C26	D21	D27
CL07	9	P02	A06	A07	A08	A09	A10	B10	B06	B09
CL08	9	B06	D05	D11	C07	A07	A06	C06	C40	D32
CL09	9	B07	C07	C14	D06	HD04	C08	A08	A07	P02
CL10	9	B08	A08	C08	HD03	D02	C09	A09	P02	B07
CL11	9	B09	C10	A10	A09	C09	C02	D07	D28	B10
CL12	9	B10	D08	C06	A06	A10	C10	C31	D25	D31
CL13	9	P03	A11	A12	A13	A14	A15	B15	B11	B14
CL14	9	B11	D09	D15	C12	A12	A11	C11	C45	D36
CL15	9	B12	C12	C19	D10	HD06	C13	A13	A12	P03
CL16	9	B13	A13	C13	HD05	D06	C14	A14	P03	B12
CL17	9	B14	C15	A15	A14	C14	C07	D11	D32	B15
CL18	9	B15	D12	C11	A11	A15	C15	C36	D29	D35
CL19	9	P04	A16	A17	A18	A19	A20	B20	B16	B19
CL20	9	B16	D13	D19	C17	A17	A16	C16	C50	D40
CL21	9	B17	C17	C24	D14	HD08	C18	A18	A17	P04
CL22	9	B18	A18	C18	HD07	D10	C19	A19	P04	B17
CL23	9	B19	C20	A20	A19	C19	C12	D15	D36	B20
CL24	9	B20	D16	C16	A16	A20	C20	C41	D33	D39
CL25	9	P05	A21	A22	A23	A24	A25	B25	B21	B24
CL26	9	B21	D17	D03	C22	A22	A21	C21	C30	D24
CL27	9	B22	C22	C04	D18	HD10	C23	A23	A22	P05
CL28	9	B23	A23	C23	HD09	D14	C24	A24	P05	B22
CL29	9	B24	C25	A25	A24	C24	C17	D19	D40	B25
CL30	9	B25	D20	C21	A21	A25	C25	C46	D37	D23

Table 7.1: Cluster definitions for the pion beta experiment. There are sixty overlapping clusters in the calorimeter. Each of which contains nine elements. Shown here are the first thirty. The rest are displayed in table 7.2. The first six clusters make a supercluster; the next six another supercluster, and so on. The definitions of the superclusters are presented in table 7.3.

Cluster	#	1	2	3	4	5	6	7	8	9
CL31	9	P06	A26	A27	A28	A29	A30	B30	B26	B29
CL32	9	B26	D21	D27	C27	A27	A26	C26	C05	D04
CL33	9	B27	C27	C34	D22	HD11	C28	A28	A27	P06
CL34	9	B28	A28	C28	HD20	D38	C29	A29	P06	B27
CL35	9	B29	C30	A30	A29	C29	C47	D23	D20	B30
CL36	9	B30	D24	C26	A26	A30	C30	C21	D17	D03
CL37	9	P07	A31	A32	A33	A34	A35	B35	B31	B34
CL38	9	B31	D25	D31	C32	A32	A31	C31	C10	D08
CL39	9	B32	C32	C39	D26	HD13	C33	A33	A32	P07
CL40	9	B33	A33	C33	HD12	D22	C34	A34	P07	B32
CL41	9	B34	C35	A35	A34	C34	C27	D27	D04	B35
CL42	9	B35	D28	C31	A31	A35	C35	C01	D01	D07
CL43	9	P08	A36	A37	A38	A39	A40	B40	B36	B39
CL44	9	B36	D29	D35	C37	A37	A36	C36	C15	D12
CL45	9	B37	C37	C44	D30	HD15	C38	A38	A37	P08
CL46	9	B38	A38	C38	HD14	D26	C39	A39	P08	B37
CL47	9	B39	C40	A40	A39	C39	C32	D31	D08	B40
CL48	9	B40	D32	C36	A36	A40	C40	C06	D05	D11
CL49	9	P09	A41	A42	A43	A44	A45	B45	B41	B44
CL50	9	B41	D33	D39	C42	A42	A41	C41	C20	D16
CL51	9	B42	C42	C49	D34	HD17	C43	A43	A42	P09
CL52	9	B43	A43	C43	HD16	D30	C44	A44	P09	B42
CL53	9	B44	C45	A45	A44	C44	C37	D35	D12	B45
CL54	9	B45	D36	C41	A41	A45	C45	C11	D09	D15
CL55	9	P10	A46	A47	A48	A49	A50	B50	B46	B49
CL56	9	B46	D37	D23	C47	A47	A46	C46	C25	D20
CL57	9	B47	C47	C29	D38	HD19	C48	A48	A47	P10
CL58	9	B48	A48	C48	HD18	D34	C49	A49	P10	B47
CL59	9	B49	C50	A50	A49	C49	C42	D39	D16	B50
CL60	9	B50	D40	C46	A46	A50	C50	C16	D13	D19

Table 7.2: The rest of the sixty clusters. They were designed such that each module is shared at most by three overlapping clusters.

Supercluster	#	1	2	3	4	5	6
SC01	6	CL01	CL02	CL03	CL04	CL05	CL06
SC02	6	CL07	CL08	CL09	CL10	CL11	CL12
SC03	6	CL13	CL14	CL15	CL16	CL17	CL18
SC04	6	CL19	CL20	CL21	CL22	CL23	CL24
SC05	6	CL25	CL26	CL27	CL28	CL29	CL30
SC06	6	CL31	CL32	CL33	CL34	CL35	CL36
SC07	6	CL37	CL38	CL39	CL40	CL41	CL42
SC08	6	CL43	CL44	CL45	CL46	CL47	CL48
SC09	6	CL49	CL50	CL51	CL52	CL53	CL54
SC10	6	CL55	CL56	Cl57	CL58	CL59	CL60

Table 7.3: The definition of the superclusters as the "OR" of clusters named CL01 through CL60. Therefore, a supercluster fires if at least one of its cluster fires. A cluster fires if the summed energy of its modules is greater the threshold.

the six clusters throughout the entire calorimeter. The six clusters around a pentagon and the associated hexagon B's form a supercluster. Therefore, there are ten such superclusters in the calorimeter and in the trigger, a supercluster is the "OR" of six clusters. Some clusters and a supercluster are shown in figure 7.10 together with the energy distribution within the calorimeter of one pion beta decay event. The clustering scheme as it translates into the pion beta trigger electronics is illustrated in figure 7.11.

The $\pi\beta$ trigger requires the coincidence of two showers within 20 ns inside a valid DPG; each shower energy must exceed the threshold and they must occur in two diametrically opposed superclusters. Beside the 4-fold Michel accidental coincidences, the only competing π^+ decay channel in this trigger is $\pi^+ \to e^+\nu_e\gamma$. However, a cut on neutrals in the plastic veto detector (see figure 5.7) will significantly reduce the $\pi^+ \to e^+\nu_e\gamma$ contribution, leaving a clean $\pi\beta$ signal. On the other hand, the $\pi^+ \to e^+\nu_e$ trigger requires the presence of a single shower, also within the DPG, occurring in only one supercluster. As a result, the $\pi^+ \to e^+\nu_e$ trigger is more susceptible to accidental coincidences of Michel events. Although the background can be cut away in an off-line analysis, the trigger must be sufficiently selective and

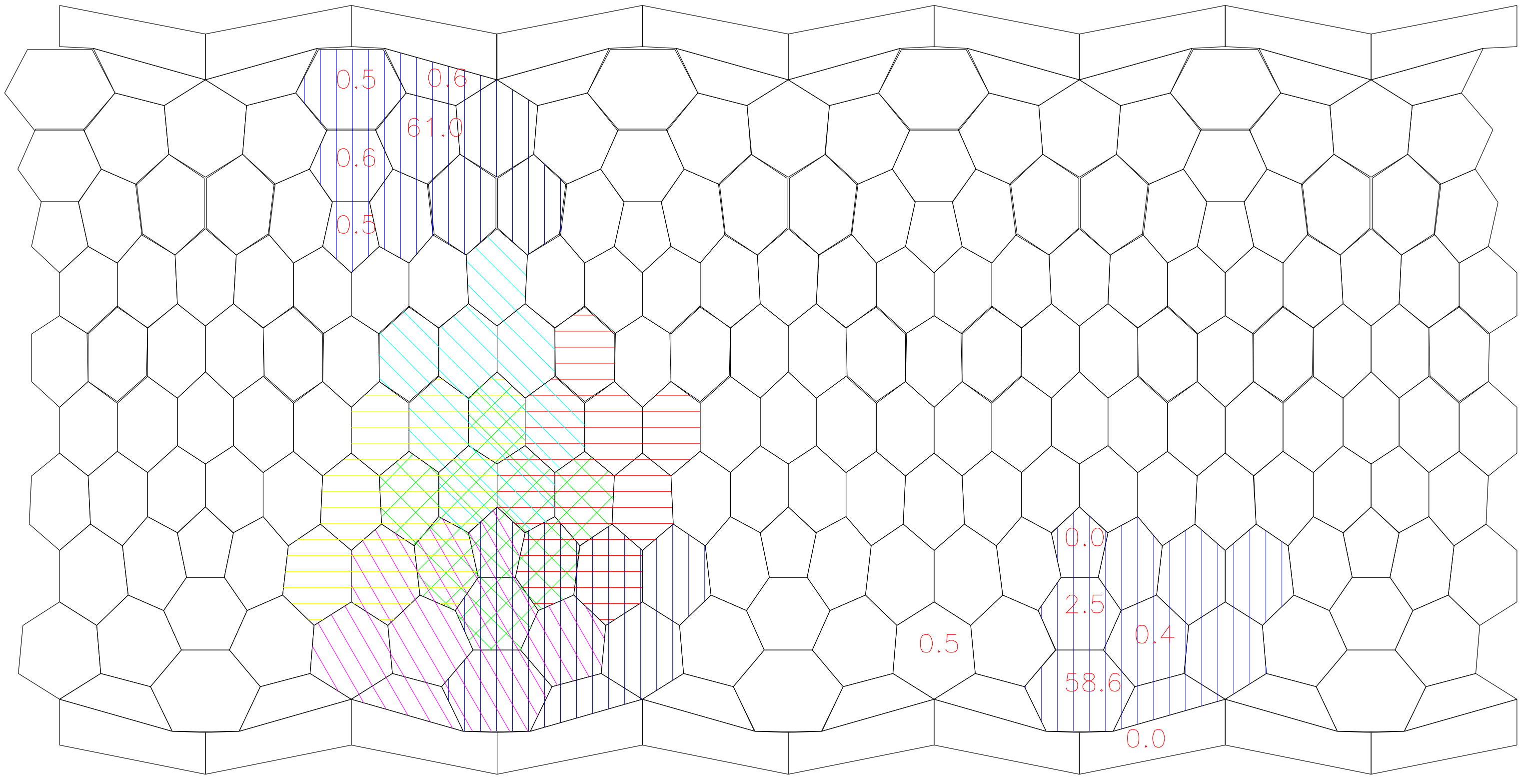

Figure 7.10: Pion beta single event display showing some clusters and one supercluster as an 'OR' of six clusters. The energy distribution (in MeV) of one pion beta event event is also shown. This event will fire the trigger since each of two diametrically opposed clusters receive more than the threshold energy (50 MeV in this case).

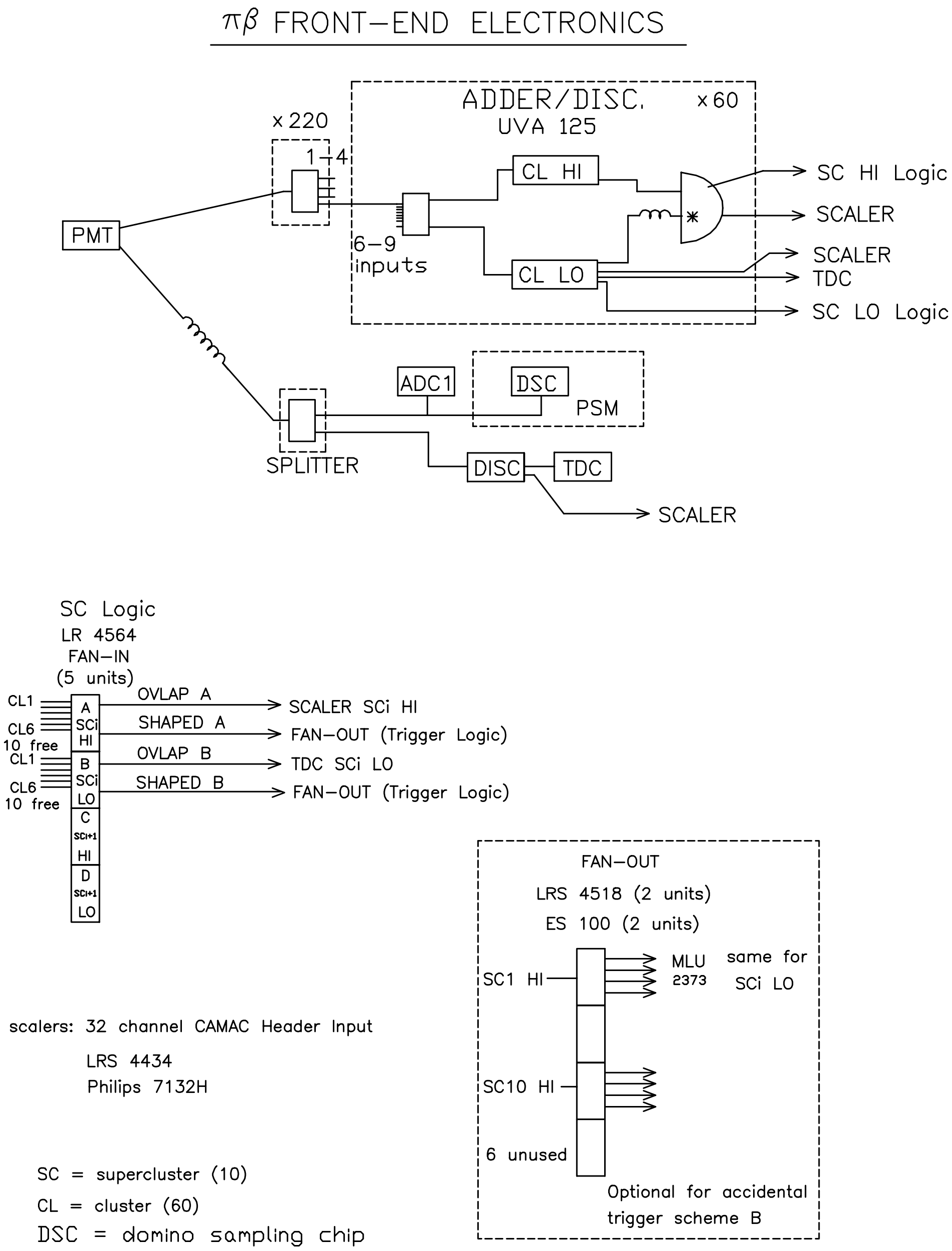

Figure 7.11: The clustering method in the front-end electronics. Two identical signals are extracted from the PMT. One of the signal goes to the cluster electronics where it may be split up to four times. The clusters are formed at the ADDER which produces a high and low discrimination outputs. The outputs are then sent to the supercluster electronics.

free of bias. For that reason, a fast pile-up rejection circuit will be implemented as well as a software pretrigger involving MWPC information. One can also reduce the cluster size from 9 to 3 to enhance the selectivity of single-arm events. In addition to the two triggers described above, there will be a cosmic ray trigger, a more delayed pion gate (DPG') trigger and on-line energy calibration procedure: in the absence of beam, a laser light will be distributed periodically to all detector modules, providing an on-line energy calibration for the entire detector system. The realization of the various event triggers are shown in figure 7.12.

7.5 Nomenclature

The calorimeter modules are assigned serial numbers S001 through S240: the pentagons carry the serial numbers S001 through S010, the hexagon A's S011 through S060. The vetoes receive the last twenty numbers S221 through S240. The numbers used in describing the clusters and the superclusters relate to the actual positions of the modules in the calorimeter while the serial numbers describe the properties of the crystals such as the shape, the fast to total, the dimensional accuracy, the light collection uniformity. However, once the calorimeter is assembled only the serial numbers will prevail since at that time the actual position of, say, S001 will be determined: S001, a pentagon whose properties are well documented, could conceivably take any of the positions P01 through P10 shown in figure 6.4.

7.6 Quality of the Crystals

Upon delivery, the crystals have been subjected to the following tests which they must pass to be selected for the assembly of the calorimeter:

7.6.1 Fast to Total Ratio

It is the first test to which all delivered modules are subjected. The bare module is air gap coupled to a PMT—EMI 9822QB. The cosmic rays traversing the crystal produce signals whose charges are integrated during the fast gate (100 ns) and the long (total) gate: 1000 ns. The ratio of the charge collected during the fast gate

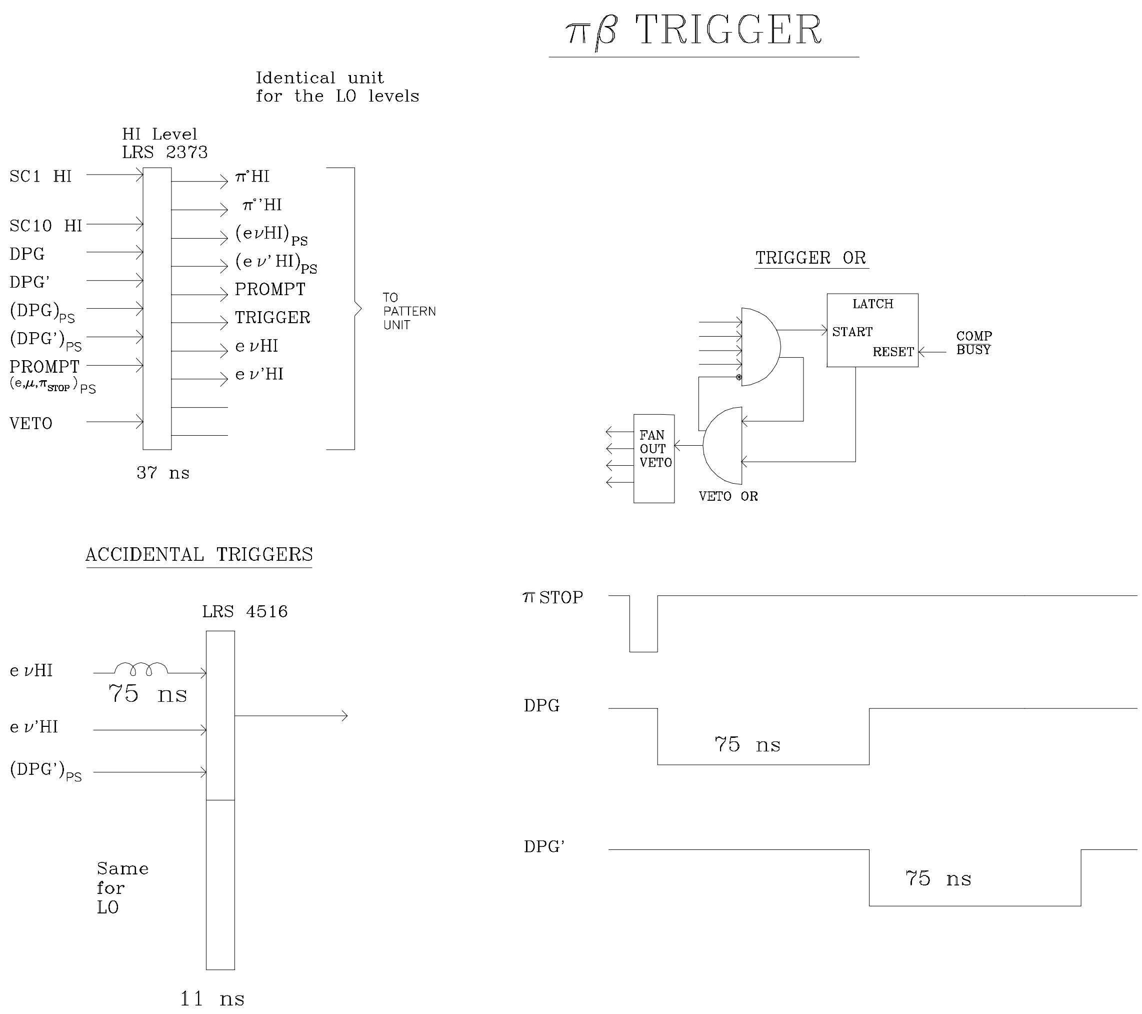

Figure 7.12: The electronic diagram for the pion beta trigger. The Memory Look Up (MLU) makes boolean operations on the inputs which include the supercluster signals, the DPG, etc. As outputs, the MLU produces the desired event triggers which are stored in pattern registers. The Data trigger is the "OR" of the various event triggers.

to that measured in the long gate gives the F/T of that particular crystal. The F/T is an important measurement of the quality of the CsI ingot from which the module was cut. The length of the fast gate is also the nominal length of the delayed pion gate (DPG) during which pion beta and $\pi^+ \rightarrow e^+\nu_e$ events are registered. For good energy resolution in the calorimeter, the F/T for each module must be 70% or better.

7.6.2 Dimensional Tolerances

The importance of this test rests on the fact that the dimensions of the fabricated modules must be within some tolerances (vertex coordinates: $\pm 300\mu$m, neighbor side angles: $\pm 0.25°$, and opposite side angles: $\pm 0.08°$) of theoretical dimensions — these dimensions are given in the tables and figures of section 5.4 — to successfully put together the calorimeter. Therefore, the dimensions of the delivered crystals are examined using a 3-dimensional measuring device. The device is computer controlled and automatically scans the surfaces, picking six points on each of the surfaces of the crystal whose dimensions are being checked. The selected points are fitted with planes, and the coordinates of the vertices follow as intersections of planes. The absolute precision of the device is 7μm with a reproducibility of 20μm.

7.6.3 Light Collection Uniformity

The proper surface treatment of the each of the modules as it affects the light output and the light collection uniformity along the longitudinal axis of the crystal has been investigated. Different wrapping materials have been tested for maximum light output and minimum non-uniformity. One of the crystals has been studied in beam and with cosmic rays using the various surface treatments. These studies have resulted in a convergence upon the following wrapping method: three layers of teflon (40μm thick) plus one layer of aluminized mylar (20μm) on the lateral surface with back paper on the front face. Prior to the wrapping, each crystal is polished using a mixture of 0.2μm aluminium oxide power and ethylene glycol. However, other surface treatments are currently under investigation. In addition, a cosmic ray tomography system has been designed to measure the light collection non-uniformity throughout the entire volume of each module. In particular, this method will reveal the regions of impurities and imperfections where the scintillation light is absorbed. For each of the crystals which eventually will make up the calorimeter, the non-uniformity must be $\leq 3\%$. Once the crystals have been tested for F/T and their dimensions checked, they are wrapped as described above and passed on to the tomography system. The description of the tomography apparatus and some of its results will be presented in a subsequent chapter.

7.7 Summary

Up to this point, the pion beta experiment has been introduced from the motivation to the experimental apparatus and approach. The design of some of the salient components like the calorimeter has been given particular attention. Other components including the support structure and the read out electronics do deserve more involved description in their own right. However, it has been the goal to provide a basic overview of the experiment with the emphasis on the design of the active target and the calorimeter. As shown in chapters 5-7, the conceptual framework of the pion beta decay experiment is being realized in the fabrication, construction, set-up and tests of the various components. The next chapter deals with the development tests, whose results provided insights into the optimization of the design, and boosted confidence in the experiment technique thus far developed.

Chapter 8

Performance and Calibration

Beside the development run undertaken in the fall of 1989, other research and development tests have been conducted with beam in the summers of 1992, 1993 and 1994. The aim of these tests has been the understanding of the beam, the optimization of the design of the apparatus, the study of the surface treatments of the calorimeter modules for minimal non-uniformity and highest light output, and the performance of the calorimeter and the active target. Other tests are being conducted with cosmic rays, such as the three-dimensional cosmic ray tomography of the modules and the measurement of the fast component over the total component of the scintillation light of CsI. Some tests required no source at all. These include the dimension measurements, the gluing of the PMT's to the back faces of the modules to ensure easy removal if need be. The test of 1989 and its significance have been presented in the chapter 6 and will not be discussed any further. Moreover, the beam studies done in 1992 and 1993 have been presented in chapter 3 in conjunction with the description of the beam channel. In this chapter, the development runs of 1993 and 1994 are described. The significance of the results of these tests are discussed in terms of the performance of the apparatus. In addition, the cosmic ray tomography set-up is introduced and some of its results presented.

8.1 Performance of the Active Target

The version of the active target used during during the development run of 1993 consisted of 140 plastic scintillator fibers of $2 \times 2\,\mathrm{mm}^2$ cross section each and 7 cm long. The fibers were isolated from each other with an acrylic cladding and held together with epoxy. Only 35 of the fibers were coupled to 1-inch PMT's via fiber optic light guides. All the other fibers were viewed by a single 2-inch PMT. The size of the beam at the center of the active target was certainly bigger than the cross-sectional area of the thirty-five fibers. For this reason, the lateral stopping distributions were measured in a series of runs during which the target was translated perpendicularly to the beam by known amounts — the translations were in steps of 10 mm to either beam up, down, right or left — relative to central trajectory of the beam. The set-up of the apparatus was similar to that shown in figure 3.6 with these modifications: the two MWPC's and the scintillator counter S1 were removed. The active target was positioned such that its center coincided with the beam waist, i.e, the position of the first MWPC in figure 3.6. An active degrader (S1) of 3 cm thick was placed immediately in front of the target such the beam pions with 116 MeV/c central momentum, stopped within the central region of the target. The pions with a mean range of 6.64 cm in plastic scintillator, traversed a 4 mm carbon degrader ($\equiv$ 7 mm of plastic scintillator) in the beam channel, the scintillator counter S0 (1.2 mm), the vacuum window ($\equiv$ 0.3 mm), the active degrader (plastic scintillator 3 cm thick) and air ($\equiv$ 1 mm). At their entrance to the active target, the residual energy and range of the pions were 24.7 MeV and 2.67 cm respectively. A cross-section of the thirty-five fibers is shown in figure 8.1. The trigger was $\mathrm{S0} \cdot \mathrm{S1} \cdot \mathrm{RF}$ (see figure 3.3) and the trigger rate was $\sim 5.00 \times 10^4\,\mathrm{s}^{-1}$ for a typical low intensity run. The average stopping rate in a fiber was $\sim 1.96 \times 10^3\,\mathrm{s}^{-1}$. The equalization of the PMT gains was done on the oscilloscope by comparing the $\pi^+ \rightarrow \mu^+\nu_\mu$ line (4.2 MeV) in each of the fibers. The light collection in the target was also determined in a similar fashion, i.e., from a comparison between the muon and the single photoelectron signals for each fiber. The number of photo-electrons per MeV deposited in a fiber varied between eight and fifteen. For each fiber, a TDC, ADC and scaler information were read out. Knowing the coordinates $X(i)$, $Y(i)$ of the centers of the fibers and their energies $ADC(i)$, the horizontal and vertical stopping distributions (X, Y) were obtained as the weighted means:

$$X = \frac{\sum_{i=1}^{35} X(i) * (ADC(i) - PED(i))}{\sum_{i=1}^{35}(ADC(i) - PED(i))}, \tag{8.1}$$

$$Y = \frac{\sum_{i=1}^{35} Y(i) * (ADC(i) - PED(i))}{\sum_{i=1}^{35}(ADC(i) - PED(i))}; \tag{8.2}$$

where $PED(i)$ are the pedestals in the ADC's. Pedestal runs were recorded periodically during the data taking process. The drifts in the pedestals had FWHM's of ~ 30 ADC channels which translate to an uncertainty of 0.26 MeV in the determination of most probable energy deposition. The analysis showed that the number of stopped pions scaled with the area defined by twenty-five, nine and four fibers: groups of twenty-five, nine and four fibers were considered as shown in figure 8.1. There is only one combination of twenty-five fibers. All the possible combinations

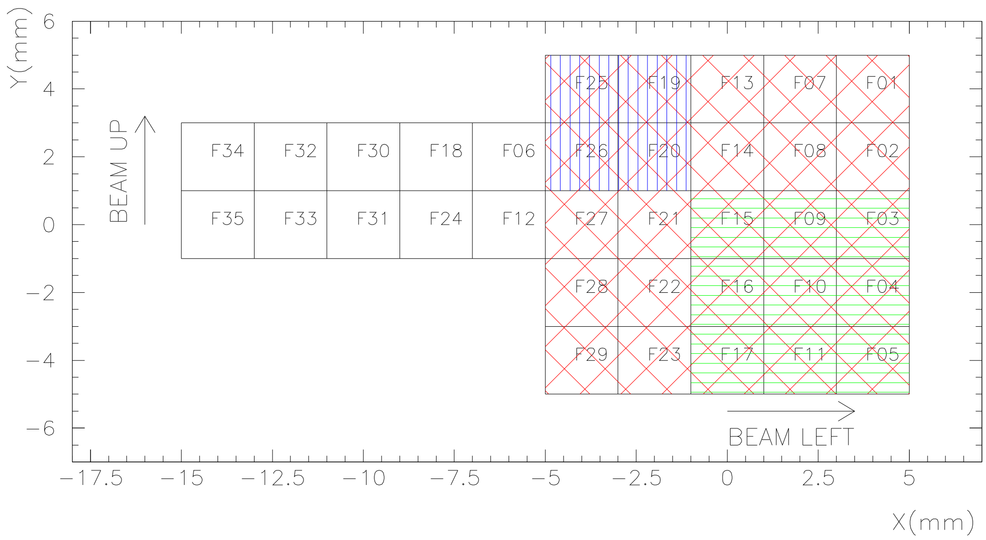

Figure 8.1: A cross section of the thirty-five plastic scintillator fibers used to measure the lateral stopping distributions during the test of 1993. When the target was centered on the beam line, the central trajectory of the beam passed through the center of fiber F15. Twenty-five fibers are shown in red, one combination of nine fibers is in green, and a combination of four in blue.

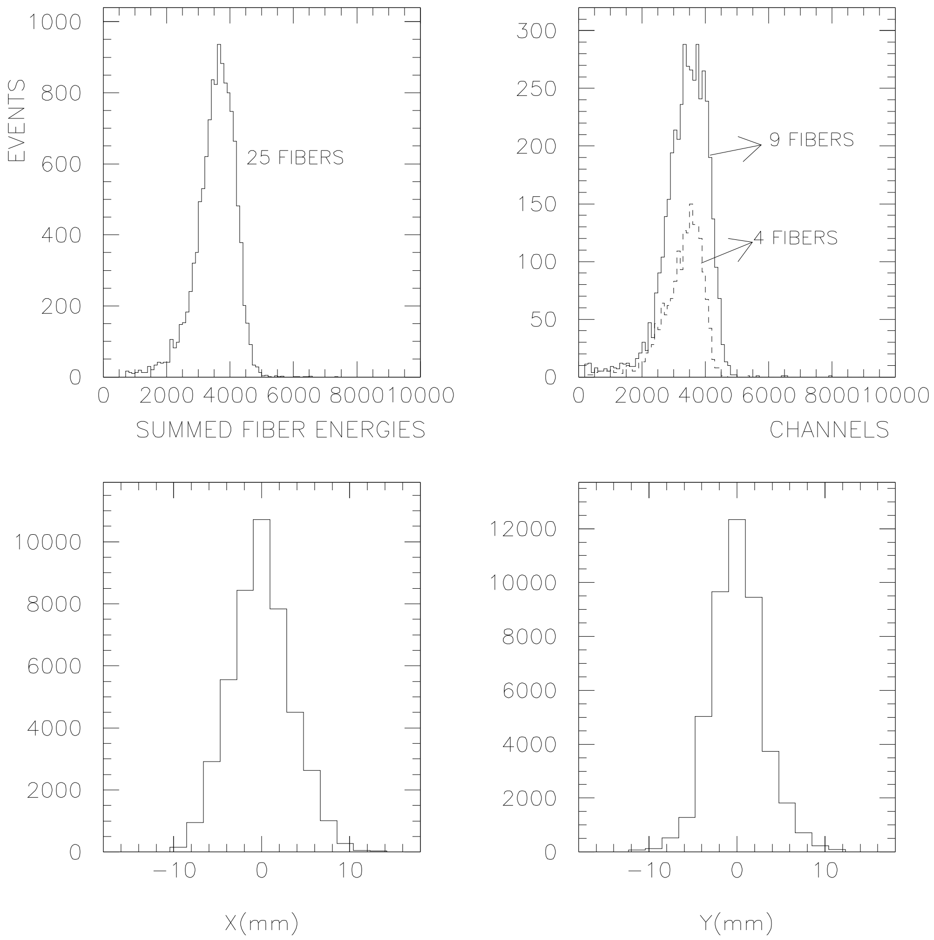

Figure 8.2: The top two figures shown the energy distributions of the stopped pions within the volume of twenty-five, nine and four fibers. The integrated contents of the histograms scale with the corresponding areas. All possible combinations of nine and four fibers were examined and consistent results were obtained. The bottom two figures are the horizontal and vertical stopping distributions measured with the active target. These results led to the redesign of the target.

of nine and four fibers were examined in detail. It was observed that the number of pions stopped within the volumes of twenty-five, nine and four fibers scaled with the corresponding cross sectional areas. However, a subgroup of less than four fibers did not exhibit this scaling feature which suggested that the beam pions stopped within the fiducial volume defined by four fibers. This enabled the redesign of the target with $3 \times 3\,\mathrm{mm}^2$ fibers instead of $2 \times 2\,\mathrm{mm}^2$. As shown in figure 8.2, almost all of the beam pions stopped within a spot of 28 mm diameter. This observation dictated the size of the new active target described in section 5.1. The on-line analysis showed that the cross talk between fibers was less than 10%. The only other modification after the test of 1993 was that the active length of the fibers were reduced from 7 to 5 cm. The newly redesigned active target was fabricated at the University of Virginia (just like the previous one) and taken to the beam in 1994. Its performance is presented below.

The target used during the test of 1994 is the one described in section 5.1. Unlike the active target used during the test of 1993, all the seventy-seven elements of this target were each viewed by a one-inch PMT. Therefore the effective area of the target was big enough to accept the entire beam. As a result, there was no need to translate the active target with respect to the central trajectory of beam in order to measure the stopping distributions in a series of runs as was done in 1993. The beam line itself had been somewhat modified to accommodate the demands of the new development run: the beam waist had been changed from 60 cm as measured from the quadrupole triplet (see figure 3.6) to 120 cm to make enough space for the concrete shielding, the bigger CsI detector array, and other detectors to be later installed during the run. An active degrader (S1) was positioned in front of the target, and the pions of 116 MeV/c stopped in the central region of the active target which was set-up in the beam line such that its center coincided with the beam waist. The arrangement of the target with respect to the beam is shown in figure 8.3.

The data trigger was defined by the coincidence $\mathrm{S0} \cdot \mathrm{S1}$ which defined the beam particles and was timed to select pions. The trigger rate was $\sim 4.0 \times 10^5\,\mathrm{s}^{-1}$ for an average proton current of $795\,\mu\mathrm{A}$. The average stopping rate in a central fiber was $\sim$

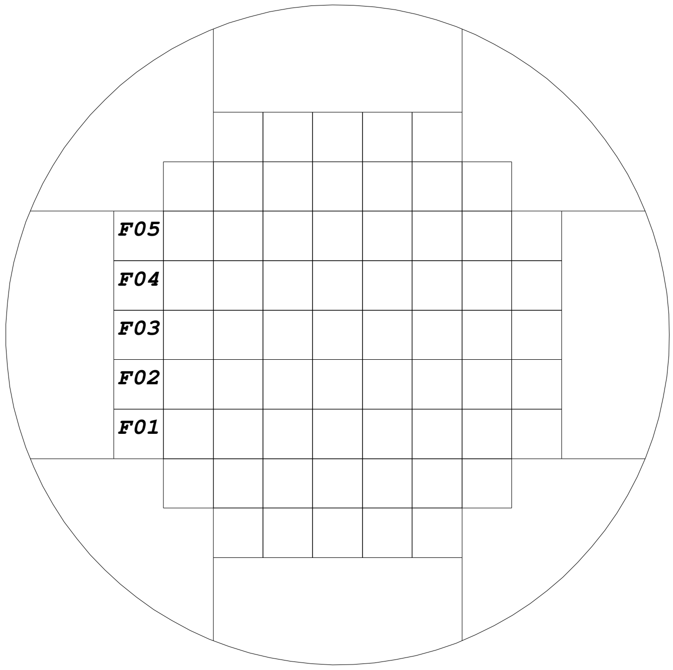

Figure 8.3: The active target and its orientation during the test run of 1994. The plastic scintillator fibers, their fiber optic light guides and PMT's were enclosed in a box for light proofing. For the same reason, face of the target where the beam entered was protected with a very thin black paper enclosure. The central trajectory of the beam was about 150.5 cm above the floor. The target was therefore placed on an adjustable platform such that the central trajectory of the beam passed through the center of fiber F35. Fine adjustments were achieved with the aid of a theodolite.

$4.8{\times}10^4$ s^{-1}. The positron and the muon contaminations in the beam were calculated using energy and time of flight cuts similar to that of figure 3.10. The gains were matched with the monoenergetic muons (4.2 MeV) from the pion decays at rest in the fibers. In this case, pedestal runs were also taken periodically; pedestal drifts of six to eight ADC channels were observed. The beam distributions were calculated

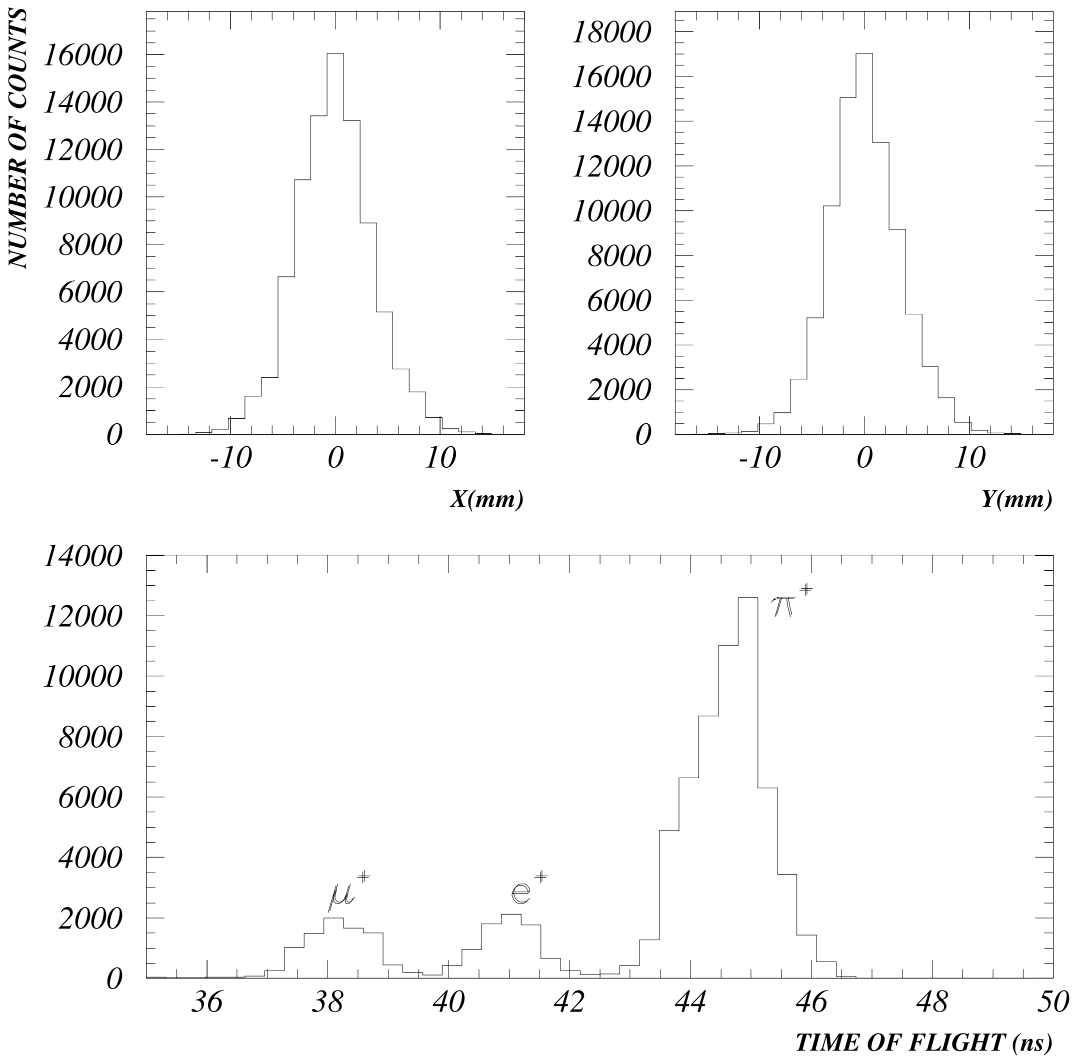

Figure 8.4: The results of the beam studies done during the test of 1994 with the active target. The top figures show the lateral beam distributions with a FWHM of $\sim 9\,$mm. The bottom portion shows the time separation between the beam pions, muons and positrons.

as the weighted means of the central fiber positions with the energy depositions in the fibers as displayed in equations 8.1-8.2. Figure 8.4 summarizes the results of the beam studies. The beam contaminations ($e^+/\pi^+ \sim 14\%$, $\mu^+/\pi^+ \sim 15\%$) are higher than the contaminations measured in 1993 (table 3.4) due to a more downstream focus. However, pulse height and time of flight cuts enabled the selection of pions with minimal contaminations from the undesired beam particles. The lateral beam distributions compare reasonably well with the previous results of 1993.

The active target provides a medium to stop the pions and to monitor the beam distributions. The target can also handle high rates, a feature which is important to the pion beta experiment. The segmentation of the active target can also be used as a tracking device for charged particles. Indeed, the decay muons of 4.2 MeV stop within few millimeters of the stopped pions. Some Michel positrons from the muon decays and the positrons from $\pi^+ \rightarrow e^+\nu_e$ have enough energy to escape the target. In the process, the escaping positron deposits energies in the fibers which lie on its path. Such an event is shown in figure 8.5.

Figure 8.5: The stopped pion decays into muon (red-green region). The muon subsequently decays into a positron with enough energy to exit from the target. The direction of the escaping positron is more or less defined by the fibers which lie on its trajectory since the positron deposits energies in those fibers. The energy scale is a continuous variation from blue (lowest energy above the noise, 20 ADC channels) to red (highest energy, more than 600 ADC channels).

8.2 Surface Treatments of the Crystals

The effects of various surface treatments on the light output and the light collection uniformity have been studied during the test of 1993 with the objective of finding the wrapping material and method which maximize the light output and at the same time minimize the light collection non-uniformity along the axis of the calorimeter modules.

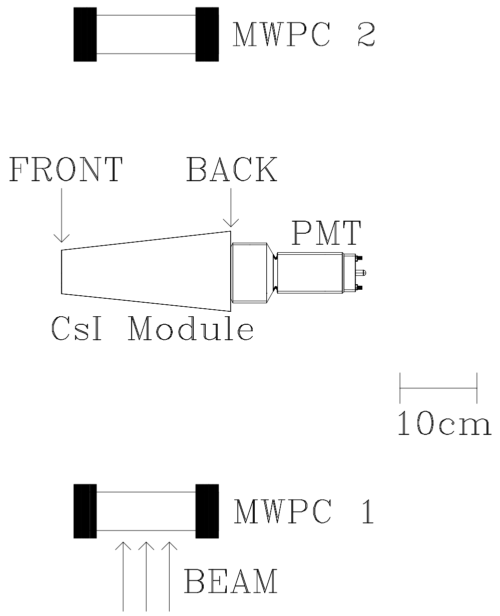

Figure 8.6: The set-up for light output and light collection uniformity tests. The wrapped CsI module was sandwiched between two MWPC's. A parallel beam of pions of 375 MeV/c traversed the first chamber, the CsI module and the second Chamber. The active areas of the chambers were not big enough to cover the entire body of the CsI crystal. As a result, for a given wrapping system, data were taken in a set of runs during which the CsI module was translated perpendicularly to the beam with the MWPC's held fixed.

During these studies one calorimeter module was used and its lateral surfaces were wrapped with different material such as teflon, aluminized mylar, etc. In addition, the front surface of the crystal was covered with black paint (100% or less), black paper or simply left naked. Different layers of wrapping were also considered. For each wrapping system, the dressed crystal was taken into the beam line, flanked by two rectangular MWPC's as illustrated in figure 8.6. The CsI crystal and the MWPC's were arranged perpendicularly to the central trajectory of the beam. A parallel beam of pions of 350 MeV/c passed through the first MWPC, traversed the calorimeter module and went through the second MWPC. The two MWPC's were the same ones used earlier during the run for the beam studies (see figure 3.6). Each of the MWPC's had an active area of $12.8 \times 12.8\,\mathrm{cm}^2$ and consisted of sixty-four vertical and sixty-four horizontal wires.

Two quantities were extracted from the hits in the MWPC's and the CsI modules: the light output of the CsI due to a beam pion which traversed the module and the path length of that pion in the CsI module. The purely geometrical effects on the light collection non-uniformity as a result of the tapered pyramidal shapes of the module were eliminated by taking the ratio of the light output to the pathlength. The light output was given by the ADC read out while the pathlength was obtained as follows: The MWPC's provided two points (X_1, Y_1) and (X_2, Y_2), indicating where the π^+ entered the two chambers. Therefore, these points gave the trajectory of the beam π^+, a trajectory which necessarily passed through the CsI crystal since the module was in the trigger. The segment of this line within the CsI was the pathlength. Only the tracks with minimal divergence as a result of multiple scattering in the CsI were selected for the calculation of the pathlength which could be obtained with different methods. One method used during the on-line data taking relied on the knowledge of the tapered angles of the surfaces of entrance and exit of the π^+. During the course of the off-line analysis the pathlengths were calculated in a Fortran routine which defined the calorimeter modules as a volume bound by intersecting planes. The routine also positioned the module as it was in the beam and found the intersection points of the line defined by the hits (X_1, Y_1) and (X_2, Y_2) with the planes of entrance and exit. The distance between these intersection points was returned as the pathlength. The active length (12.8 cm) of the MWPC's could not cover the entire body of the module (22 cm). For this reason, for a given wrapping material and method, data were taken in a series of runs during which the CsI crystal was translated perpendicularly to the beam with respect to the fixed positions of the MWPC's.

Figure 8.7 shows the light output per unit pathlength along the axis of the modules for various treatments of the front face: the lateral faces were wrapped in three layers of teflon. Better uniform response and light output were achieved with the front face covered with black paper. Consequently, for the study of the responses of an array of calorimeter modules to monoenergetic positron beams, each crystal was wrapped in three layers of teflon with black paper at the front face.

Further tests regarding the surface treatment of the crystals were carried out after the run of 1993. These tests favored a wrapping method consisting of one layer of aluminized mylar in addition to the three layers of teflon on the lateral surfaces and black paper of the front faces. Furthermore, a tomography apparatus

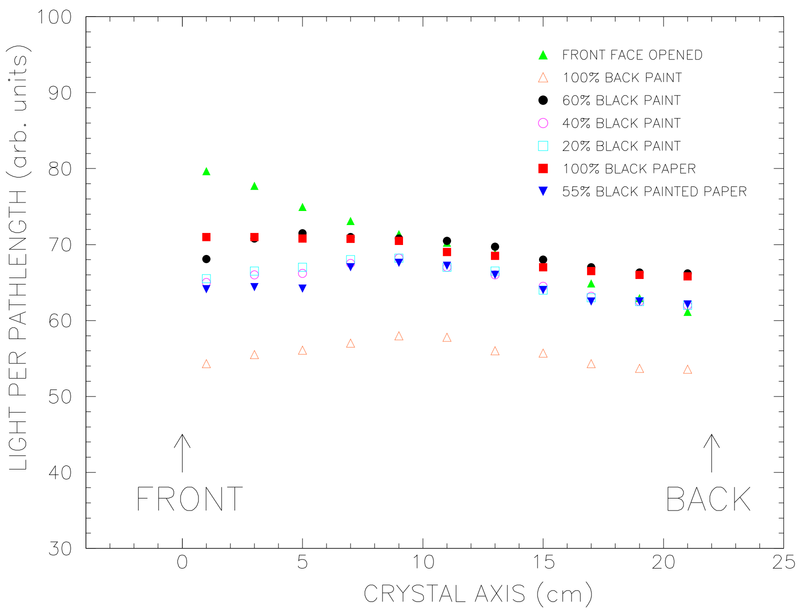

Figure 8.7: The light output per unit pathlength along the axis of the crystal for different treatments of the front face. Among all the treatments considered, black paper gave the most uniform response and the best light output. For these treatments of the front face, the lateral surfaces were covered with three layers of teflon. The result of these tests was used in the subsequent measurements of the responses of an array of twelve modules to monoenergetic beams of e^+'s.

has been set-up to examine the optical properties of each of the calorimeter modules with minimum ionizing cosmic muons. The apparatus and some of its results are presented next.

8.3 Cosmic Ray Tomography

The optical properties of a given calorimeter module are being systematically studied and must satisfy expectations before the particular module can be selected for the assembly of the calorimeter. Some of the expectations which must be met have been described and explained in section 7.6. The optical properties of interest include the attenuation length of CsI, the temperature dependence of the light output, the non-uniformity in the generation and collection of the scintillator light and the ratio of the fast to total component of the CsI light.

Forty-seven calorimeter crystals have been examined so far with the tomography apparatus which consists of a box (see figure 8.8) enclosing the modules (six at a

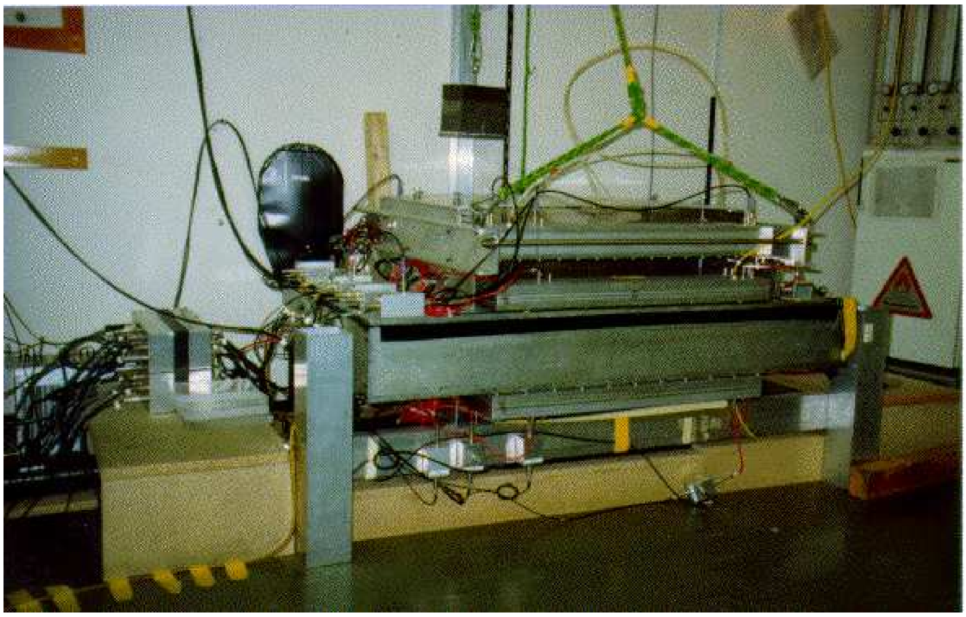

Figure 8.8: The tomography apparatus contains six crystals whose positions in the steel box are known to within 1 mm. There are two drift chambers on top, and one below the box. The active area of the chambers is $60 \times 60\,\mathrm{cm}^2$. The lead bricks and the plastic scintillator counters are hidden in this view.

time), three drift chambers (two above and one below the box), and two scintillator paddles below the bottom chamber. Lead bricks (5 cm thick) between the lower chamber and the scintillator counters allow the selection of minimum ionizing cosmic particles (with a threshold of 120 MeV) which traverse the entire detector system. The directions of the cosmic rays are extracted from the hits in the chambers. The segments of the cosmic ray paths in the CsI modules, together with the energies deposited enable the study of the properties mentioned above. In particular a reconstruction algorithm has been implemented with the objective to extract the light output throughout the entire volume of each of the crystals. This procedure reveals the regions of imperfections (if any) where the scintillating light is either absorbed or more or less produced.

8.3.1 Description of the Apparatus

Six crystals at a time can be positioned in the box after they have been carefully prepared, i.e., polished, wrapped in three layers of teflon and one layer of aluminized mylar with black paper on the front face, and PMT glued (figure 8.9). A temperature sensor is also installed in the box, and for every event during the data taking process, the temperature and the absolute time are also read out. Once the modules have been positioned, and their identities, positions and orientations recorded, the box is closed and light proof. The apparatus is operated in a climatized room with controlled humidity. The crystal PMT's and the drift chambers are then brought under their operational voltages for a day or so before the data taking. The operational voltages of the PMT's are determined by requiring that the minimum ionizing peaks fall in the same channels. For the drift chambers, positive high voltages of 2200-2400 Volts are applied to the anode wires with the cathode wires grounded. These drift chambers were built at the Los Alamos Meson Physics Facility (LAMPF) and were previously used in other experiments [Ate-81], [Mor-82], [Ran-81] and [Ran-82]. Each chamber has two signal planes and three ground planes on each side and in-between the signal planes which consist of two orthogonal sets of alternating anode and cathode wires. The anode-cathode separation is 0.4064 cm. The cathode wires are alternately attached to two bus lines, thereby making an odd (O) and an even

(E) bus lines. The anode wires are soldered onto a delay line of 2.0 ns per wire spacing, i.e., a total of 144 ns for each anode line containing 73 wires. A gas mixture of 65% argon, 35% isobutane and 0.1% isopropyl is supplied to the chambers. The gas pressure in the chambers is kept constant over time via a bubbler with 3 mm low vapor pressure oil.

The signals — from the two ends of the anode delay lines, X_P and X_N for instance — produced by a charged particle going through a chamber are sent via a splitter box (figure 8.10) to a preamplifier for double stage amplification. The signals are then fed through a DC filter to a constant fraction discriminator whose output (30 ns wide) are sent to scalers and used for TDC stops. The signals from the odd (O) and even (E) cathodes are added and subtracted electronically by a dual cathode O/E amplifier (figure 8.10) which generates two outputs: O+E and O−E. The polarity (or sign) of the O−E signal indicates the side of the anode wire on which the charged particle has passed since the closest cathode wire has the largest pulse. The offset and the gain of the O/E amplifiers are set to produce

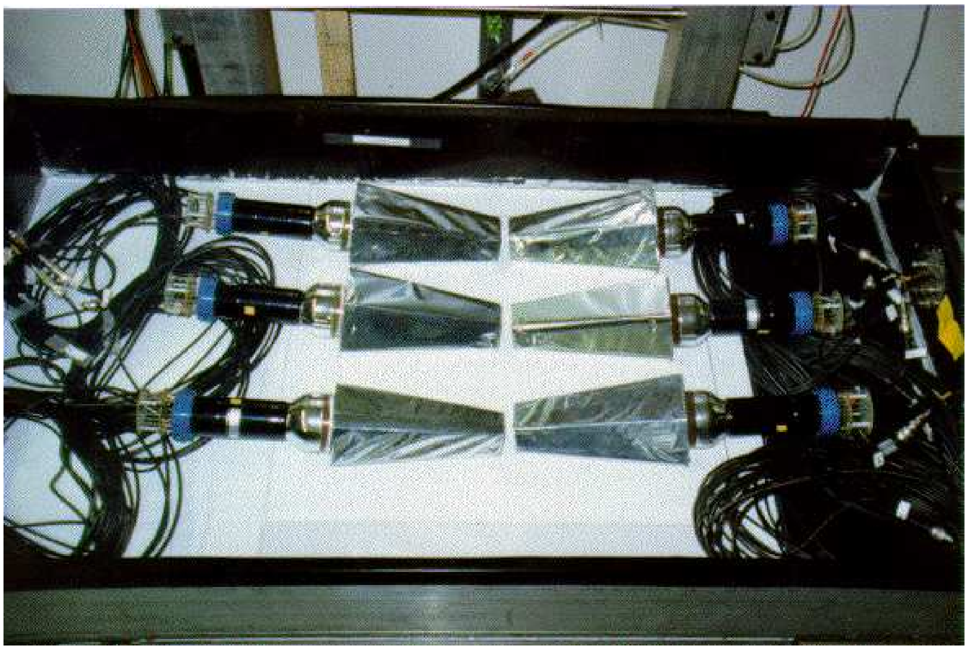

Figure 8.9: Positions of crystals in the tomography apparatus.

-0.2 Volts offset and a maximum gain of 500 mV; as a result, the most positive signals saturate at zero volt. The O$-$E signals are sent to an ADC with integration time of 100 ns. The O+E signals are fed to TDC's with the master trigger as a veto since the TDC must receive a stop only for good events. The master trigger itself is a triple coincidence between the two scintillator counters and the "OR" of the CsI modules in the box as shown in figure 8.11, or a double coincidence of the two scintillators alone, in which case the data are used for the calibration of the drift chambers.

8.3.2 Data Acquisition and Reduction

The data acquisition code used is HIX[1] (Heterogeneous Information Exchange). In this system, a front-end 486 PC is interfaced to a CAMAC crate via a HYTEC controller. The PC reads out the data and sends it over the network to a VAX server where the data are stored in a global section. A logger task passes the data to the analyzer which enables the on-line analysis and also write the data to disk and to tape. The data taking is controlled from the PC under MS Windows. Only the events with at least two good X and two good Y chambers are recorded on the tapes. A good chamber is defined as good reading of its TDC's and ADC. The trigger rate is ~ 12.7 Hz with ~ 4.4 Hz written to tapes. The filtered event rate is ~ 2.7 Hz with the CsI modules. During one week of data taking ~ 50000 raw events are collected per CsI crystal. The off-line analysis is done by packing the data in PAW Ntples. ADC pedestals, drift time-to-distance lookup tables and the calibration constants are determined for each run.

8.3.3 Calibration of the Drift Chambers

For each event, four data words per chamber are read out: the TDC's of the two ends of the anode delay lines, the TDC of the O+E signal and the O$-$E ADC. From this information, the anode wire nearest the path of the charged particle can be

[1] HIX was developed at the Paul Scherrer Institute by Dr Stefan Ritt. The HIX code has also been used during the test runs of 1992, 1993 and 1994, and is the data acquisition system for the pion beta decay experiment.

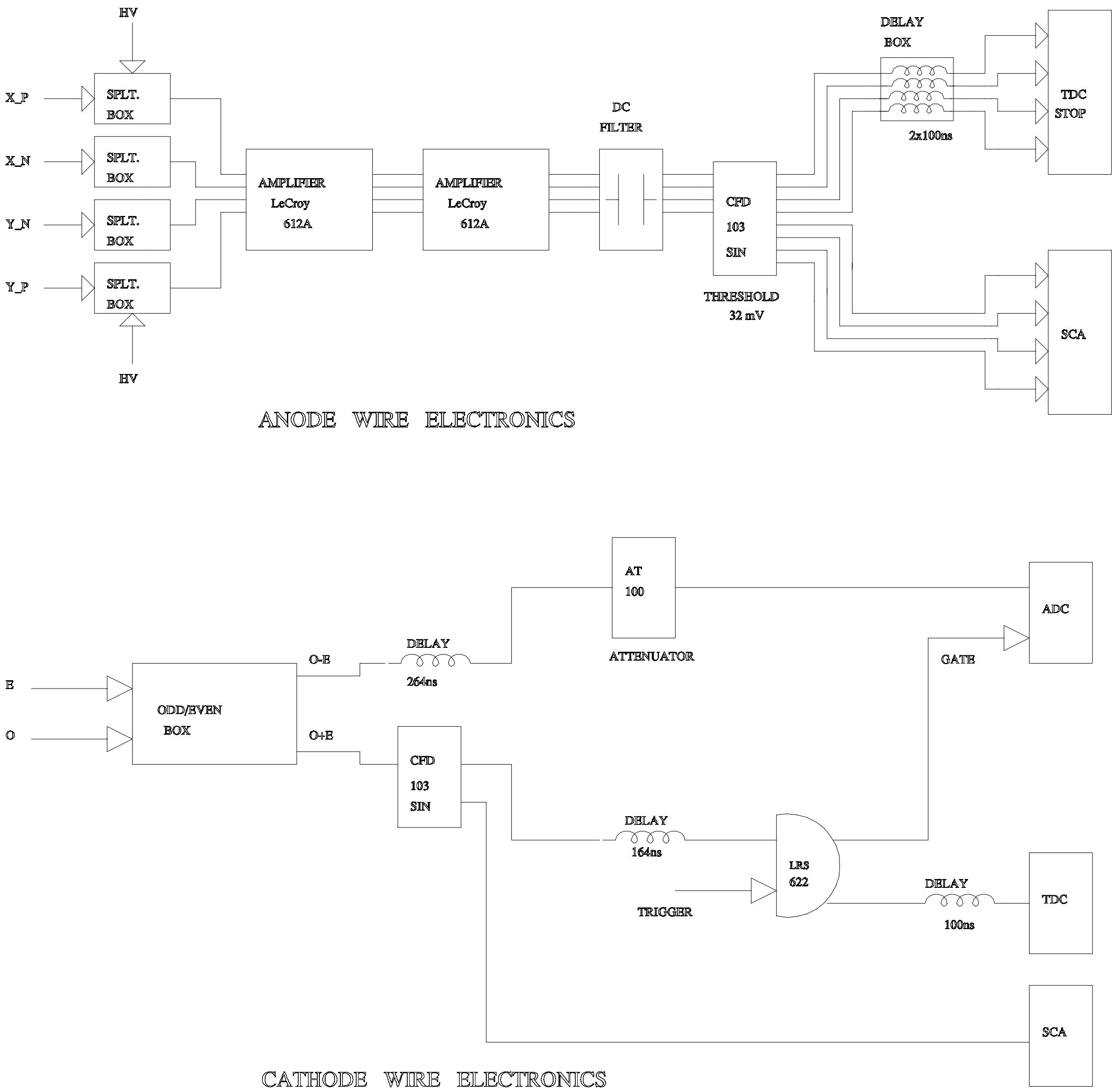

Figure 8.10: The electronic diagram of the drift chamber read out.

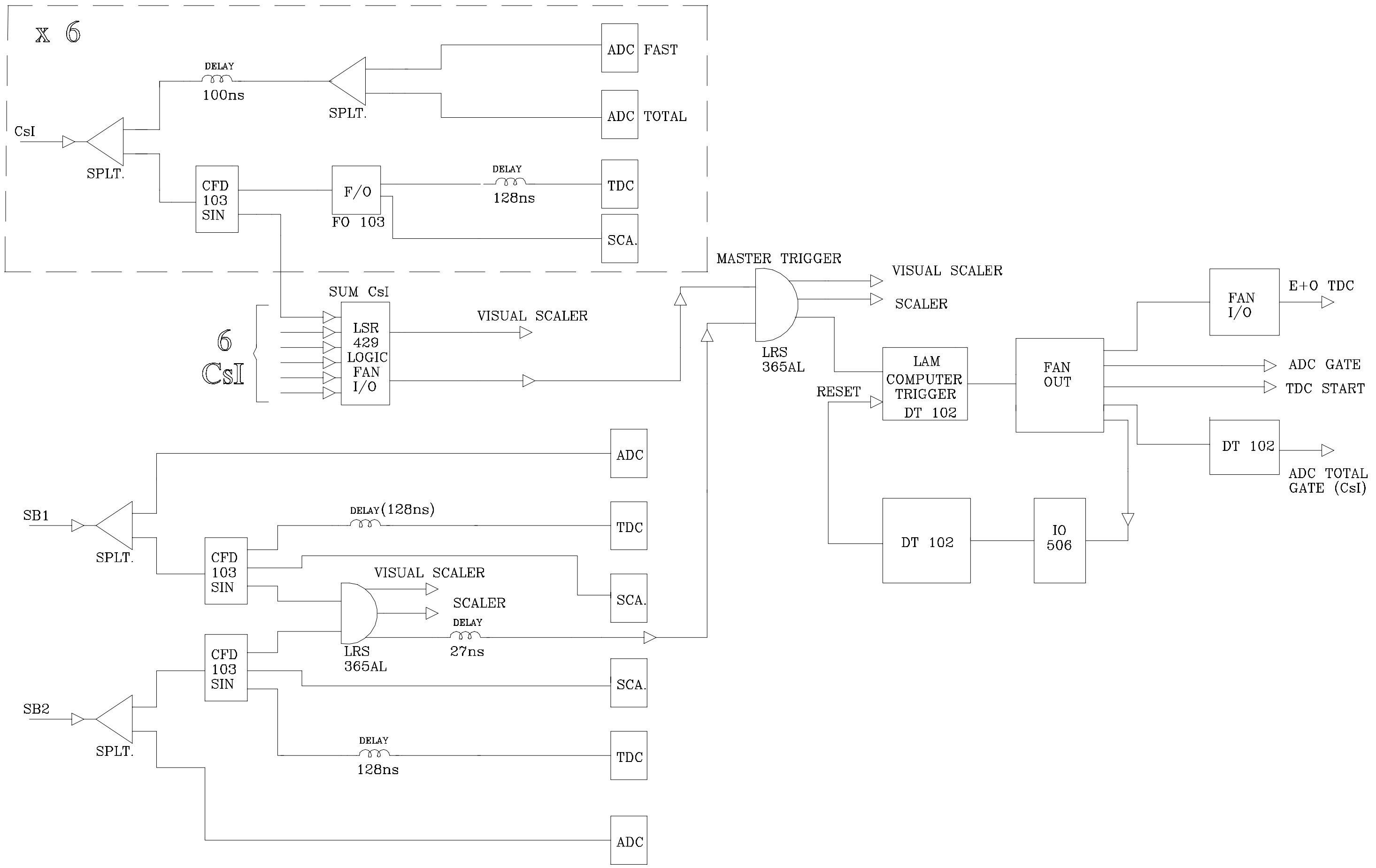

Figure 8.11: Trigger electronics for the tomography apparatus. The master trigger is the coincidence of the two scintillator counters and the "OR" of the six modules. For calibration of the drift chambers, the trigger reduces to the 2-fold coincidence of the scintillators.

determined. In addition, the distance to the nearest anode wire (the drift distance) and the side of the anode wire on which lies the particle's trajectory can be found. The anode wire number n_i is obtained from the difference in the arrival times T_1 and T_2 of the signals from the two ends of the delay lines:

$$n_i = \frac{T_1 - T_2 + N \times D}{2D}, \tag{8.3}$$

where $N = 73$ is the total number of wires and $D = 2\,\mathrm{ns}$ is the delay per wire spacing. Due to non-linear effects in the long delay lines, the corrected position of the anode wire is written as:

$$x_a = \sum_{i=0}^{m} c_i (T_1 - T_2)^i, \tag{8.4}$$

where m depends of the delay line. The coefficient c_i's are obtained by minimizing the function $(x_t - x_a)^2$. The truncated anode position x_t is a multiple of the wire spacing g:

$$x_t = g((\mathrm{integer}(x_a/g + 50.5)) - 50). \tag{8.5}$$

The drift distance d is obtained from the drift time t_d which is determined from a comparison between of arrival times (TDC's) of the anode and O+E signals with that of the trigger. Figure 8.12 shows the anode position and the drift time. The side of the anode wire on which lies the original particle's path is inferred from the O−E ADC signal also shown in figure 8.12 The ADC spectrum of the O−E signals shows two low gain peaks separated by a valley which is the divide between O>E (the left side of the anode wire) and E>O (the right side of the anode wire). The valley is therefore the origin point 0.0 for the calibration. The coordinate of the charged particle in the chamber is given as:

$$x = x_t + (-)^n (\mathrm{sign}\,\mathrm{ADC}_{\mathrm{O-E}}) d, \tag{8.6}$$

with n being the wire number. A precise and fast way to check the chamber alignment is the calculation of the residuals which are the deviations of the best straight line fit to the measured coordinates in two chambers (X_1, Y_1) and (X_3, Y_3) from the measured coordinate in the third chamber (X_2, Y_2). The spectrum of the residuals

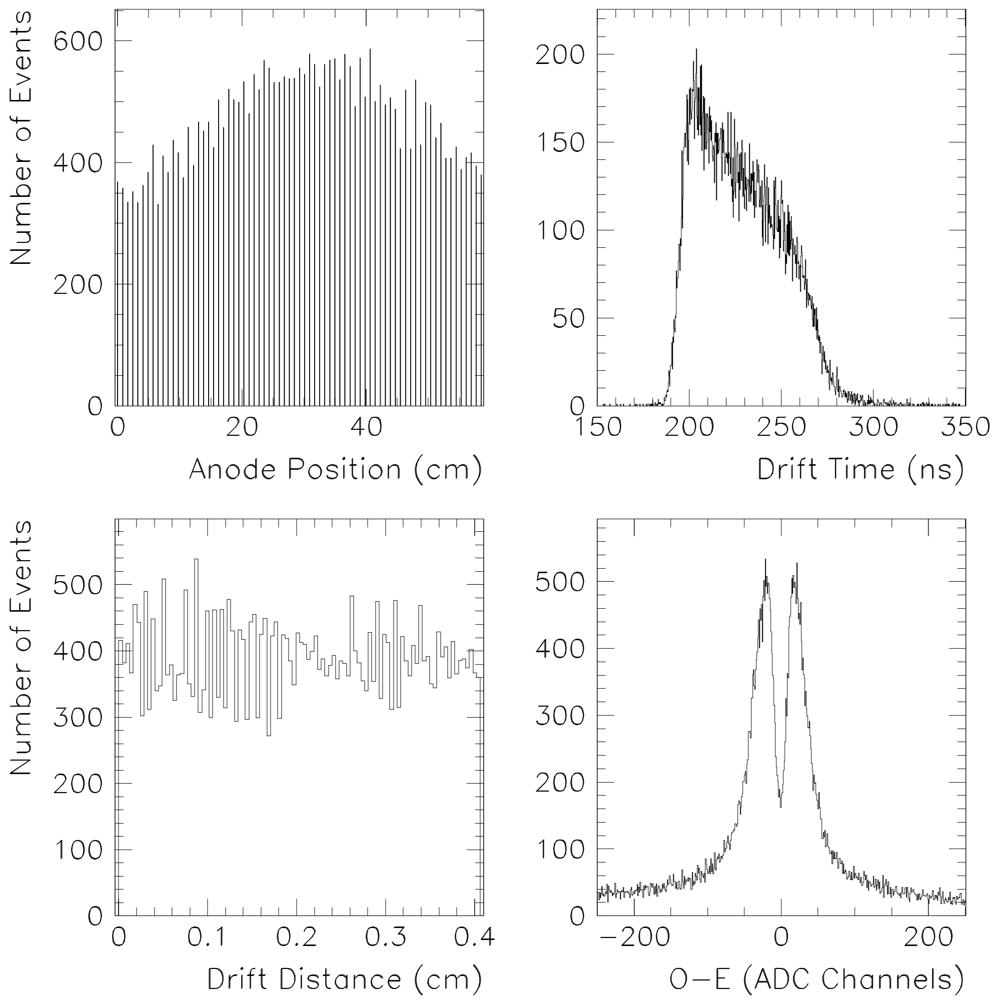

Figure 8.12: Calibration of the drift chambers. At the top left is the histogram of the positions of the anode wires. The top right shows the drift time obtained from the arrival times of the anode and O+E signals with respect to the time of the trigger. The drift distance (bottom left) is calculated from the drift times and look-up files. The left-right side identification is shown on the bottom right (O−E ADC). Because the electronics can only accept negative pulses, a gain offset is applied in the O/E amplifiers. This is compensated for in the calibration by the identification of the valley in the O−E ADC spectrum as the zero point, i.e., the divide between the left and right sides of the anode wire where the original particle's trajectory lies.

is expected to be a very sharp peak centered at channel zero as shown in figure 8.13. Once the chambers are calibrated, checks and cuts can be applied to the data to obtain a clean sample of events. The residuals and the checksums (the sums the delay line end times) provide good basis for eliminating "bad" events.

8.3.4 Reconstruction

In order to determine the non-uniformity of the CsI light throughout the volume of the modules, a reconstruction technique similar to that used in nuclear medicine imaging is needed. In the case of the pion beta tomography, the directions and the pathlengths of the cosmic muons in the CsI modules are obtained from the drift chambers. If the volume of a crystal is subdivided into elementary cells, a cosmic muon traversing the module will deposit energies in the cells which lie along the particle path. The energy deposited depends on the segments of the particle's trajectory in the cells. A geometrical algorithm has been designed to trace the particle's trajectory through the crystals, and to find the number and the actual pathlength in each of the cells traversed. However for a given cosmic ray, only the total sum of the light outputs in the cells traversed is known from the CsI ADC. The reconstruction method allows the determination of the light per pathlength in the elementary cells of the CsI module, and enables the study of the non-uniformity of the generation and collection of the CsI light in the volume of the crystals.

The principle of the reconstruction technique consists of taking initial guesses at the lights per pathlengths in the elementary cells. Then new guesses are taken based on the discrepancies between the calculated light outputs (from the previous trial) and the measured ones. An iterative process is then initiated until the process converges. Four of the existing reconstruction techniques [Bud-74] have tested for their convergences and their abilities to handle noisy data. The four methods tested are the additive and multiplicative versions of the algebraic reconstruction technique (ART), the simultaneous iterative reconstruction (SIRT) and the least-square iterative approach. These techniques have been tested with a sample of simulated data consisting of a 5% signal riding on an isotropic background. In 500 iterations, the SIRT reconstructed the data, especially the signal as a region of 4.6% intensity

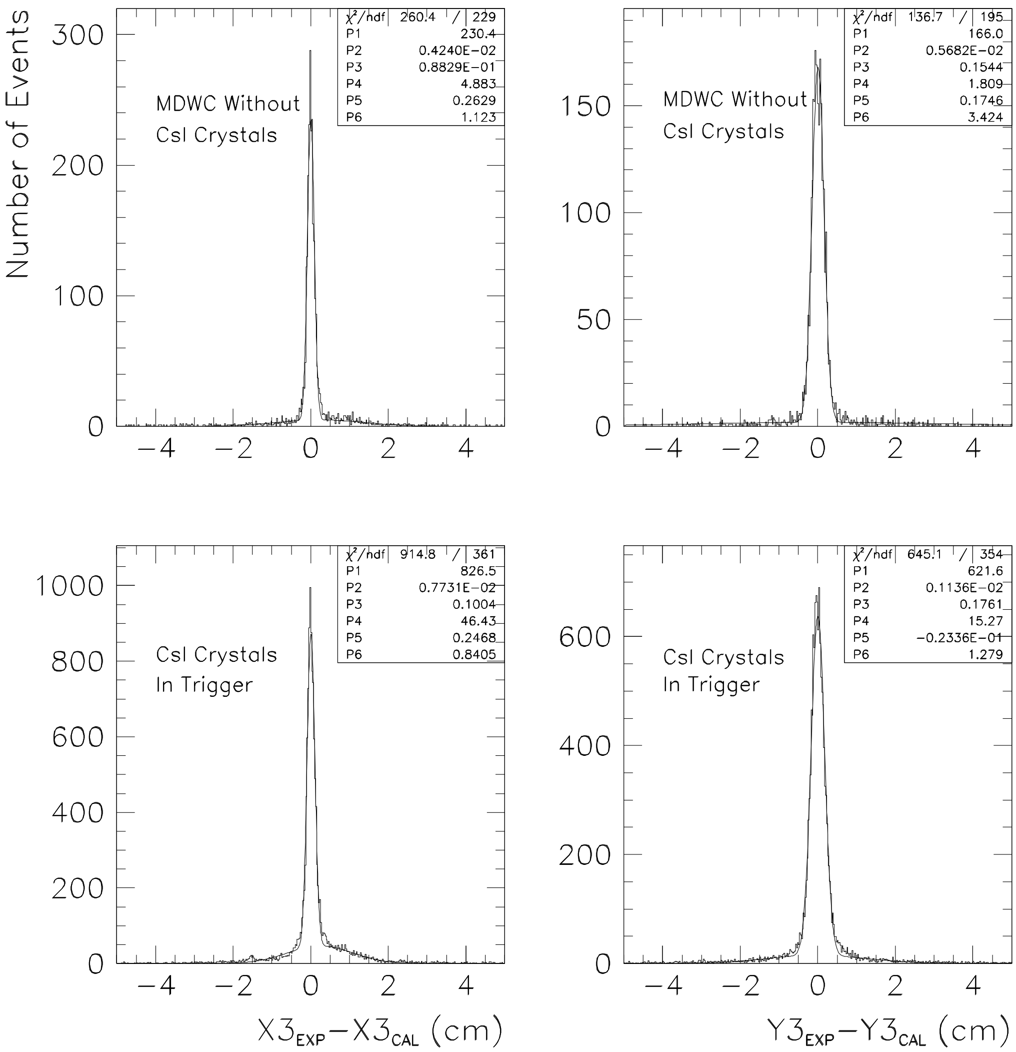

Figure 8.13: The residuals obtained as the deviations of the best line fits to the coordinates of the central and bottom chambers from the coordinates of the top chamber. The FWHM's are ~ 0.08 cm and ~ 0.18 cm for the x and y coordinates respectively. The 1.2 cm plateau contains the events with incorrect left-right identification, and/or with large scattering angles.

Crystal Shape	Crystal Serial #	$\frac{\text{Fast}}{\text{total}}$	Non-uniformity (%) σ vs 70 MeV γ	Temperature Coefficient(%)
Penta	S003	0.65	9.6 vs 2.7	-2.2
Hex A	S011	0.70	10.2 vs 3.3	-1.8
Hex A	S014	0.73	10.4 vs 4.8	-2.4
Hex C	S111	0.69	15.8 vs 4.5	-5.4
Hex C	S113	0.66	6.2 vs 2.4	-4.2
Hex D	S165	0.71	5.0 vs 1.8	-3.3

Table 8.1: Some parameters of the six crystal measured with the tomography system. The non-uniformity σ in the fourth column is affected by the light generated close to the PMT — solid angle effect. When the non-uniformity functions are weighted with the energies of the showers initiated by 70 MeV γ's incident along the crystal axes, the detector responses are more uniform. The temperature coefficients were calculated assuming a linear dependence of the light output on the temperature. For the fast and the total components, the ADC integration times were 100 ns and 1 μs respectively.

above the uniform background[2]. Some results of the reconstruction are shown in figure 8.14 for one of the modules in the box. Figure 8.15 shows the light non-uniformity along the axis of a set of six crystals in the box, and some results of the tomography are summarized in table 8.1.

In conclusion the tomography apparatus is under stable operation and a reconstruction technique has been worked out to examine each of the calorimeter modules. Up to six crystals can be inserted in the apparatus at a time. It takes about a week of data taking to collect enough statistics for one set of crystals in the box. During that period another batch of six modules are prepared and ready to be set-up for the tomography. As stated previously, tomography data have been taken for forty-seven crystals to date. The results presented here are likely to be improved upon with a refinement of the reconstruction technique and the analysis of the data. The goal is to build the calorimeter using modules with non-uniformity less than 3% (section 7.6). The crystals of that quality are being selected through the tomog-

[2]These reconstruction methods have been examined by Dr Emil Frlež who has been analyzing the tomography data. Some of his results are presented in this section.

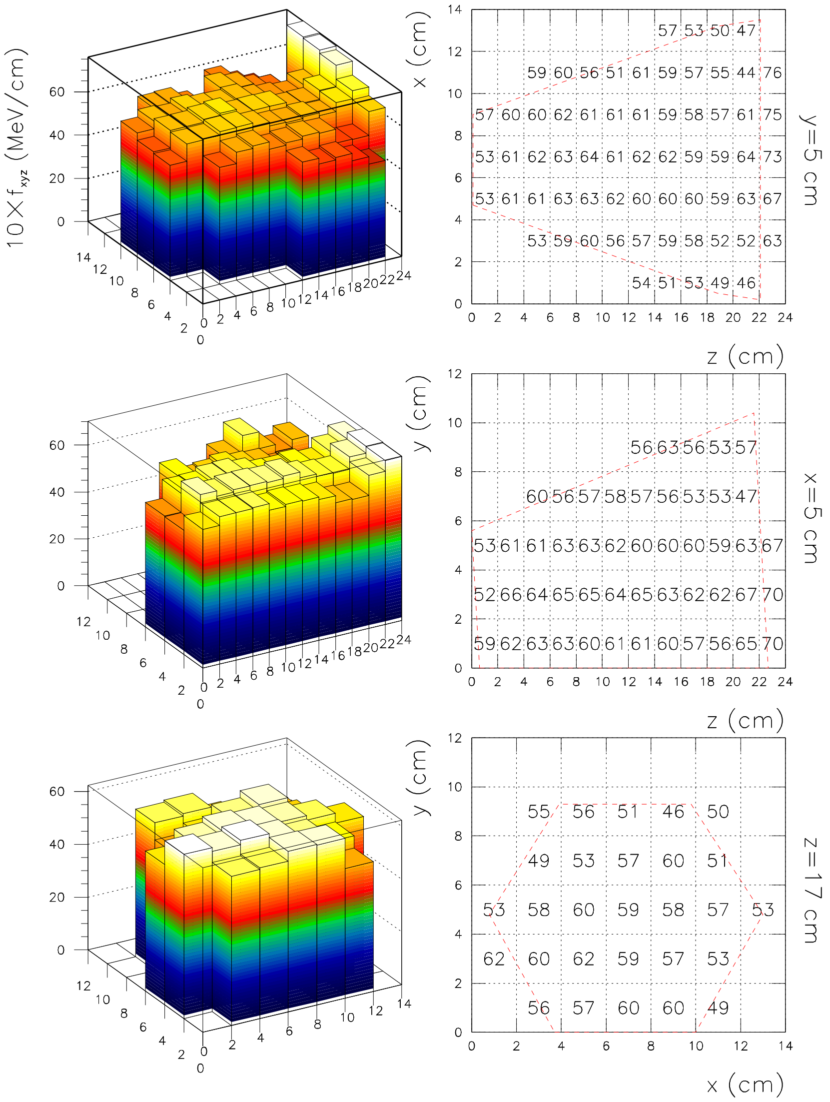

Figure 8.14: The light non-uniformity obtained from the reconstruction procedure for one CsI module (serial # S011) in the box. 28000 events with multiple scattering angles $< 3.00°$ were considered for the reconstruction. The volume of the elementary cells was $2 \times 2 \times 2\,\mathrm{cm}^3$. Three orthogonal cuts through the crystal are shown here, and the text histograms display the average light outputs (MeV) in the cells. The average energy deposited in the CsI by the cosmic muons is 10.33 MeV/cm, while the most probable energy loss is 5.92 MeV/cm.

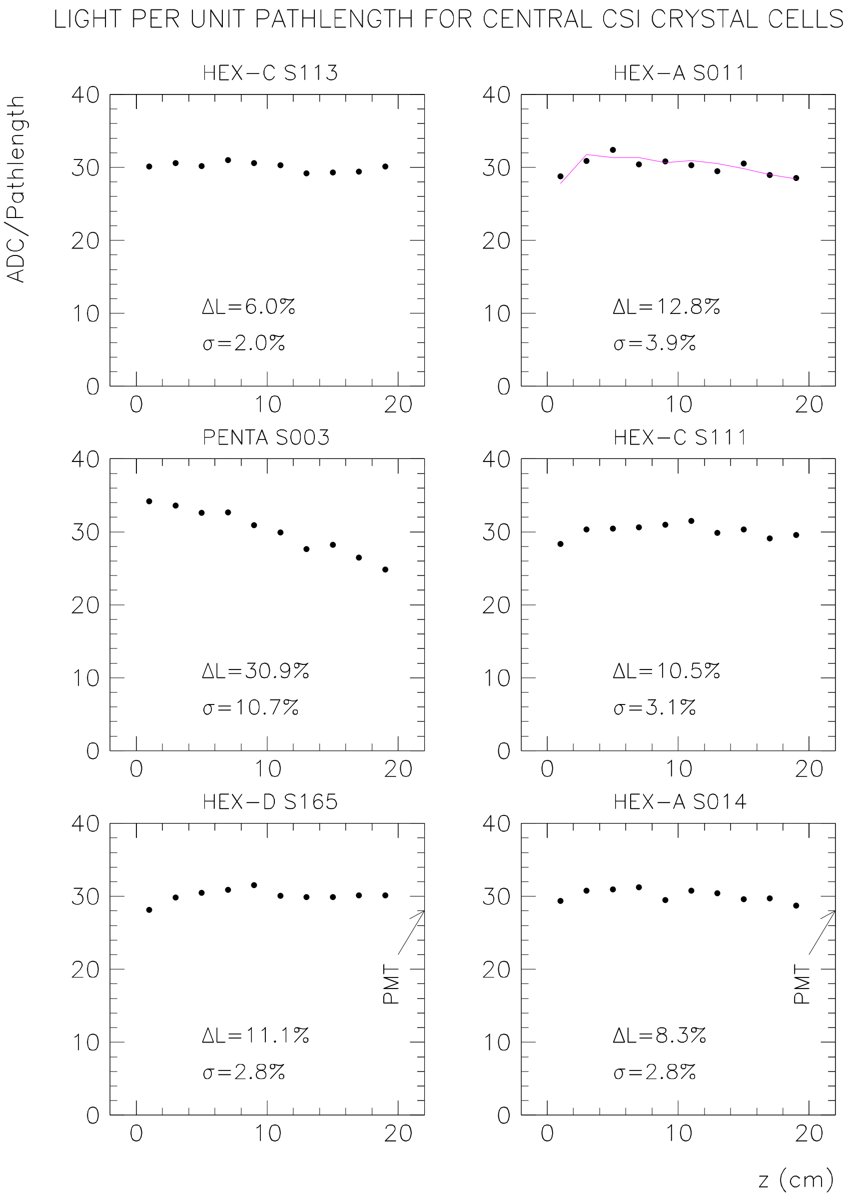

Figure 8.15: The light collection non-uniformity along the axes of six crystals measured with the tomography system. The cosmic rays with polar angles $\theta > 170°$ in axial strips of $\pm 1.5\,\mathrm{cm}$ were analyzed. The result of the reconstruction technique summed over the cells which satisfy the same cuts is shown as the dashed line for the module S011.

raphy method described here. For the responses of an array of twelve calorimeter modules to monoenergetic beam of e^+'s, a non-uniformity of 3% — this was inferred from the surface treatment studies for a wrapping method consisting of three layers of teflon and black paper at the front face (see figure 8.4) — has been used to obtain excellent agreement between data and simulation (section 8.1.3). The tomography method reveals the non-uniformity throughout the volumes of the modules, and consequently will render the simulation of the experiment even more realistic.

8.4 Calorimeter Response to e^+/e^- Beams

For the test run of 1993, twenty-five crystals were ordered from Bicron Corporation with the plan to build a sizable array with clusters and to set-up two opposite groups of modules with the objective to test the performance of a subsection of the calorimeter against monoenergetic beams of e^+'s, $\pi^+ \to e^+\nu_e$ and $\pi^+ \to \pi^0 e^+\nu_e$ decays. However, at the time of the test run, only twelve calorimeter modules were delivered. The twelve crystals consisted of one pentagon, four hexagon A's, two hexagon B's, three hexagon C's and two half-hexagon D's. They were all polished and wrapped according to the result of the surface treatment studies, i.e., three layers of teflon and black paper at the front faces. Moreover, the half-hexagon D's were each viewed by 2-inch XP2020Q PMT's with quartz window while the other crystals were each read out with 3-inch EMI 9814QB PMT's also with quartz window. The PMT's were glued to the back faces of the modules (see chapter 7) which were then arranged in the configuration shown in figure 8.16 in a box. The box which enclosed the array, was later positioned onto the beam line such that defocused parallel beams of positrons of 10, 20, 30, 50 and 70 MeV/c were incident on the array at the front faces. The side of the box that the beam traversed before striking the front faces of the array, was made of a thin black paper in order to minimize energy losses and multiple scatterings and consequently the beam divergences. The support system of the array and part of the box are displayed in figures 8.17 and 8.18. The beam line arrangement was that of figure 3.6 except for the following: one of the MWPC's and the counter S1 were removed. The side of the box which directly faced the

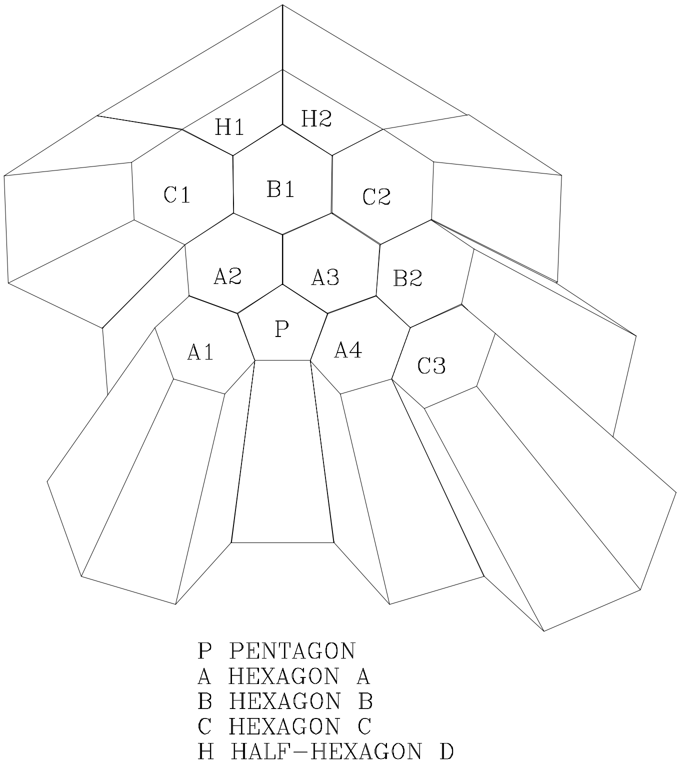

Figure 8.16: The configuration of the twelve modules used during the test run. The array was supported on the sides and the bottom by wooden plates and modules, and sealed up in a dark box to be light proof.

beam was 85 cm away from the last the quadrupole triplet. The box was first set up such that the central trajectory of the beam passed through the common edge of B1, A2 and A3 (see figure 8.16). However, because the size of the beam was not big enough to cover the entire front faces of the crystals, different runs were performed with the box rotated or translated with respected to its original position. One of the MWPC's shown in figure 3.6 was placed right in the front of the box for cuts on the regions of the front faces irradiated by the beam. The event trigger was simply the scintillator S0 in coincidence with the "OR" of the modules, i.e., $S0 \cdot \sum_{i=1}^{12}$ CsI, with $\sum_{i=1}^{12}$ CsI determining the timing. The gain matching procedure was performed on-line and off-line with the 10 MeV/c data since at that energy, the positron showers are contained in the individual crystal volumes so that the 10 MeV peaks were very sharp and well defined in all twelve ADC spectra.

The data taken at various beam momenta were compared to simulations. In this case also the Geant simulation package was used. The array of twelve calorimeter modules was defined and positioned in the simulation code as it was during the data

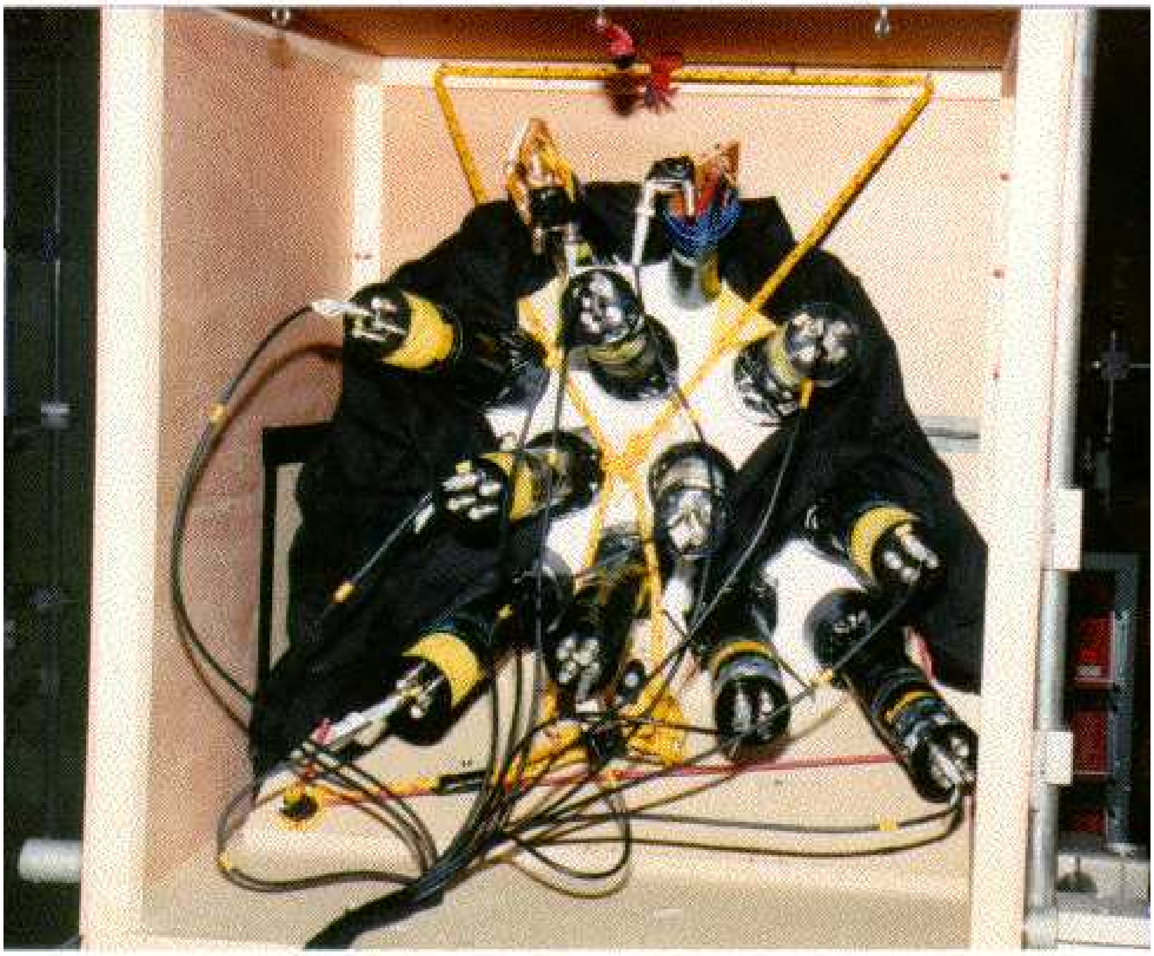

Figure 8.17: The array of CsI crystals with sections of the box and the support structure. The PMT's and the bases are also shown. This view from downstream of the beam does not show the demarcations of the modules due to the white teflon covering the rest of the back faces, and the protective black cloth.

taking process. This was a simplier task since the array was a subsection of the entire calorimeter which had already been described in the Geant simulation code as explained in section 7.4. The beam parameters were also simple to account for because the beam was a parallel, defocused beam with monoenergetic positrons. The positrons were thrown into the central region of the array in order to avoid leakage of the shower through the lateral surfaces, a leakage which would have worsened the energy resolution. In the entire calorimeter, because of its spherical geometry and the presence of the edge vetoes, this lateral leakage of the shower would not be a problem. During the data analysis, the central region of the array was selected with cuts in the MWPC. For the simulations to be realistic and comparable to data, the calculated deposited energies in each crystal were smeared by a Gausssian function

Figure 8.18: A top view of the array showing some of the wooden plates used for support, parts of the box and some of the back faces with PMT's and bases. This was before the box was sealed and set up along the beam line.

whose standard deviation combined the effects of light collection non-uniformity and photoelectron statistics in quadrature. For an event i, if the calculated energies were $dE(i,j)$ with $j = 1, 12$, the smeared energies $E(i,j)$ were obtained as:

$$\sigma(i,j) = \sqrt{\frac{dE(i,j)}{\mathrm{NPM}} + (dE(i,j) * \mathrm{LNU})^2}, \tag{8.7}$$

$$E(i,j) = dE(i,j) + \sigma(i,j) * \mathrm{Gauss(iseed)}; \tag{8.8}$$

where Gauss(iseed) was the function that randomly generated a Gaussian distribution of mean zero and standard deviation one. NPM and LNU were respectively the measured number of photoelectrons per MeV and the light collection non-uniformity in percentage. Previously during the run, 180 photoelectrons per MeV were measured for the CsI crystals, and a light collection non-uniformity of 3% standard deviation was inferred from the analysis of the surface treatment data as shown in figure 8.7. The data and the simulations show excellent agreement for 70, 50, 30 and 10 MeV/c. The measured resolution at 70 MeV/c was 5.6 MeV. This result is of particular importance since it indicates the energy resolution of the calorimeter. The data at 20 MeV/c did not include MWPC information due to a problem during the data taking. For this reason, the data at 20 MeV/c could not be compared to simulations in the same way as the data at the other beam momenta.

During the test of 1994, the array consisted of twenty-six CsI modules. By that time, forty-seven calorimeter modules had been delivered and the twenty-six were selected on the basis of their fast to total ratios and on their dimensional accuracies. The crystals were polished and wrapped in three layers of teflon and one layer of aluminized mylar with black paper at the front faces. After the wrapping, the photomultiplier tubes were glued at the back faces of the modules. Two-inch XP2020Q with a PSI base were used for the HD's while the other shapes were viewed by three-inch EMI 9822K PMT's with a standard CERN base or EMI 9821QB PMT's with a UVA base. The gluing process took place in a special apparatus which held the crystals and the PMT's, and allowed the PMT's to be glued on the

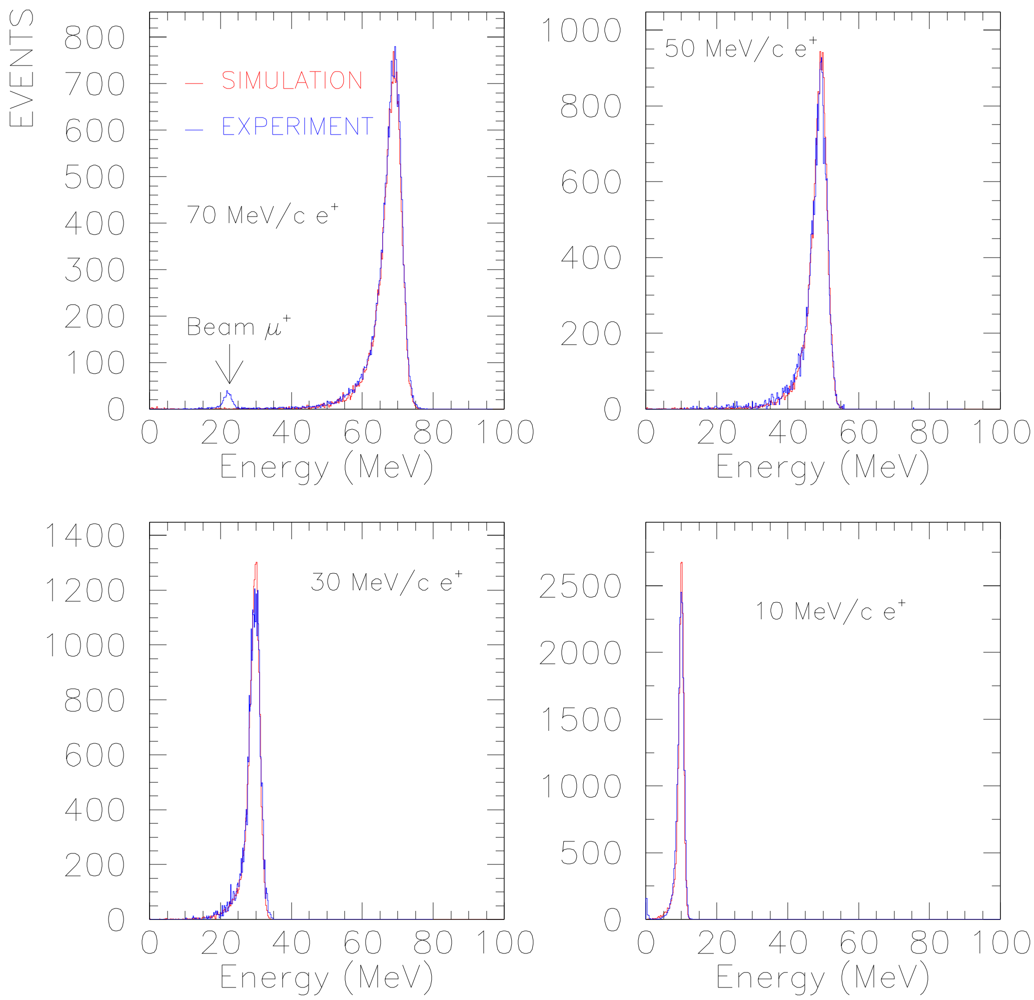

Figure 8.19: The responses of a subsection of the calorimeter to monoenergetic beam of positrons of 70, 50, 30 and 10 MeV/c. The calculated responses with 180 photoelectrons per MeV and 3% light collection non-uniformity show excellent agreement with the data. The measured energy resolution at 70 MeV/c (the e^+'s from $\pi^+ \rightarrow e^+\nu_e$ have ~ 69 MeV) was 5.6 MeV full width half maximum.

centers of the back faces so that the axes of the modules coincided with those of the PMT's (the axes of the HD's and the vetoes do not pass through the centers of their front and back faces; for these shapes, the crystal axes do not coincide with the PMT axes) . The glue consisted of 300 μm layer of silicon elastomer (Sylgard 184). Three days later when the glue had assumed its normal strength, the crystal were tested in the tomography apparatus. In the meantime, the arrangement of the crystals in a light proof enclosure was designed. A special climatization apparatus was constructed to monitor and control the temperature and the humidity inside the enclosure. The climatization system consisted of an air-conditioning device connected to the enclosure via a box which served as a heat exchanger. Seven temperature and humidity sensors were installed inside and outside the enclosure and read out periodically with the data. The relative positions of the crystals and their types are shown in figure 8.20 and a view of the experimental arrangement is shown in figure 8.21. The active target and the degrader were removed and the light proof enclosure was positioned along the beam line so that the central beam trajectory coincided with the body axis of the pentagon. Defocused parallel beams of positrons and electrons of 10, 20, 30, 50 and 70 MeV/c were incident upon the front faces of the modules. The beam intensity was kept relatively low, $\sim 4\times10^4\,\mathrm{s}^{-1}$, to avoid radiation damage to the crystals. The event trigger was $\mathrm{S0}\cdot\sum\mathrm{CsI}$.

The energy calibration required correct pedestal subtractions to establish the energy zero for $\sum$ CsI. The analysis of the data on an event by event basis revealed that the crystals had correlated pedestals for each event: they were either all negative, nearly zero or all positive. This effect was amplified 20-25 times in the $\sum$ CsI. Further analysis showed that the common noise problem was related to the three different types of PMT-base combinations used for the read out: excellent pedestal correlations were observed between crystals of each PMT-base group. Consequently, a second software pedestal subtraction algorithm was worked out for the three PMT-base groups, and the noise correlation problem was resolved with a good fix on the energy zero for $\sum$ CsI.

The data at 10 MeV/c could not be used for the gain matching because the array was much bigger and all the crystals were not uniformly covered by the beam.

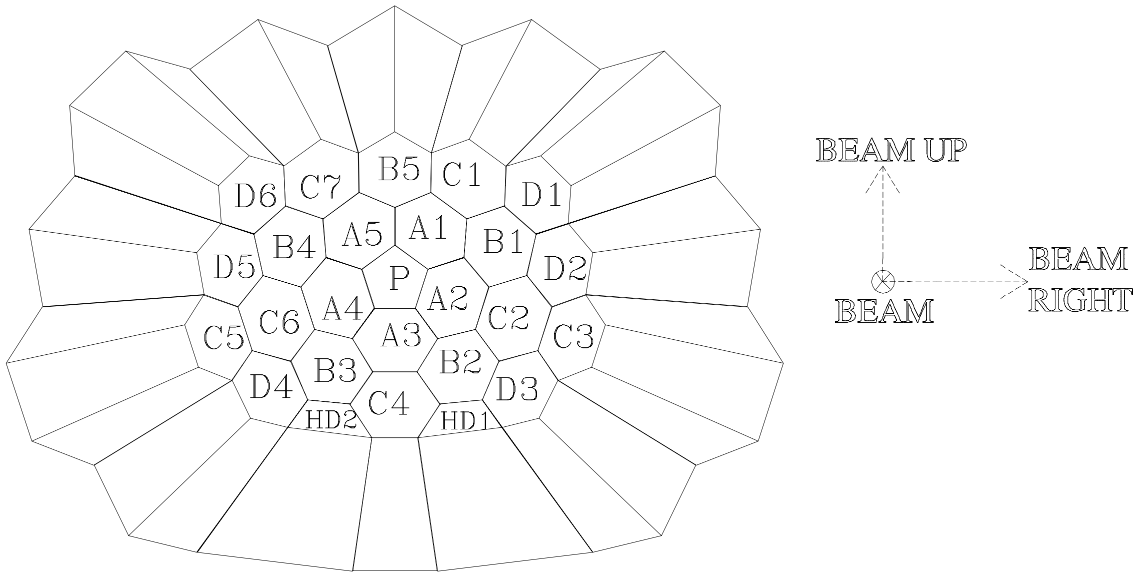

Figure 8.20: The array of twenty-six calorimeter modules used during the test run of 1994. The array was set up in a closed box with a special climatization apparatus to control the temperature and the relative humidity within the box. The parallel defocused beams of positrons and electrons were incident on the front faces of the modules and the central beam trajectory passed through the center of the pentagon.

Consequently the 10 MeV positron peak was not clearly defined in all the twenty-six[3] ADC spectra. The gain matching was done with the endpoint of the Michel spectrum in which case a degrader and a target counter were set up along the beam line, the box containing the crystals was rotated ninety degrees out of the beam line and placed such that the front face of the crystals were 26 cm from the center of the target. The beam channel was switched over to select 116 MeV/c π^+'s and the cascades $\pi^+ \rightarrow \mu^+ \rightarrow e^+$ were detected in the array. Prior simulation of Michel events had indicated that the Michel endpoint was the same in all the crystals. The calibration was also done at 20 MeV/c by changing the trigger $S0 \cdot \sum$ CsI to $S0 \cdot CsI_i$ for the module i (i=1,25) and looking to the $\sum$ CsI spectrum. The ambient

[3]Actually there were only twenty-five. The crystal at the position B5 (S018) was disregarded because it produced very broad signals (large slow component), and as a result messed up the $\sum$ CsI signals. The selection of this crystal was based solely on its good dimensions; its fast/total was unavailable at the time.

temperature in the experimental area varied within band of 2.5 °C with a mean of $\sim$ 27 °C over a period of two days. In the closed box the temperature was maintained at $\sim$ 18 °C with a spread of $\sim$ 1.75 °C over the same period of time. This translated into gain variations due to temperature fluctuations of the order $\pm 1.5\%$.

After the tests with monoenergetic positrons were completed, the polarities of the magnets and quadrupoles were reversed to select negative particles, mainly electrons, using the same momenta as for the positron measurements. A difference between the responses of the array to positrons and electrons is expected because of positron annihilations with atomic electrons. When the resulting two photons are detected in the array, the total energy is increased by 2×0.511 MeV, the electron

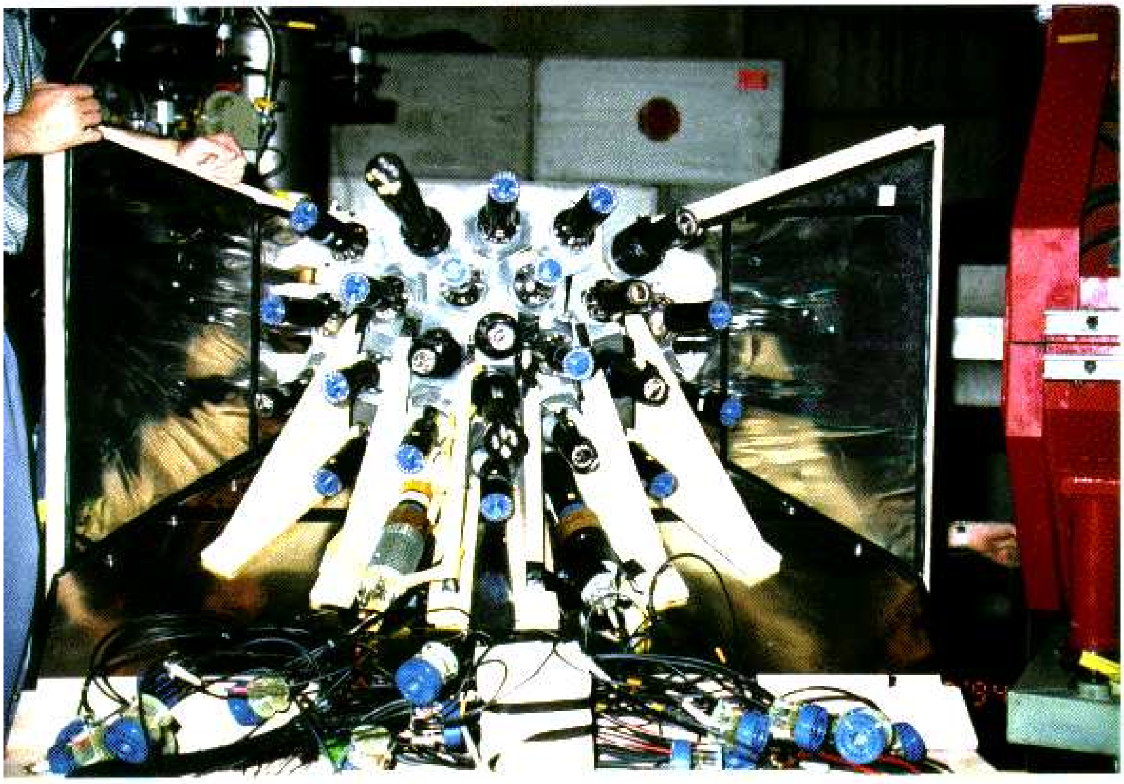

Figure 8.21: The array of twenty-six calorimeter modules seen from the back. The PMT's, some bases and the wooden support structure are shown. Sections of the box enclosing the modules are also visible. The red cylinder on the right is the quadrupole triplet of the $\pi E1$ beam line.

and the positron masses.

The data at 70 MeV/c were used for gain calibration during the off-line analysis. Twenty-five histograms of $\sum$ CsI were defined one for each crystal: for the crystal $\mathrm{CsI_i}$, the corresponding $\sum$ CsI was defined such that the module $\mathrm{CsI_i}$ received a significant portion of the shower energy. From Monte Carlo simulation of the shower spreadings (section 7.4), it is known that if hit centrally, one module will receive 90% of the shower energy, and three crystals receive most of the shower. This gain calibration method is therefore based on the events for which the total shower is contained within the array. The 70 MeV peaks were well defined in the twenty-five $\sum$ CsI spectra and the peak channels were used to calculate the gain correction factors by which the individual ADC spectra were multiplied. This operation resulted in new $\sum$ CsI spectra and gain correction factors. The process was repeated until the 70 MeV peaks fell in the same channel. The energy resolution measured at 70 MeV/c was 4.2 MeV FWHM. This result represents a 25% improvement over the 1993 result. This improvement is attributed to a better wrapping method, a good control of the temperature and the humidity within the box, the quality of the crystals and the size of the array. The results of the analysis are shown in figures 8.22 and 8.23. The data were compared to simulations with excellent agreement. The simulation code was the same one used for the 1993 data with the appropriate modifications regarding the number detector modules and their relative arrangements with respect to the beam.

The CsI array also was used to detect $\pi^+ \to e^+\nu_e$ events in order to test the performance of the calorimeter with a known pion decay channel of interest to the experiment.

8.5 Calorimeter Response to $\pi^+ \longrightarrow e^+\nu_e$

$\pi^+ \to e^+\nu_e$ decays are of prime importance to the pion beta experiment because, as explained in chapter 7, these events are used for normalization of the pion beta processes. Therefore, the pion beta experiment will not only measure the branching ratio of pion beta events but also that of $\pi^+ \to e^+\nu_e$ decays. With twenty-five

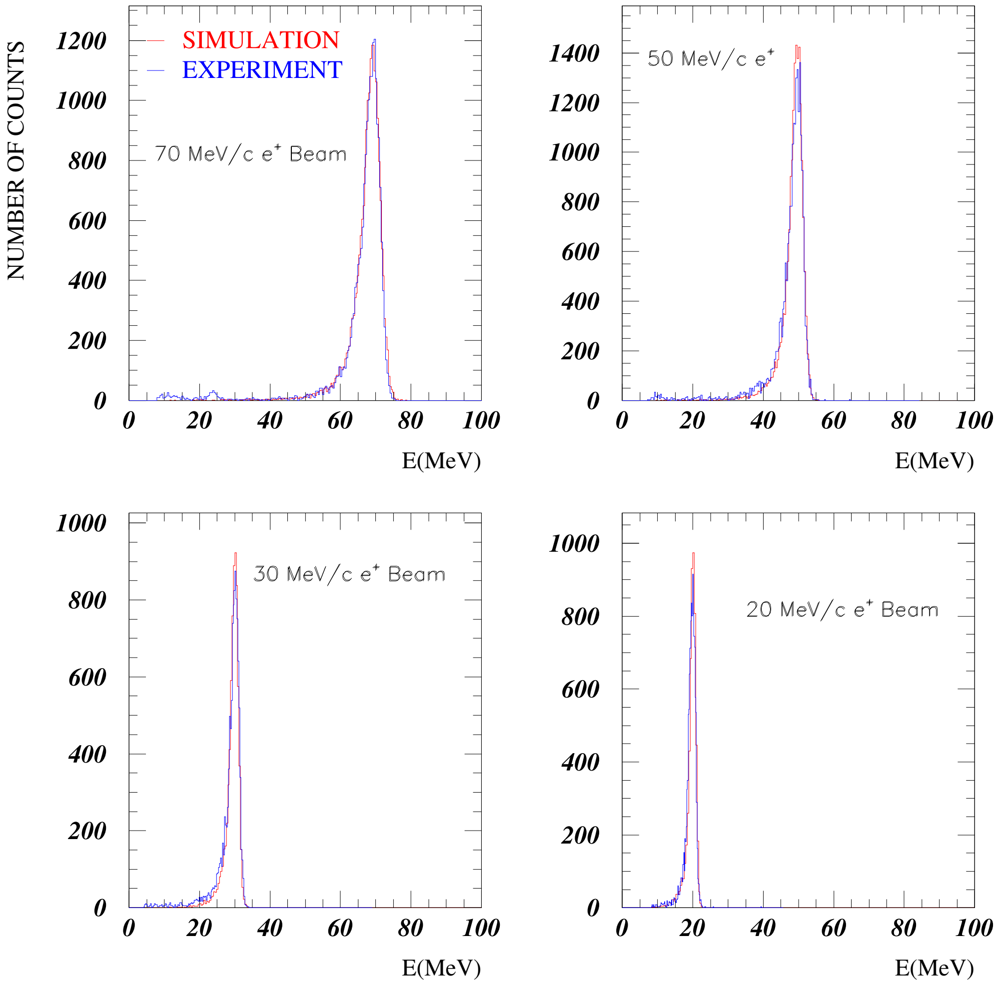

Figure 8.22: The measured line-shapes of the response of the CsI array to monoenergetic positrons of 70, 50, 30 and 20 MeV/c. Data are compared to simulations with excellent agreement. Due to the high discrimination threshold, the data at 10 MeV/c did not exhibit the full spectral response of the array. The resolution at 70 MeV is 4.2 MeV FWHM, a substantial improvement over the result obtained in 1993.

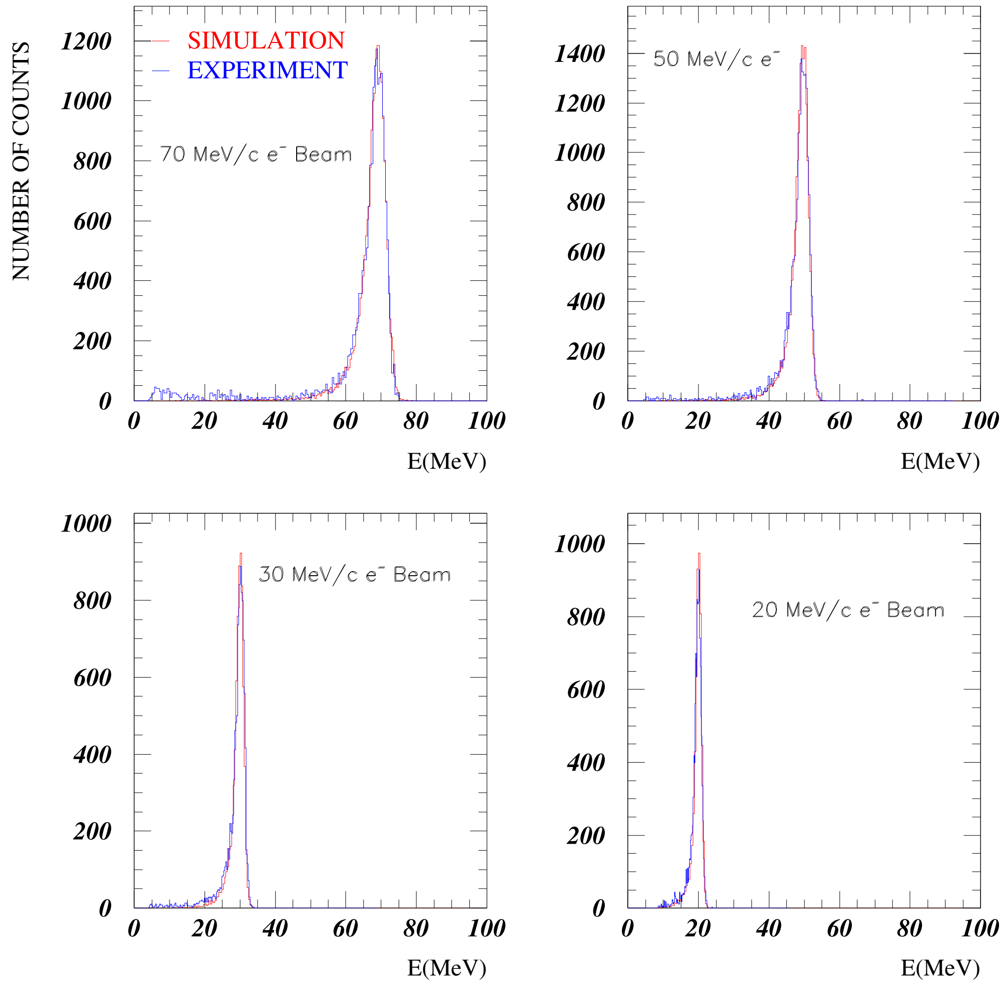

Figure 8.23: The response of the array to electron beams. The expected difference between the positron and the electron responses is due positron annihilations with atomic electrons. However, the 1.02 MeV increase in the total energy coming from the annihilation processes is not observed because of photoelectron statistics and light collection non-uniformity.

detector modules, a fraction of the calorimeter ($\sim 10\%$) was put together with five overlapping clusters (shown in table 8.2) to make a single arm trigger. The beam line set-up consisted of a 4 cm active degrader (S1), a 5 cm active target (S2) and the box containing the calorimeter modules as shown in figure 8.24. A very thin (0.3 cm) plastic scintillator counter was placed in front of the array and used as veto for hadronic processes. The stopped pion was defined as the coincidence

Cluster	#	1	2	3	4	5	6	7	8
CL1	6	P	A1	A2	A3	A4	A5		
CL2	8	B1	D1	D2	C3	C2	A2	A1	C1
CL3	8	B2	C2	D3	HD1	C4	A3	A2	C3
CL4	8	B3	A3	C4	HD2	D4	C6	A4	C5
CL5	8	B4	C7	A5	A4	C6	C5	D5	D6
Supercluster(SC)	5	CL1	CL2	CL3	CL4	CL5			

Table 8.2: The cluster definitions during the test run of 1994. There was only one supercluster which was the entire array. These definitions were not exactly the same ones presented in section 7.4.3. However, the scheme was the same, i.e., each module was shared at most three times. Electronically, the PMT signals were split the number of times they were shared and sent to the adders where the cluster and supercluster signals were produced with a high and a low discrimination levels.

between the beam counter S0 (see figure 3.6 where S0 is the scintillator counter located behind the lead collimator), the active degrader S1 and the RF, timed appropriately for pion selection: $\mathrm{S0} \cdot \mathrm{S1} \cdot \mathrm{RF}$. The stopped pion initiated a delayed pion gate (DπG) of 60 ns during which the $\pi^+ \to e^+\nu_e$ decays were registered as the coincidences $\sum \mathrm{CsI} \cdot \mathrm{D}\pi\mathrm{G} \cdot \overline{\mathrm{PROMPT}}$. The signal $\sum \mathrm{CsI}$ was the supercluster signal — with high discrimination level but with the timing of the low discrimination level signal which enabled a good timing resolution and the elimination of some prompt events which might otherwise have slipped into the DπG — obtained as the "OR" of the five cluster signals. The low and high discrimination levels were set at 3 MeV and 25 MeV respectively. The high discrimination level eliminated a significant fraction of the accidental Michel events and reduced the computer dead time. The absence of the prompt veto, $\overline{\mathrm{PROMPT}}$ which was provided by the S1 counter, led to the domination of the spectrum by prompt events. The electronic diagram is shown in figure 8.25 with the trigger for $\pi^+ \to e^+\nu_e$ events. However, data were also collected for prompt and Michel processes, in which case the event trigger was modified to $\sum \mathrm{CsI} \cdot \pi\,\mathrm{STOP}$ and $\sum \mathrm{CsI} \cdot \mathrm{D}\mu\mathrm{G} \cdot \overline{\mathrm{PROMPT}}$ respectively. As previously mentioned, the endpoint of the Michel spectrum had been used for gain calibration of the CsI detectors, and the prompt events provided a timing calibration and a reliable way to time in various signals. The delayed muon gate DμG was also initiated by the stopped pion but delayed by about 250 ns with respect

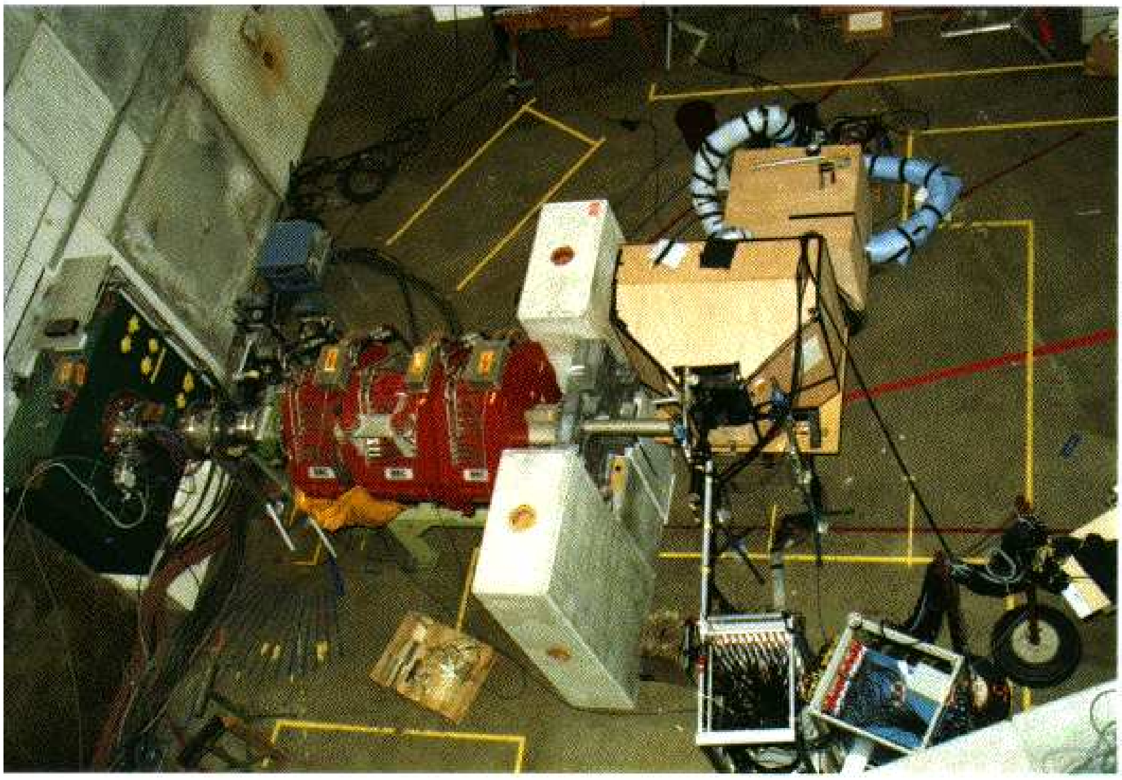

Figure 8.24: The beam line set-up to measure $\pi^+ \to e^+\nu_e$ decays. 116 MeV/c π^+'s traversed the plastic scintillator degrader and stopped within the active target. $\pi^+ \to e^+\nu_e$ decays were detected in the array of twenty-five crystals which subtended $\sim 8\%$ of 4π solid angle. The concrete shielding and parts of secondary beam channel in the $\pi E1$ area are also shown. Behind the wooden box of CsI detectors, is the climatization apparatus.

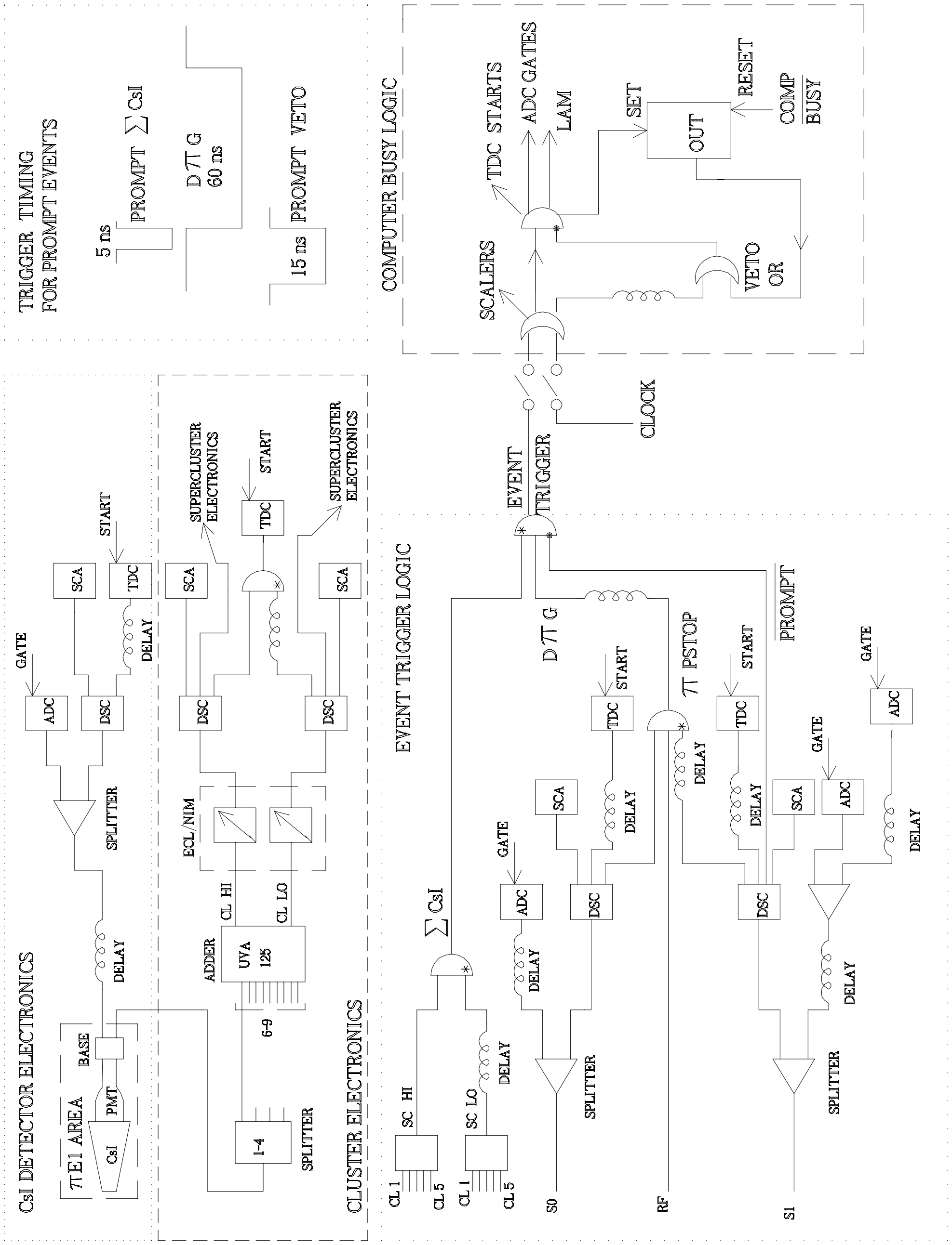

Figure 8.25: The electronic diagram for the $\pi^+ \to e^+\nu_e$ trigger. The upper and lower discrimination levels were 25 and 3 MeV respectively: this meant that 16% of the accidental Michel events were cut away in the trigger. The delayed pion gate was opened 15 ns after a valid pion stop.

to the pion stop time. As displayed in figure 7.2, 250 ns after the pion stop time,

	Measured Rates
Counter S0	255 kHz
Counter S1	114 kHz
$S0 \cdot S1$	100 kHz
$S0 \cdot S1 \cdot RF$: Stopping rate	72 kHz
Trigger: $\sum \mathrm{CsI} \cdot \mathrm{D}\pi\mathrm{G} \cdot \overline{\mathrm{PROMPT}}$	100 Hz

Table 8.3: The rates measured during the taking at an average proton current of $840\,\mu A$. The computer live time was $\sim 60\%$.

the number of $\pi^+ \to e^+\nu_e$ events was negligible and the DμG was only sensitive to Michel events. The temporal distributions (shown in figure 7.2) of $\pi^+ \to e^+\nu_e$ and Michel events are given by the following relations respectively:

$$N_{\pi^+ \to e^+\nu_e} = BR_{\pi^+ \to e^+\nu_e} N_\pi \Omega e^{-\lambda_\pi t_o}(1 - e^{-\lambda_\pi T}), \tag{8.9}$$

and

$$N_{\pi\mu e} = N_\pi \Omega \frac{\lambda_\pi \lambda_\mu}{\lambda_\pi - \lambda_\mu} \left[\frac{1}{\lambda_\mu} e^{-\lambda_\mu t_o}(1 - e^{-\lambda_\mu T}) - \frac{1}{\lambda_\pi} e^{-\lambda_\pi t_o}(1 - e^{-\lambda_\pi T}) \right]; \tag{8.10}$$

where N_π is the rate of pion stops, $\Omega = 8\%$ is the fraction of solid angle subtended by the CsI array, $t_o = 15\,\mathrm{ns}$ is the delay of DπG with respect to the pion stop time (t=0), $T = 60\,\mathrm{ns}$ is the length of the delayed pion gate, $1/\lambda_\pi = 26\,\mathrm{ns}$ and $1/\lambda_\mu = 2.2\,\mu\mathrm{s}$ are the mean lifetimes of the pion and muon respectively, and $BR_{\pi^+ \to e^+\nu_e} = (1.235 \pm 0.005)\,10^{-4}$ is the $\pi^+ \to e^+\nu_e$ branching ratio. Some of the measured rates are compiled in table 8.3. The expected trigger rate (102 Hz) was the fraction of $N_{\pi\mu e}$ with energies above the upper discrimination level of $\sum$ CsI. The rate of $\pi^+ \to e^+\nu_e$ in the CsI array was given by equation 8.9. The explicit calculation gave $\sim 0.4\,\mathrm{s}^{-1}$, consistent with the on-line observations.

A cut on the energy spectrum of the plastic veto detector in front of the CsI not only eliminated the very energetic hadronic interactions but also some of the double Michel events $(\mu^+ \to e^+\nu_e\bar{\nu}_\mu)^2$. The double Michel processes form a broad energy spectrum extending up to $\sim 105\,\mathrm{MeV}$ with the most probable energy close

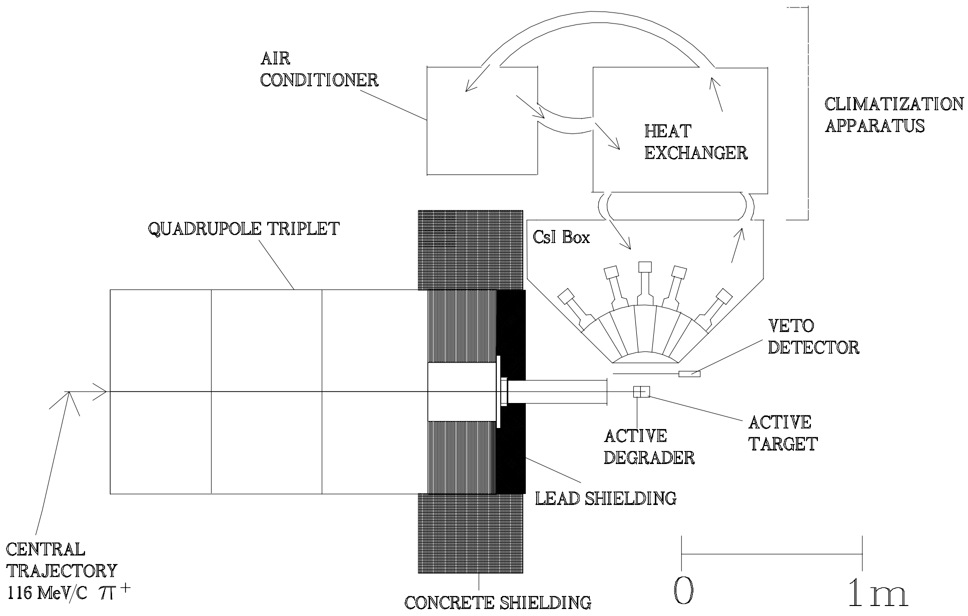

Figure 8.26: The experimental arrangement for the study of $\pi^+ \to e^+\nu_e$ decays.

to the $\pi^+ \to e^+\nu_e$ peak. The suppression of these events dictated the need for the two cylindrical MWPC's with double track resolution as explained in chapter 5. However, the test run of 1994 was not equipped with MWPC's. As a result, the measured $\pi^+ \to e^+\nu_e$ spectrum shown in figure 8.27 rides on some double Michel background which was not cut away by the plastic veto detector alone. The reduction of the beam intensity by a factor of three resulted in an additional suppression of the double Michel events by a factor of ten.

The measured $\pi^+ \to e^+\nu_e$ spectrum is well separated from the Michel background and the resolution could be improved by compensating for the energy dispersion in $\sum$ CsI due to the energy losses of the positrons in the target and the plastic veto. To that end, two ADC inputs were implemented for the target S2 and the degrader S1. One of the ADC inputs was in time with the trigger while the other was delayed. The delayed ADC inputs measured the charge which preceded the pulse in time with the trigger and allowed full energy reconstructions in S1 and S2 signals. The energy scales for the degrader and the target were absolutely calibrated using the

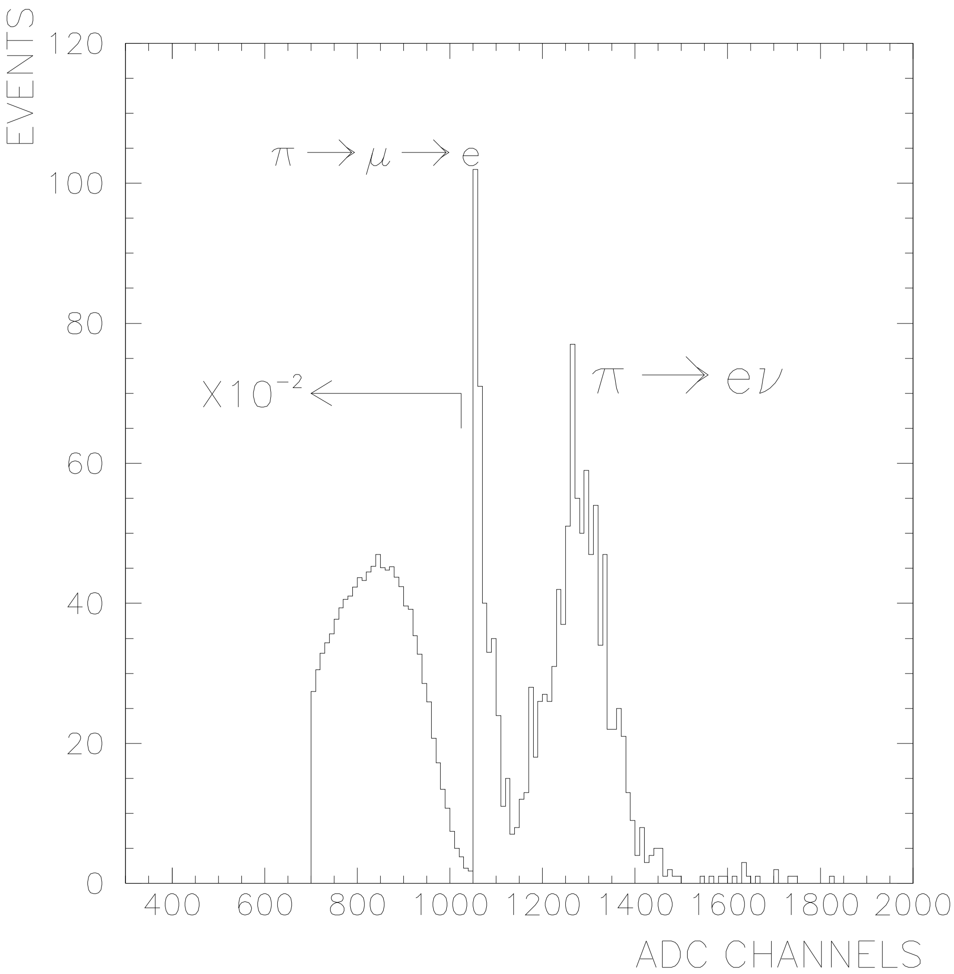

Figure 8.27: $\pi^+ \rightarrow e^+\nu_e$ spectrum measured during the test run of 1994. After accounting for the double Michel background, the number of $\pi^+ \rightarrow e^+\nu_e$ events observed is consistent with the correct branching ratio. The energy calibration, obtained from Monte Carlo simulation of $\mu^+ \rightarrow e^+\nu_e\bar{\nu}_\mu$ and $\pi^+ \rightarrow e^+\nu_e$, is 20.55 ADC channels per MeV. Due to the energy loss in the target (3.80 MeV) and in the plastic veto (0.90 MeV), the peak energy detected in the array for $\pi^+ \rightarrow e^+\nu_e$ events is 63.25 MeV which corresponds to $\sim$ 1300 ADC channels while the detected endpoint of the Michel spectrum is $\sim$ 53MeV, i.e. channel 1090.

measured peak positions of the light outputs in S1 and S2 and the expected energies deposited in these counters by the beam positrons, muons and pions. Electron equivalent energies [Mad-78] were used in the calibration for muons and pions. For the degrader S1, the fully reconstructed energy was used to identify the beam particle which preceded the event. On the other hand, for the target S2, the reconstructed energy was used to identify the Michel events from $\pi^+ \to e^+\nu_e$ decays as shown in figure 8.28: in fact, the cascades $\pi^+ \to \mu^+ \to e^+$ were expected to deposit an additional 4.118 MeV in the target relative to the $\pi^+ \to e^+\nu_e$ events due to muon stops. Therefore, the correlations between the full target energy and $\sum$CsI

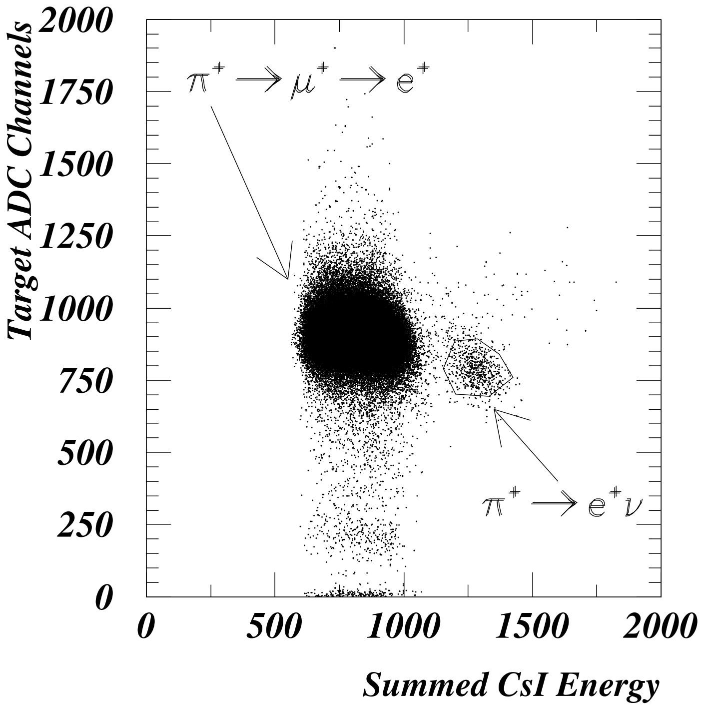

Figure 8.28: The separation between Michel decays and the $\pi^+ \to e^+\nu_e$ events. The mean energy of the Michel events in the target is higher by ~ 3.2 MeV than that of the $\pi^+ \to e^+\nu_e$ events due to the 4.118 decay muons.

(triggered on one of the crystals for better energy resolution and cut on positrons in the plastic veto detector) revealed two groups of particles with one group having ~ 3.2 MeV — this result is obtained from the absolute calibration and the energy distribution of the active target cut on Michel and $\pi^+ \to e^+\nu_e$ events in the CsI array — more than the other group in S2. The expected light output from the 4.118 MeV muons in target was ~ 3.1 MeV in agreement with measurement.

The goal of the test was to measure the response of the calorimeter to $\pi^+ \to e^+\nu_e$ decays. In that respect, the test run was very instructive and encouraging. The re-

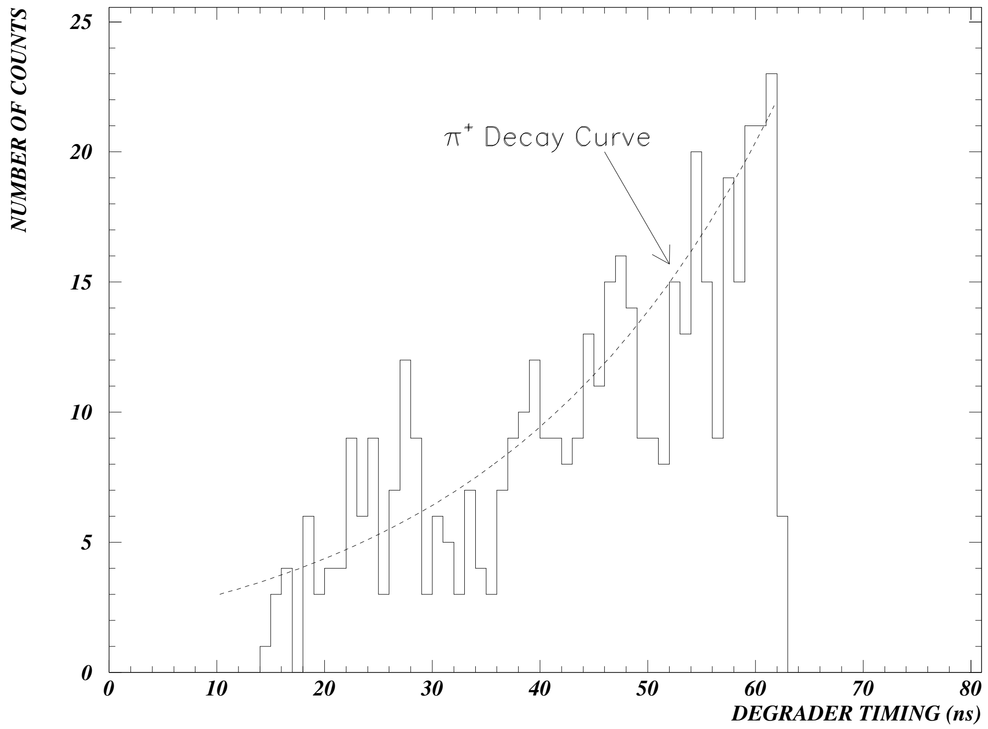

Figure 8.29: The measured pion decay curve versus expectation (dashed line).

sult of figure 8.27 shows a clean separation between the Michel and the $\pi^+ \rightarrow e^+\nu_e$ events. The resolution will certainly be improved with the elimination of the double Michel events using MWPC's with good double track resolution. From the measurements of the responses of the array to monoenergetic positrons, electrons, and $\pi^+ \rightarrow e^+\nu_e$ decays, it can be concluded that the pion beta shower calorimeter, operated under controlled temperature and humidity and equipped with excellent CsI modules with good surface treatment, is capable of detecting $\pi^+ \rightarrow e^+\nu_e$ decays with good energy and timing resolutions which are necessary to isolate this process from the background. The other reaction of interest to the pion beta experiment is the pion beta decay. This process ultimately produces two photons of $\sim 65 - 70\,\mathrm{MeV}$ which are expected to be detected in the shower calorimeter. It has therefore been necessary to check the response of the calorimeter to photons of similar energies.

Such photons were produced during the test run of 1994 via the charge exchange reaction $\pi^- p \rightarrow \pi^0 n$, and the data are currently being analyzed.

With the number of $\pi^+ \rightarrow e^+\nu_e$ decays measured and the number of pions stopped in target, an estimate of the branching ratio $BR_{\pi^+ \rightarrow e^+\nu_e}$ can be made. It should be stressed that the measurement of the branching ratio $BR_{\pi^+ \rightarrow e^+\nu_e}$ was not the goal of the test run and as a result, the experiment was not fully equipped for a precise determination of $BR_{\pi^+ \rightarrow e^+\nu_e}$. Of the $2.34\,10^9 \pm 4.84\,10^4$ particles stopped in the target, $\sim 76\%$ were pions and $5.68\,10^3 \pm 7.54\,10^1$ $\pi^+ \rightarrow e^+\nu_e$ decays were registered in the array. Taking into account the fraction of solid angle $(8.0 \pm 0.4)\%$ subtended by the array, the fraction of pions still alive at the time the delayed pion gate is opened (0.56), and correction factors such as the computer live time (60%), positron annihilation $\sim$ 2%, shower backsplash $\sim$ 1%, and the veto inefficiency $\sim$ 0.3%, the estimated branching ratio is $BR_{\pi^+ \rightarrow e^+\nu_e} \simeq (1.23 \pm 0.02 \pm 0.06)\,10^{-4}$.

Chapter 9

Conclusion

A review of the material presented and discussed in the chapters 1-8 is given here. This review constitutes the progress made toward the precision measurement of the pion beta decay since the conception of the project and the development run of 1989.

9.1 Scientific Motivation

The pion beta decay ($\pi^+ \to \pi^0 e^+ \nu_e$) is a semi-leptonic process involving only vector interactions. It is a transition between spin zero members of an isomultiplet and is therefore similar to superallowed Fermi transitions in nuclear beta decay. The measurements of the $\mathcal{F}t$ values of the Fermi decays can be used to test the CVC hypothesis, quark-lepton universality and the unitarity of the CKM quark mixing matrix. From the neutron beta decay which involves the full V$-$A structure of the weak interactions, it is possible to extract the mixing angle between the up and the down quarks by measuring the ratio of the weak vector to the axial-vector coupling constants and the neutron lifetime. The discrepancy between Fermi beta decay data and the neutron beta decay data dictates the need for a new precision experiment. Pion beta decay ($\pi^+ \to \pi^0 e^+ \nu_e$) being the most direct test of CVC, presents an independent approach to extract the weak vector coupling constant without the complication of nuclear corrections, screening effects and final states Coulomb interactions. Only radiative corrections are needed in the calculation of the pion beta decay rate, and these corrections have been evaluated up to the leading terms in

$Z\alpha^2$ and amount to $\sim 3\%$. Experimentally however, the study of the pion beta decay is complicated by its small branching ratio. The most precise measurement of the pion beta decay rate to date is in good agreement with theory but stands at 4% experimental accuracy. It is desirable to improve upon this result since it is not precise enough to test the full extent of radiative corrections. Therefore, an experiment has been designed to do a precise measurement of the pion beta decay rate at the Paul Scherrer Institute in Switzerland. During the first phase of the experiment, an attempt will be made to measure the decay rate with an overall uncertainty of 0.5%. At this level of precision, it will be possible to test the CVC hypothesis and the radiative corrections, and to compare the Fermi beta decay data to the neutron decay data. An even more precise measurement will be made during the second phase of the experiment, reducing the uncertainty to the level of 0.2%-0.3%. This will allow a test of the CKM unitarity and place constraints on possible new physics beyond the Standard Model of the elementary particle physics.

9.2 Experimental Method and Detector Design

The experimental approach relies on the coincident detection of the two photons which originate from the subsequent decay of the neutral pion, $\pi^0 \to \gamma\gamma$. The process $\pi^+ \to e^+\nu_e$ is used for the normalization of the pion beta decay events. The experiment is therefore a relative experiment with a stopped pion technique. The relative measurement of the pion beta decay rate is possible because of the similarity between the detector acceptances and responses to $\pi^+ \to e^+\nu_e$ and $\pi^+ \to \pi^0 e^+\nu_e$ events. As a result, the differences in the systematic uncertainties are very small. Monte Carlo calculations have shown that the processes which affect the detection efficiency of pion beta events and constitute the main sources of systematic uncertainties occur at the level of few percent.

Positive pions of 116 MeV/c are transported by the secondary beam channel ($\pi E1$) of the Ring accelerator to the experimental apparatus which consists of: beam counters and an active target to identify and stop the pions, two cylindrical MWPC's for charged particle tracking and for additional suppression of the background, a segmented, cylindrical plastic veto detector for the identification of charged particle induced events, a highly segmented shower calorimeter made from pure CsI for the detection of gamma rays and high energy electrons and positrons, thermal insulation around the detectors for the control and stabilization of the temperature and the humidity, a lead shield to avoid self-vetoing due to shower leakage, cosmic veto detectors and the read out electronics. The segmentation of the calorimeter was obtained from a class II geodesic triangulation of an icosahedron with the requirements of uniform coverage of solid angle by the resulting modules, minimal number of the different modular shapes, high rate capability and good energy resolution. The choice of CsI as the material of the calorimeter was due to the properties of this inorganic scintillator. The development run of 1989 has shown that CsI can provide a good timing resolution and has a much longer attenuation length to its radiation than previously reported. In addition, compared to some other organic scintillators, the higher refractive index of CsI makes it easier to achieve better uniform light collection for the tapered truncated pyramidal shapes of the calorimeter. The thickness of the calorimeter was chosen as a compromise between the energy resolution and the cost, both of which increase with the thickness. Monte Carlo studies of the spreadings of the showers produced by photons from pion beta decay and positrons from $\pi^+ \to e^+\nu_e$ aided in the choice of the granularity and the design of the trigger elements as overlapping clusters of 6-9 calorimeter modules. The current clustering scheme is $\sim$ 99% efficient in detecting valid $\pi^+ \to \pi^0 e^+ \nu_e$ and $\pi^+ \to e^+\nu_e$ events with energy depositions above the threshold. The expected angular resolution of the calorimeter is 5° FWHM as shown in figure 9.1.

9.3 Detector Testing and Calibration

After delivery, the CsI crystals must pass three tests to be selected for use in the calorimeter: the ratio of the fast component to total scintillation light output must be greater than seventy percent; the linear and angular dimensions of a given crystal must be within predefined tolerances; the light collection non-uniformity must be better than three percent. Various surface treatment methods have been in-

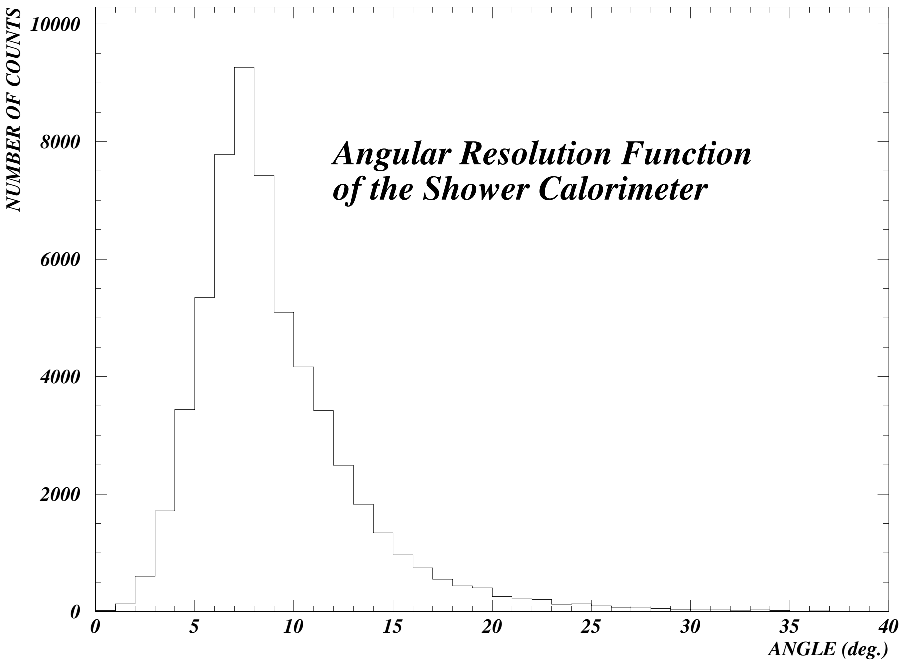

Figure 9.1: The resolution function is obtained as the deviation of the shower centroid from the starting direction of the original particle. In this case, 70 MeV photons were thrown isotropically into the detector apparatus according the stopping distribution. The angular resolution is 5° FWHM.

vestigated for maximal light output and maximum non-uniformity and a cosmic ray tomography apparatus has been set up to measure the light non-uniformity throughout the volume of each module. A particular surface treatment consisting of three layers of teflon plus one layer of aluminized mylar was arrived at by the time of the development run of 1994; as a result, the modules used during that run were wrapped as described above. The results of the development runs aided in the optimization of the design of the apparatus, revealed the performance of the main detector systems and validated the experimental technique. During the test of 1992, the effort was concentrated exclusively on the beam and its parameters such as the spot size, the horizontal and the vertical profiles, the contaminations and the beam particle rates. The results of this test affected the design of the active target and its segmentation. The target was fabricated at the University of Virginia and inserted in the beam during the test run of 1993. By that time, some CsI modules were delivered by Bicron Corporation and it was possible to build up a section of the calorimeter and to study the responses of the array to monoenergetic beams of positrons at various momenta. The line shapes of the responses of the array were compared to simulations. Excellent agreement was observed after the effects of photoelectron statistics and light collection non-uniformity were accounted for. At 70 MeV/c (this is the energy of interest since the e^+'s from $\pi^+ \to e^+\nu_e$ have $\sim 69\,\mathrm{MeV}$) the measured energy resolution of the calorimeter was 5.6 MeV FWHM. The study of the stopping rate in the active target revealed that the number of stopped pions scaled with the area of twenty-five, nine and four fibers. This allowed the redesign of the active target with $3 \times 3\,\mathrm{mm}^2$ fibers instead of $2 \times 2\,\mathrm{mm}^2$. The redesigned active target was also built in Virginia and tested in beam during the test run of 1994: the beam distributions measured with the active target suggest a beam spot of $< 1\,\mathrm{cm}$ FWHM. Another study conducted during the 1993 run was a test of the wrapping method. Of the various surface treatments considered, black paper at the front faces of the crystals with the lateral surfaces wrapped in teflon gave the best light output and uniformity. Further studies after the run led to the wrapping system used in the tomography apparatus and during the test run of 1994. In the tomography system, the directions of the cosmic muons are defined by three drift chambers. The path-lengths of the cosmic rays and their energy depositions in the CsI modules are used in a reconstruction algorithm which finds the light per unit path-length in the volumes of the modules — the crystals are subdivided into cubic cells and the reconstructed light yields per path-lengths in the cells constitute a measure of the optical non-uniformity in the crystals. The CsI modules used during the test of 1994 were all examined in the tomography system. More crystals were delivered by that time and it was possible to set up a much bigger portion of the calorimeter than the one used in the 1993 experiment. The line shapes of the responses of the calorimeter were remeasured with not only monoenergetic e^+'s but monoenergetic e^-'s as well. With a good control of the temperature and the humidity, a better wrapping system, and a bigger size of the array, a better energy resolution was achieved, i.e., 4.2 MeV FWHM. In addition, the response of the array to $\pi^+ \to e^+\nu_e$ decays confirmed the need for MWPC's with good double track resolution for additional suppression factors of double Michel events. The $\pi^+ \to e^+\nu_e$ decays were well separated from the Michel background and the number of $\pi^+ \to e^+\nu_e$ events collected was consistent with the correct branching ratio.

9.4 Outlook

The initial design and the calibration phase of the pion beta decay experiment have been described in this thesis. The experiment continues with the assembly of the apparatus and the data collection phase. Thus, the first results on the pion beta decay rate are several years away as of the writing of this thesis.

Bibliography

[Ate-81] L. G. Atencio, J. F. Amann, R. L. Boudrie and C. L. Morris, *Nucl. Inst. and Meth.*, **187**, 381 (1981).

[Byc-73] E. Bycking and K. Kajantie, *Particle Kinematics*, (John Wiley & Sons, 1973) p. 103.

[Bli-73] R. J. Blin-Stoyle, *Fundamental Interactions and the Nucleus*, (North-Holand Publishing Comp. 1973) p. 246.

[Bud-74] T. F. Budinger and Gullberg, *IEEE Trans. Nucl. Sci.,* NS-21, **2** (1974). *Lawrence Berkeley Laboratory Report*, **LBL-2146**, (1974).

[Che-79] D. C. Cheng and G. K. O'Neill, *Elementary Particle Physics*, (Addison-Wesley Publishing Company, 1979), p. 158.

[Dav-69] B. Davidson, *The African Genius*, (Little, Brown & Company in association with The Atlantic Monthly Press, 1969) p. 17.

[Dep-68] P. Depommier, J. Duclos, J. Heintze, K. Kleinknecht, H. Riesenberg and V. Soergel, *Nucl. Phys.* **B4** (1968) 189.

[Dru-87] E. G. Drukarev and M. I. Strikman, *Phys. Lett.* **186B** (1987) 1.

[Ero-90] Erozolimskiĭ, A. Kuznetsov, I. A. Kuĭda, Yu. A. Mostovoĭ, I. V. Stepanenko, *Yad. Fiz.*, **52**, 1583 (1990).

[Geo-84] H. Georgi, *Weak Interactions and Modern Particle Theory*, (The Benjamin/Cummings Publishing Comp. Inc) p. 58.

[Got-84] K. Gottfiried and V. F. Weisskopf, *Concepts Of Particle Physics*, Vol. 1, (Oxford University Press 1984) p. 134.

[Hal-84] F. Halzen and A. D. Martin, *An Introductory Course in Modern Particle Physics*, (John Wiley & Sons Inc. 1984) p. 261.

[Har-90] J. C. Hardy, I. S. Tower, V. T. Koslowsky, E. Hagberg and H. Schmeing, *Nucl. Phys.* **A509**, 429 (1990).

[Hor-75] W. F. Hornyak, *Nuclear Structure*, (Academic Press 1975) p. 525.

[Jau-87] W. Jaus and G. Rasche, *Phys. Rev. D* **35** (1986) 3420.

[Ken-76] H. Kenner, *Geodesic Math And How To Use It*, (University of California Press, Berkeley 1976) p. 82.

[Mad-78] R. Madey, F. M. Waterman, A. R. Baldwin, J. N. Knudson, J. D. Carlson and J. Rapaport, *Nucl. Instr. and Meth.* **151** (1978) 445.

[Mar-86] W. J. Marciano and A. Sirlin, *Phys. Rev. Lett.* **56** (1986) 22.

[Mar-87] W. J. Marciano and A. Sirlin, *Phys. Rev. D* **35** (1987) 1672.

[McF-85] W. K. McFarlane, L. B. Auerbach, F. C. Gaille, V. L. Highland, E. Jastrzembski, R. J. Macek, F. H. Cverna, C. M. Hoffman, G. E. Hogan, R. E. Morgado and R. D. Werbeck, *Phys. Rev. D* **32** (1985) 547. *Phys. Rev. D* **25** (1982) 2259.

[Mor-82] C. L. Morris, *Nucl. Inst. and Meth.*, **196**, 263 (1982).

[Oku-82] L. B. Okun, *Leptons and Quarks*, (North-holland Publishing Comp. 1982) p. 29.

[Orm-85] W. E. Ormand and B. A. Brown, *Nucl. Phys.* **A440** (1985) 274.

[Orm-89] For the most up-to-date discussion of δ_C see: W. E. Ormand and B. A. Brown, *Phys. Rev. Lett.* **62** (1989) 866.

[Ran-81] R. D. Ransome, Ph.D. Thesis, *LA-8919-T*, LAMPF, Los Alamos, 1981.

[Ran-82] R. D. Ransome, S. J. Green, C. L. Hollas, B. E. Bonner, M. W. McNaughton, C. L. Morris and H. A. Thiessen, *Nucl. Inst. and Meth.*, **201**, 309 (1982).

[Sch-83] F. Scheck, *Leptons, hadrons and Nuclei*, (Elsevier Science Publishers B.V. 1983) p. 324.

[Shr-78] R. E. Shroch and L. Wang, *Phys. Rev. Lett.* **41** (1978) 35.

[Sir-78] A. Sirlin, *Rev. Mod. Phys.* **50** (1978) 573.

[Sir-86] A. Sirlin and R. Zucchini, *Phys. Rev. Lett.* **57** (1986) 1994.

[Sir-87a] A recent review of the status of radiative corrections to Fermi decays, including references to previous work, is found in: A. Sirlin, *Phys. Rev. D* **35** (1987) 3423.

[Sir-87b] A. Sirlin, *Comments Nucl. Part. Phys.* **17**, 279 (1987).

[Sir-89] A. Sirlin, *private communication*, 1989.

[Tow-77] I. S. Towner, J. C. Hardy and M. Harvey, *Nucl. Phys.* **A284** (1977) 269.

[Wil-78] D. H. Wilkinson, in *"Nuclear Physics with Heavy Ions and Mesons"*, ed. by R. Balian, M. Rho and G. Ripka (North-Holland, Amsterdam, 1978), p. 877.

[Wei-92] Y. Z. Wei and R. Y. Zhu, *DOE Research and Development Report*, **CALT-68-1778**, (1992).

[Woo-90] C. L. Woody, P. W. Levy, J. A. Kierstead, T. Skwarnicki, Z. Sobolewski, M. Goldberg, N. Horwitz, P. Souder, and D. F. Anderson, *IEEE Trans. Nucl. Sci.*, **37**, 492 (1990).